UNIVERSITY OF SOUTHAMPTON

On the reflection of the equatorial waves at eastern ocean boundaries

by

Jacyra Ramos Soares

A dissertation submitted in candidature
for the degree of Doctor of Philosophy
at the University of Southampton

November 1993

UNIVERSITY OF SOUTHAMPTON
ABSTRACT
FACULTY OF SCIENCE
OCEANOGRAPHY
Doctor of Philosophy

On the reflection of the equatorial waves at eastern ocean boundaries

by Jacyra Ramos Soares

Observational and theoretical studies have indicated that much of the oceanographic variability along the eastern ocean boundaries, for example that associated with El Niño, is remotely forced. The remotely forced motion along these boundaries originates from the reflection of low frequency baroclinic Kelvin waves on the equatorial boundary. At the equator, part of the incoming Kelvin wave energy is reflected in the form of westward propagating Rossby waves and the remainder of the energy is divided between northward and southward propagating coastal Kelvin waves. Previous analytical results have shown the strong dependence of both coastline slope and incident wave frequency on the wave reflection at the eastern boundary.

A baroclinic shallow water model is developed to explore the behaviour of the baroclinic equatorial Kelvin waves when they reach different eastern oceanic boundaries. The large latitudinal extent used in the numerical domain permits consideration of the response at both equatorial and mid-latitudes. Previous analytical studies in this field have always excluded some effects, such as viscosity and non linearities, and employed approximations (equatorial β-plane, low frequency wave, meridional boundaries, for example) to the governing equations in order to solve them analytically. Numerical solutions, however, can be obtained without these approximations and the real ocean is viscous, non linear and has nonmeridional boundaries.

The energy flux results indicate that the nonlinear effects can be regarded as negligible when considering reflection of equatorial waves at an eastern boundary, whereas the viscous effects are very important. The influence of the coastline geometry and the incident wave period, is found to be more important for the westward energy flux than for the poleward flux. It is recommended that any numerical model involving the reflection of baroclinic Rossby waves at eastern boundaries consider the effect of the coastline geometry in order to improve the accuracy of its results. Meridional boundary models should give accurate results for the poleward energy fluxes at seasonal and annual periods. For comparatively shorter periods, the appropriate Atlantic or Pacific coastline geometry should be included to obtain more accurate results.

To the boys: Gil, Diogo and Ivan.

ACKNOWLEDGEMENTS

I wish to thank the Conselho Nacional de Desenvolvimento Científico e Tecnológico, CNPq (Brasília, Brazil, scholarship no 260102/89.0) for the financial support of this work. In addition I wish to thank Dr. Neil Wells for his supervision and comments during the course of this research.

I also want to thank Prof. Steve Thorpe for his useful suggestions on this research. I am also indebted to Dr. Wolfgang Barkmann for his interest and illuminating suggestions at times when the work progress was slow.

My special thanks to Dr. Michael Dearnaley for his very generous assistance for proof-reading this thesis.

I also wish to express my gratitude to all my friends in the Department of Oceanography who have offered encouragement over the last years; in particular Claire Burren, Sigrid Gellers-Barkmann and Veikila Vuki.

LIST OF CONTENTS

LIST OF FIGURES

LIST OF TABLES

CHAPTER 1

INTRODUCTION

1.1 Introduction

Results from observations and modelling of the upper ocean have suggested that there is a connection of equatorial anomalies to higher latitudes, through the ocean eastern boundaries, over time scales of a few months to years. The most important among these anomalies is the El Niño phenomenon.

To date most of the El Niño research has been concentrated in the equatorial Pacific where the main disturbances take place and from where the energy for changes elsewhere emanates. Oceanic models, developed to study El Niño phenomenon, frequently exclude higher latitudes and often have an artificial barrier just outside the tropics (Philander, 1990).

The El Niño-Southern Oscillation (ENSO) is thought to be the result of strong and complicated coupling between the ocean and the atmosphere in the tropics. In order to explore this idea several coupled models have been developed in the past few years with different dynamical complexity. McCreary and Anderson (1991) provide a recent overview of coupled ocean-atmosphere models of ENSO.

The principal purpose of research in this field is to forecast ENSO events. However, rather than attempt to simulate the ENSO the foremost interest in this study is in the low-frequency variations of the eastern ocean boundaries, during the El Niño years, induced by a single candidate mechanism: the remotely forced equatorial Kelvin wave.

Section 1.2 of this chapter addresses very briefly the ENSO phenomenon. No attempt is made to describe the ENSO phenomenon in detail. In the following sections an overview of the relevant observations are presented. This chapter concludes with a statement on the approach and aims of this study.

1.2 El Niño-Southern Oscillation (ENSO)

In 1983, the Scientific Committee on Oceanic Research (SCOR, 1983) defined El Niño as follows: El Niño is the appearance of anomalously warm water along the coast of Ecuador and Peru as far south as Lima (12°S), during which a normalized sea surface temperature (SST) anomaly exceeding one standard deviation occur for at least four consecutive months at three or more of five coastal stations (Talara, Puerto Chicama, Chimbote, Isla Don Martin and Callao).

The atmospheric counterpart to the El Niño is the Southern Oscillation (SO). The SO is a coherent variation of barometric pressure, on an interannual time scale, which is related to weather phenomena over large areas of the globe, particularly in the tropics and subtropics.

A helpful index of the SO is the anomalous atmospheric pressure difference between Darwin (representative of the Indonesia low) and Easter Island (representative of the South Pacific high) (Philander, 1990). Time series of this pressure difference indicate that this index, the SOI, drops to a minimum during each El Niño event. It has been found that the SOI is remarkable well correlated with such diverse quantities as sea-level pressure, air temperature, sea-surface temperature, precipitation and sea level, at a variety of locations (Gill, 1982).

Because the causal relationship between the pressure fluctuations of the SO and the anomalous warm water of the El Niño remains unclear, both phenomena are now considered together as a single phenomenon called ENSO (Cane and Sarachick, 1983).

Before 1972 the adverse effects of the ENSO phenomenon were recognized only in South America, especially Peru. Following the 1972-1973 El Niño it was further realized that El Niño may have important impacts throughout the world (Enfield, 1989).

ENSO is such a large scale event that it is considered to cause decreased hurricane activity in the Atlantic, droughts in Indonesia, India, the Philippines, Australia, Northeast Brazil, Ethiopia and southern Africa, as well as other regions. It has also been associated with floods in southern Brazil, Peru and Ecuador, mild winters in eastern Canada, cool summers in northeast China and many other anomalous weather conditions. The large scale biological consequences of ENSO are also many and very complex (see Barber and Chavez, 1983).

Glantz et al.(1990), examining the environmental and societal aspects of the El Niño phenomenon, observed that climate-related health problems, including famine, epidemics, death and injury from wildfire, flood or storm surge, connected to the El Niño events, are not limited to the tropical regions but can be linked throughout the globe.

A comprehensive compilation of ENSO events is presented by Quinn et al.(1987). They have reviewed historical publications to obtain information on El Niño over the past four and a half centuries. The ENSO events were classified as weak, moderate, strong or very strong depending on several factors, such as intensity and economic impact. However, as pointed out by Philander (1990), despite the amplitudes of different ENSO events varying significantly, the phases of different episodes may be remarkably similar. Because of this, composite analysis is possible.

Rasmussen and Carpenter (1982), using composite analysis, gave a detailed description of the sequence of events in the ENSO phenomenon over the Pacific. They combined the data for the three years: before, during and following each of six El Niño episodes that occurred between 1951 and 1973 (1951, 1953, 1957, 1963, 1965 and 1972).

The composite El Niño, however, provides only a general model of processes that are common to most ENSO events. The 1982-1983 El Niño, for example, exhibited some discrepancies from the composite El Niño. The 1982-1983 ENSO event and its peculiarities have been extensively discussed by Cane (1983) and Rasmusson and Wallace (1983), among others.

Wyrtki (1975) explained the onset of the ENSO as a dynamic response of the equatorial Pacific ocean to atmospheric forcing: the interannual equatorial Pacific trade wind anomalies cause the accumulation of upper layer water in the west (strong trades) and its subsequent tendency to return eastward (weak trades) in the form of equatorially trapped internal Kelvin wave packets. The sea level changes are baroclinic; there is comparatively little change in pressure at the bottom of the ocean associated with these events. These ideas have been expanded by several researches and validated in a set of numerical experiments.

Upon impingement with the eastern boundary, the incoming baroclinic equatorial Kelvin wave excites westward-propagating internal Rossby waves and poleward-propagating coastal Kelvin waves (Moore, 1968; Moore and Philander, 1977; McCreary, 1976). White and Saur (1983) have observed interannual baroclinic long waves propagating westward associated with coastal sea level variability south of 30°N. Thus, remote forcing may play an important role in the dynamics of the coastal regions off North and South America through the equatorial and coastal wave guides.

Moore et al. (1978) have also hypothesized that cold SST in the Gulf of Guinea during the coastal upwelling season is the result of a coastal Kelvin wave, which, through a complex series of events involving equatorial waves, is excited by changing winds in the western equatorial Atlantic.

The tropical Atlantic has a counterpart to El Niño phenomenon (quasi El Niño), such an event occurred in 1984 when sea surface temperatures off southwestern Africa were exceptionally high (Philander, 1990; Verstraete, 1992).

In addition to the theoretical model results, there is observational evidence for the propagation of baroclinic disturbances along the equator and the eastern boundaries.

1.3 Observational evidence of equatorially-trapped Kelvin waves

The equatorial Kelvin waves are thought to occur over a wide range of frequencies. Sea level records from El Niño years reveal that sustained periods of high sea level were composed of several wave periods, which were interannually modulated.

Several observations show eastward phase propagation along the equator but it is difficult to find measurements that unambiguously show the presence of Kelvin waves. According to Philander (1990), this is because the waves are superimposed on other waves and on time-dependent wind-driven currents which have no dispersion relation.

1.3.1 Pacific Ocean

On interannual time scales, the prominent disturbances of sea level elevation in the equatorial Pacific Ocean related to known occurrences of the El Niño phenomenon are associated with the SO.

The shortage of available measurements suitable to study the interannual oceanic variability impedes a reliable quantitative description. Interannual variability has such a large amplitude that the definitions of mean conditions and of the climatological seasonal cycle depend heavily on the period over which the data was collected (Philander, 1990). Observational evidence for forcing of higher frequency modes (intraseasonal periods, for example) is most common, but even this data is sparse.

Intraseasonal fluctuations of 40- to 60-day periods have been observed in sea level records of the equatorial Pacific and were shown to be Kelvin waves forced in the western equatorial Pacific by the "Madden-Julian oscillation" (hereinafter MJO). The MJO is a large-scale, eastward propagating signal characterized by a 30 to 60 day spectral peak in the variance and coherence of near-equatorial tropospheric wind, pressure and convection (Madden and Julian, 1971, 1972).

There have been many studies of the MJO, but many of its characteristics remains unexplained. Weickman (1991) has shown that for the developing 1982-1983 ENSO interannual transitions in the anomalous atmospheric circulation and in the sea surface temperatures in the western-central Pacific coincide with the passage of strong MJOs from the Indian to Pacific Oceans.

According to Enfield (1989), it may be that the MJO is only effective as a trigger that trips a preconditioned ocean-atmosphere system into an El Niño state. Or it may be that the oscillation is decoupled from the ENSO sequence and merely modulates the observed anomalies.

As pointed out by Glantz et al.(1990), the presence of the MJO waves in the tropical Pacific suggests that it may be impossible to predict the early stages of an El Niño event on a month-to-month basis. It seems likely that these waves could advance or retard the discernable onset of an event by a month. If so accurate prediction of monthly SST anomalies would require that the pattern of 30-60 day activity be predicted as well.

Enfield (1987), using time series of sea level elevation for the period of 1979-1985, has documented intraseasonal fluctuations of 40- to 60-day period in sea level propagating eastward across the equatorial Pacific as a baroclinic Kelvin wave forced in the western equatorial Pacific by the MJO.

Ripa and Haynes (1981) observed low-frequency fluctuations at the Galapagos Islands of intraseasonal period (about 100 days) with meridional structure consistent with a first baroclinic mode Kelvin wave.

Strong observational evidence of the Kelvin wave is provided by Knox and Halpern (1982). They filtered out some of the variability integrating the zonal currents vertically and a pulse propagating nondispersively from the central to the eastern equatorial Pacific at speed of 2.9 m/s was revealed.

McPhaden and Taft (1988), analysing time series measurements from surface moored buoys in the eastern and central equatorial Pacific for the period 1983-86, have found intraseasonal eastward propagating baroclinic Kelvin-like waves at periods of 60-90 days, which were poorly correlated with the local winds.

Two years of GEOSAT (GEOdetic SATellite) altimetric sea-level data were used by Miller et al.(1988) to investigate the tropical Pacific Ocean before and during the 1986-87 El Niño. Sea level time series along the equator showed both positive and negative interseasonal anomalies propagating eastward across the Pacific with phase speeds of 2.4 to 2.8 m/s, suggesting downwelling and upwelling Kelvin waves, respectively.

Using GEOSAT sea level and surface current anomalies of 1986-1987 Delcroix et al.(1991) have shown evidence of an equatorial Kelvin wave with the characteristics of a first baroclinic mode propagating over most of the equatorial Pacific basin.

1.3.2 Atlantic Ocean

In the Atlantic Ocean, observations suggest that the upwelling event in the Gulf of Guinea is not associated with either the local winds or the local ocean circulation (Houghton, 1976). A possible explanation is that a strong upwelling signal, generated by increased westward wind stress in the western Atlantic, can travel as an equatorially trapped Kelvin wave (Moore et al., 1978; Adamec and O'Brien, 1978; Servain et al., 1982; Busalacchi and Picaut, 1983; Picaut, 1983; McCreary et al., 1984). This interpretation is analogous to theories of El Niño in the Pacific Ocean.

Long-term inverted echo sounder records along the equator in the Atlantic were analyzed by Katz (1987) to show the dominance of equatorially trapped and eastward propagating disturbances with first baroclinic mode Kelvin wave characteristics. The propagation speed was estimated to be between 2.1 and 2.6 m/s along the equator.

Verstraete (1992), analysing both historical data and the FOCAL hydrographic stations (1982-1984) has related the equatorial downwelling-upwelling in 1984 in the Gulf of Guinea to the remotely forced equatorially trapped Kelvin wave.

1.4 Observational evidence of long wave propagation along the eastern ocean boundaries

The low frequency response of sea level on the eastern boundaries can be subdivided for linear purposes into two independent constituents (1) the remotely forced part, e.g., that which is the result of equatorial Kelvin waves incident on the boundary, and (2) the locally forced part. The latter is due to the longshore component of the wind (Bigg and Gill, 1986).

Observational and theoretical studies, however, have indicated that the remotely forced part dominates the sea level variability along the ocean eastern coasts.

1.4.1 Pacific Ocean

Reported results along the eastern coast of North and South America suggest that much of the oceanographic variability along these eastern ocean boundaries is of equatorial origin. Evidence for wave propagation along the eastern boundary of the Pacific Ocean can be seen in records of coastal sea-level elevation.

Enfield and Allen (1980), based on a 25 year time series of coastal sea level from Chile (33°S) to Alaska (60°N), have found coherency in the interannual sea level fluctuations at most of the stations, especially those at low latitude, i.e., from Matarani to San Francisco (see Figure 1.1). The El Niño events (high sea level) can be readily identified: 1951, 1953, 1957-58, 1963, 1965-66, 1969 and 1972-73. Shorter period fluctuations are found to be visually coherent between neighbouring stations or within regional groups (e.g., Crescent City to Yakutat, Galapagos to Matarani). The interannual fluctuations typical of El Niño events are shown clearly at the four stations from Galapagos to Matarani where, in particular, a double peaked structure of the large El Niño events is evident. The interannual anomalies, associated with El Niño variability, exhibited a poleward propagation from equatorial regions in both Hemispheres with properties similar to those of internal Kelvin waves. For the Northern Hemisphere the phase speed of 180±100 km/day (0.9 to 3.2 m/s) was established. In the Southern Hemisphere a phase speed of ~35-50 km/day (0.4 to 0.6 m/s) was estimated. Because of the limitation of the data in the Southern Hemisphere this result was considered by the authors as being ambiguous.

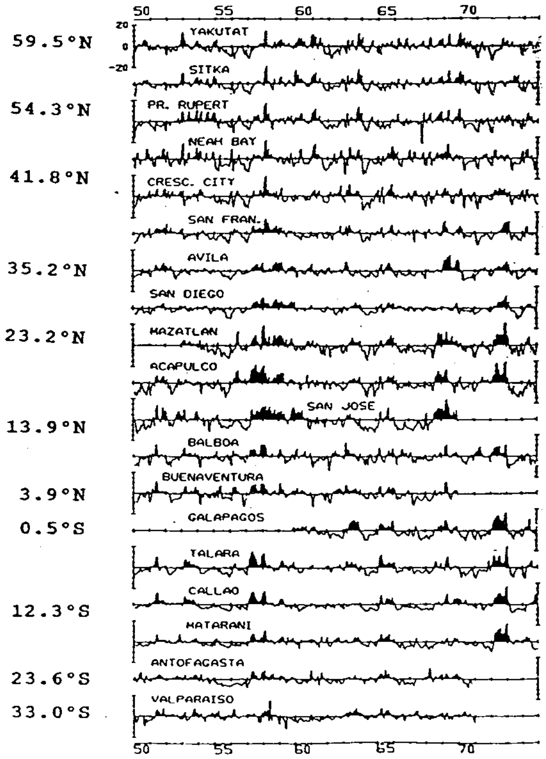

FIGURE 1.1: Time series of monthly anomalies of sea level from 1950 to 1974, inclusive. Positive anomalies are shaded black. [from Enfield and Allen, 1980].

Chelton and Davis (1982) have examined 29 years of nonseasonal, monthly-mean, tide-gauge sea level data along the west coast of North America. It was verified that the interannual aspects of the large scale sea level variability in the eastern tropical Pacific are closely related to El Niño occurrences, which appear to propagate poleward with phases speed of ~0.4 m/s. Higher frequency (monthly) aspects of this large scale sea level variability were attributed to direct effects of atmospheric forcing over the North Pacific.

Pares-Sierra and O'Brien (1989), identified a major source of sea level variability along the coast of North America to be poleward propagating baroclinic Kelvin waves of interannual periods.

Johnson and O'Brien (1990) have shown that baroclinic coastal Kelvin waves are the dominant factor for the mid-latitude El Niño of the North American coast at interannual and annual periods. The influence of the coastal Kelvin waves was found to diminish poleward of 45°N. At seasonal time scales, the acceleration of the local wind appeared as an important mechanism in driving coastal currents.

Spillane et al.(1987), using sea level records at coastal stations from Peru to British Columbia for the period 1971-1975, have found oscillations associated with the 1972-1973 El Niño with intraseasonal periods of 36-73 days. These oscillations were shown to be coherent from near the equator north to 34°N and south to at least 12°S. The amplitude and phase variations were consistent with propagation as free coastally trapped waves with a poleward phase velocity of 150-200 km/day (1.7 to 2.3 m/s), in the Northern Hemisphere.

1.4.2 Atlantic Ocean

Servain and et al. (1982) have presented evidence, based on historical SST and wind data, indicating that remote forcing in the western equatorial Atlantic Ocean is an important factor affecting the eastern equatorial Atlantic SST.

Picaut (1983), analysing historical monthly mean SST, showed that the seasonal coastal upwelling in the eastern Atlantic propagates poleward, starting from the equator, at a mean speed of 0.7 m/s in both Hemispheres. It was suggested that remote forcing west of the Guinea Gulf is an important factor affecting the temperature in the Gulf.

1.5 Approach and Aims

This study assumes the most widely accepted theory for the oceanic response during El Niño events: namely that the changes at the eastern Pacific coast are caused by changes in the zonal wind stress in the central Pacific and that their influence is transmitted across the Pacific by equatorial baroclinic Kelvin waves.

The main aims of this study are:

(1) The development of the shallow water model to explore the reflection of the low frequency baroclinic equatorial Kelvin wave at eastern oceanic boundaries;

(2) An investigation of the behaviour of these equatorial Kelvin waves when they reach the eastern oceanic boundaries. It addresses the questions:

- How far from the equator can the baroclinic disturbances propagate?
- How important is the coastline orientation on the propagation of the coastally trapped Kelvin waves and on the generation of the reflected Rossby waves?
- How important are the viscous effects on the studied waves?
- What are the main differences between propagation in the Northern and Southern Hemispheres of the Pacific and Atlantic Oceans?
- What occurs when the frequency of the incident equatorial wave changes?

Chapter 2 presents some analytical theory used in this study. The baroclinic shallow water equations are used as the basis for investigating the reflection of the equatorial Kelvin waves at the eastern ocean boundaries.

The shallow water model is developed in Chapter 3 and its numerical details are presented in the Appendix.

Chapter 4 explores the problem of equatorial low frequency wave reflection at hypothetical eastern boundaries. Energy fluxes generated by reflection of equatorial Kelvin waves of different periods at different eastern boundaries are investigated.

The development and results of more realistic experiments are described in Chapter 5. In that chapter the numerical eastern boundaries simulate the Pacific and the Atlantic ocean coastlines.

In Chapter 6 the main results of this study are discussed and further factors which may influence low frequency wave propagation are presented.

Chapter 2

THEORETICAL CONSIDERATIONS

2.1 Introduction

In this chapter some analytical theories relevant to the phenomena studied are briefly discussed. These theories will be frequently referred to in the subsequent chapters.

Most of the subjects discussed in this chapter can be applied to any equatorial ocean. Special attention, however, is devoted to the Pacific ocean because of its relationship with the El Niño phenomenon.

Earlier studies have alluded to the importance of equatorial phenomena on the ENSO events. The general characteristics of the equatorial dynamics on large time scales may be explored considering a simple reduced-gravity shallow water model (Section 2.2). The one-layer model represents an attempt to produce the simplest possible model that can be used to study baroclinic motion. Simple models can be of considerable value because the results obtained using them can provide insight into situations where more complex physical processes are at work.

The phenomenon of the equatorially trapped wave, one relevant feature of equatorial dynamics, is described in Section 2.3. The equatorial waves in the presence of a zonal boundary near the equator is addressed in Section 2.4.

Theoretical and observational studies have shown that equatorially trapped internal Kelvin waves may generate, upon reflection on the eastern coast, a poleward propagating disturbance along this boundary. Thus, poleward propagating waves generated in the tropics during a ENSO episode, for example, should carry information to the extratropical regions. The question of reflection at eastern coasts is addressed in Section 2.5. Section 2.6 discusses the criteria for validity of the equatorial β-plane approximation.

2.2 The reduced-gravity shallow water model

Shallow water models have proved extraordinarily useful for explaining equatorial phenomena on long time scales (Cane and Patton, 1984).

The reduced-gravity approach has often been used in models of tropical oceans (McCreary, 1977; Adamec and O'Brien, 1978; Cane, 1979; among others). Such a model is capable of reproducing observed sea level variability in equatorial regions and also along the eastern oceanic boundaries (Johnson and O'Brien, 1990; Bigg and Inoue, 1992).

Meyers (1979) has shown, using sea level and interfacial depth profiles, that during most of the year the eastern tropical Pacific acts in a manner compatible with the dynamics implicit in the reduced-gravity approach. The profiles show that variations in the sea level and 14°C isothermal depth are 180° out of phase. This phase relation allows a zero pressure gradient to exist below the upper layer. The general assumption is that a warm sea surface temperature anomaly is associated with a depressed thermocline and, conversely, that an upwelling thermocline occurs with a cool SST anomaly.

In the model, the interface between two immiscible layers of fluid, each of constant density, simulates the thermocline that separates the warm surface water from the cold waters of the deep ocean. The upper layer has density ρ_1, a mean depth H, and is bounded above by a rigid lid. The lower layer has density ρ_2 and is infinitely deep. Linear hydrostatic motion in the upper layer is associated with a displacement h of the interface and is described by the linear shallow water equations (McCreary, 1976):

$$\frac{\partial u}{\partial t} - fv + g^* \frac{\partial h}{\partial x} = 0 \qquad (2.2.1a)$$

$$\frac{\partial v}{\partial t} + fu + g^* \frac{\partial h}{\partial y} = 0 \qquad (2.2.1b)$$

$$g^* \frac{\partial h}{\partial t} + c^2 \left(\frac{\partial u}{\partial x} + \frac{\partial v}{\partial y}\right) = 0 \qquad (2.2.1c)$$

The velocity components in the eastward (x) and northward (y) directions are u and v, respectively. The Coriolis parameter is $f=\beta y$, where $\beta=2\Omega/r$. Here Ω denotes the rate of rotation of the earth and r its mean radius. The gravitational acceleration g, because of stratification, is effectively reduced to

$$g^* = \frac{\rho_2 - \rho_1}{\rho_2} g \qquad (2.2.2)$$

and the gravity wave speed is $c=(g^*H)^{1/2}$.

The free wave solutions to Equations (2.2.1) are of four types: Kelvin waves, Rossby waves, inertia-gravity waves and mixed Rossby-gravity waves (Cane and Sarachik, 1976). "Free-waves solutions" are understood to be solutions to Equations (2.2.1) without forcing and that have u, v and h proportional to:

$$\exp(ikx - i\sigma t) \qquad (2.2.3)$$

where the zonal wavelength is $2\pi/k$ and the frequency is σ.

Equations (2.2.1) may be combined to form a simple equation for the northward velocity component. The resultant expression together with Equation (2.2.3) reduces it to the ordinary differential equation:

$$\frac{\partial^2 v}{\partial y^2} + \left(\frac{\sigma^2}{c^2} - k^2 - \frac{\beta k}{\sigma} - \frac{\beta^2 y^2}{c^2}\right) v = 0 \qquad (2.2.4)$$

A significant property of the solutions of Equation (2.2.4) is the equatorial trapping; i.e., waves are guided along an equatorial waveguide. The waveguide effect is due entirely to the variation of the Coriolis parameter with latitude (Gill, 1982).

Note that for a wave of fixed frequency σ and fixed east-west wavenumber k, the coefficient of v in Equation (2.2.4) may be positive at the equator, giving wavelike behaviour, but as $|y|$ increases, $f=\beta y$ increases, and the coefficient of v decreases until it becomes zero at the *critical latitude* (see Section 2.5.1). At latitudes higher than the critical one, the coefficient of v becomes negative and solutions of Equation (2.2.4) become exponential in character, thus giving wave trapping.

2.3 Equatorially trapped waves

An important geographical area as far as the oceans are concerned is the equatorial region, where at the equator itself, the Coriolis parameter vanishes. One relevant feature of equatorial dynamics is the phenomenon of the equatorially trapped wave - a narrow band of latitudes centred on the equator which acts as a waveguide for westward propagating planetary waves and zonally propagating long gravity waves (LeBlond and Mysak, 1978).

Equations (2.2.1) describe linear waves on an equatorial β-plane. For given values of σ and k, Equations (2.2.1) constitute an eigenvalue problem. If the solutions are required to be bounded at large distances from the equator, then modes are possible only for a certain discrete values of the meridional wave number n that are eigenvalues of Equation(2.2.4). These eigenvalues are given by the expression (Philander, 1979):

$$\frac{c}{\beta}\left(\frac{\sigma^2}{c^2} - k^2 - \frac{\beta k}{\sigma}\right) = 2n+1 \qquad n=0,1,2... \qquad (2.3.1)$$

The full dispersion relation for equatorially trapped modes is shown in Figure 2.1, with frequency, σ, in units of $(\beta c)^{1/2}$, and the zonal wave number, k, in units of $(c/\beta)^{1/2}$. The Kelvin wave is represented by the straight line labelled n=-1. Trapped equatorial Rossby waves appear as low-frequency, negative-k curves having modal numbers n = 1,2,3,...

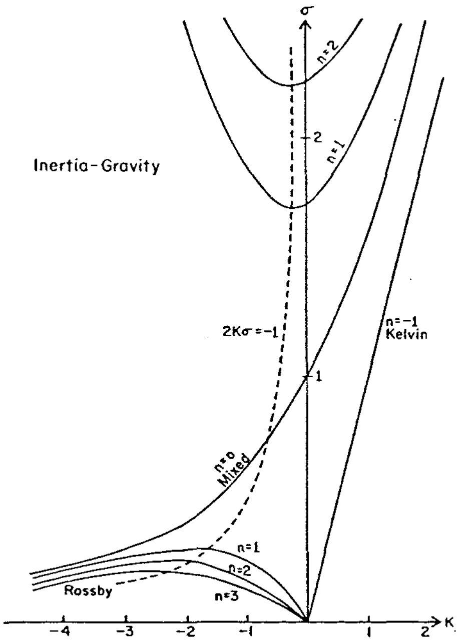

FIGURE 2.1 - Dispersion diagram for equatorially trapped modes. The unit of frequency is $(\beta c)^{1/2}$ and the unit of zonal wave number k is the inverse of the radius of deformation $(c/\beta)^{1/2}$. [From Cane and Sarachik, 1976].

The group velocity $c_g = \partial\sigma/\partial k$ may be calculated from the dispersion relation (2.3.1). Equation(2.3.1) gives two curves for each value of n: one for inertia-gravity waves and the other for Rossby waves. Those with n even have u and h components which are antisymmetric and v components which are symmetric about the equator; those indexed by odd n have opposite symmetries. Also, the smaller n is, the more equatorially confined is the mode.

2.3.1 "Mixed" Rossby-gravity waves

According to Equation (2.3.1) there are two apparent roots for $n=o$. The first root $(k=-\sigma/c)$ must be discarded because the corresponding u and h functions become unbounded when $y \rightarrow \infty$. The other root (labelled $n=o$) is known as the Rossby-gravity mode because it is similar to inertia-gravity waves at high frequencies and similar to Rossby waves at low frequencies. In the literature this mixed wave is often referred to as a Yanai wave. It has the dispersion relation:

$$k = \frac{\sigma}{c} - \frac{\beta}{\sigma}$$

The phase velocity may be eastward ($k>0$) or westward ($k<0$) but the group velocity is always eastward.

The case $k=0$ corresponds to a standing wave for which the surface moves sinusoidally up and down on opposite sides of the equator. Particles move anticyclonically with eastward phase when the free surface is elevated and westward phase when it is depressed. The frequency of the standing wave is:

$$\sigma = (\beta c)^{1/2}$$

For $n \geq 1$, both roots of Equation (2.3.1) lead to acceptable wave fields (see Figure 2.1).

2.3.2 Inertia-gravity waves

For the upper branches, the term $\beta k/\sigma$ in Equation (2.3.1) is small, so the dispersion curves are given approximately by:

$$\sigma^2 \approx (2n+1)\beta c + k^2c^2 \qquad n=1,2,3,\ldots$$

These waves are called equatorially trapped inertia-gravity waves and the lower the frequency of these waves, the more equatorially trapped they are. The group velocity can be to the east or west.

For long waves (k→0) the frequency is given by:

$$\sigma^2 = (2n+1)\ \beta c \qquad n=1,2,3,\ldots$$

Hence the minimum frequency of the inertia-gravity waves is $\sigma = (3\beta c)^{1/2}$, which for a phase speed of 2.5 m/s is $\sigma \sim 1.3\ 10^{-5}\ s^{-1}$, equivalent to a 5 ½ day period.

2.3.3 Rossby waves

On the lower branches of the curves, the term σ^2/c^2 in Equation (2.3.1) is small, and consequently the dispersion curves are given approximately by:

$$\sigma \simeq \frac{-\beta\ k}{k^2 + \frac{(2n+1)}{c}\beta} \qquad n = 1,2,3,\ldots$$

The corresponding waves are called equatorially trapped Rossby waves. These waves all have a westward phase speed.

The slow, short, dispersive waves have eastward group velocities and the fast, long, nondispersive waves have westward group velocities $c_g = c/(2n+1)$. For c = 2.5 m/s, $c_g \approx 0.83,\ 0.50,\ 0.36\ ms^{-1},\ldots$ The higher the meridional wave number, the further poleward the Rossby waves extend.

The long Rossby waves are very important in the oceanic adjustment to the ENSO phenomenon, whilst the inertia-gravity, Rossby-gravity and short Rossby waves are relatively unimportant.

2.3.4 Kelvin waves

Another interesting free response to Equations (2.2.1) is the flow when values of the meridional velocity are made equal to zero. With values of $v=0$, the equations of motion (2.2.1) simplify to:

$$\frac{\partial^2 u}{\partial t^2} - c^2 \frac{\partial^2 u}{\partial x^2} = 0 \qquad (2.3.2a)$$

$$f \frac{\partial u}{\partial t} - c^2 \frac{\partial^2 u}{\partial xy} = 0 \qquad (2.3.2b)$$

The first equation implies that:

$$u = E(y)\ F(x \pm ct) \qquad (2.3.3)$$

where E and F are arbitrary functions.

Disturbances propagate nondispersively either eastward or westward with speed c. Equation (2.3.2-b) determines the function E. It is unbounded at large values of y in the case of westward-propagating disturbances, which must therefore be ruled out. However, eastward equatorially trapped Kelvin waves are possible:

$$u = \frac{g^* h}{c} = e^{\frac{-y^2}{2R_e^2}}\ F(x - ct)\ , \qquad v=0 \qquad (2.3.4)$$

showing decay in a distance of order R_c.

For the case of wave disturbances $F=exp(ikx-i\sigma t)$, Equation (2.3.2-a) gives the dispersion relation:

$$\sigma = ck \tag{2.3.5}$$

Note that Equation (2.3.5) is also root of Equation (2.3.1) when $n=-1$, even through the latter equation is derived on the a-priori implicit assumption that $v\neq 0$. Because of this the equatorial Kelvin wave is sometimes called the $n=-1$ wave.

2.4 Effects of zonal coasts

In the presence of a zonal boundary near the equator, the Equation (2.2.4), which describes equatorial waves must be solved subject to the condition that the meridional velocity is zero at the latitude of the zonal boundary (Philander, 1990). Since the boundary conditions are no longer symmetric in this case the solutions lose their symmetry about the equator. Furthermore, two additional meridional wave modes are possible due to the overlapping radii of deformation for the equatorial and coastal regions: (1) a mixed Rossby-Kelvin wave and (2) a mixed Kelvin-gravity wave (Weisberg et al., 1979).

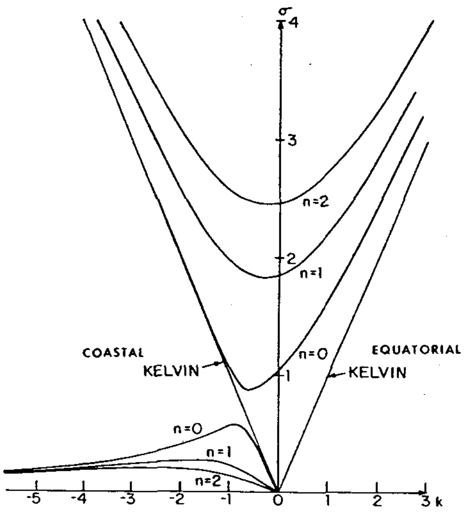

FIGURE 2.2: The dispersion diagram when a wall is present along a circle of latitude 1.7 radii of deformation north of the equator. The unit of frequency is $(\beta c)^{1/2}$ and the unit of wave number k is $(\beta/c)^{1/2}$. [from Cane and Sarachik (1979)].

Figure 2.2, from Cane and Sarachik (1979), shows the dispersion diagram when a wall is present along a circle of latitude 1.7 radii of deformation north of the equator

(~5°N). This is the approximate location of the northern coast of the Gulf of Guinea. The n=0 Rossby-gravity curve of Figure 2.1, which would have intersected the line for coastal Kelvin waves, now becomes two curves, for Kelvin-gravity and Rossby-Kelvin modes. Therefore, the tropical Atlantic may respond differently to forcing than the tropical Pacific Ocean.

2.5 Low frequency reflections at eastern coasts

Reported results along the coasts of North and South America suggest that much of the oceanographic variability along these eastern oceanic boundaries is of equatorial origin. According to the theory (Anderson and Rowlands, 1976; McCreary, 1976; Clarke 1983), the eastern boundary is an extension of the equatorial waveguide, and the reflection of low frequency waves incident on the boundary at the equator should be detectable at latitudes along the coast.

Evidence for wave propagation along the eastern boundaries is discussed in Section 1.4.

The unforced motion along the eastern boundary originates from incoming wave energy. For the large east-west scales anticipated at low frequencies in the ocean interior, the incoming energy must be in the form of equatorial Kelvin waves, because these are the only large east-west scale waves with eastward group velocity (see Figure 2.1). Therefore, energy accumulates at the eastern sides of equatorial ocean basins. The wave numbers k of the waves that should be available for reflection can be calculated from the dispersion relation (2.3.1):

$$k = \frac{\beta}{2\sigma} \pm \frac{1}{2}\left[\frac{\beta^2}{\sigma^2} - 4\left(\beta\frac{2n+1}{c} - \frac{\sigma^2}{c^2}\right)\right]^{\frac{1}{2}} \qquad (2.5.1)$$

At low frequencies, a Kelvin wave incident on an eastern boundary excites a finite number of long Rossby waves. In Equation (2.5.1) these waves are associated with the low values of n for which k is real.

Far from the equator, for y large and positive, the reflection of an equatorial Kelvin wave on an eastern boundary, at $x = L$, resembles coastally trapped waves (see Moore (1968) for details). The sum of the coastally trapped disturbances asymptotes, with increasing y, to the expression (Philander, 1990):

$$v = A\, y^{1/2} \exp\left[i\left(\sigma t - \frac{\sigma y}{c} + \frac{\beta x}{2\sigma}\right) - \beta y\, \frac{L - x}{c}\right] \qquad (2.5.2)$$

where A is a constant.

The response thus has some of the characteristics of a coastal Kelvin wave though no true Kelvin wave is present. It propagates poleward at speed c and is confined to a coastal zone with a width equal to that of the local radius of deformation $c/\beta y$. The wave differs from the classic coastal Kelvin wave because the velocity component normal to the coast is not zero and because the lines of constant phase are not normal to the coast. Although, in general, the energy of the coastal wave is not rigorously conserved (nor even rigorously defined) for short time scales, the loss to planetary waves and inertia-gravity waves beyond the radius of deformation of the coast may be neglected (Anderson and Rowlands, 1976). Conservation of energy then suggests that this initial disturbance must amplify as $y^{1/2}$ as it propagates away from the equator.

In short, when an equatorially trapped Kelvin wave from the western boundary impinges on a meridional boundary, part of the incident energy is reflected in the form of westward propagating Rossby waves. The remainder of the energy is divided equally (by symmetry) between northward and southward-propagating coastal Kelvin waves (Clarke, 1992).

These coastal waves provide a mechanism for energy to be lost from the equatorial region. But realistic ocean boundaries are not meridional ones and previous studies have shown that the inclination of the coast to the meridian can determine whether an incident Kelvin wave causes either coastally trapped waves or Rossby waves with group velocity away from the coast.

This question of low frequency reflection at a nonmeridional boundary has been studied previously by Schopf et al.(1981) and Grimshaw and Allen (1988) using ray theory analysis. They have shown, among other results, the strong dependence of the coastline inclination and the frequency of the incident wave on the behaviour of the wave reflection at the boundaries. A geometrical explanation of the phenomenon was also provided in those studies (see Section 2.5.1).

Clarke (1983, 1992) considered this same problem of reflection but using a low-frequency boundary-layer theory. The theory consists mainly of two parts. One discusses a near-boundary low frequency solution determined up to an arbitrary multiplicative constant, and the other shows how the arbitrary constant can be related to the incoming equatorial Kelvin wave. In this way the boundary and equatorial wave guide are linked and a complete near-boundary solution is available. It was also shown, using mathematical and physical arguments, that nonmeridional boundaries can play an important role in the low frequency reflection problem.

2.5.1 Critical latitude

The nature of the response at an eastern boundary to an incident baroclinic Kelvin wave at a single frequency σ depends on the magnitude of σ and on the latitude. For the low frequencies a critical latitude θ_c exists such that for $|\theta|<\theta_c$ the response consists of offshore-propagating Rossby waves, whereas for $|\theta|>\theta_c$ the waves are coastally trapped. The magnitude of θ_c depends on σ and on the angle of the coastline, decreasing as σ increases and as the orientation departs from the meridian (Grimshaw and Allen, 1988).

For a boundary making a constant angle γ with due north, a critical latitude θ_c can be defined as (Clarke and Shi, 1988):

$$|\theta_c| = \tan^{-1}\left[\frac{c\cos\gamma}{2\sigma r}\right] \qquad (2.5.3)$$

where r is the Earth's radius and c is the phase velocity.

Thus, as γ is increased, $|\theta_c|$ decreases and the latitude band over which Rossby waves radiate from the coast also decreases.

The strong dependence of the critical latitude on the coastline angle, is explained by Clarke (1992) in terms of potential vorticity. Particles near the boundary must move parallel to the boundary; so for a given frequency and velocity amplitude, the *more* the boundary inclines from the meridian the *less* planetary vorticity change an oscillating particle will experience. When the change in planetary vorticity is sufficiently large energy leaves the boundary as Rossby waves. Therefore, inclination of the boundary favours trapped motion.

Geometrically, the reflection of equatorial waves from a coast inclined to the meridian can be explained by Figure 2.3, where the circle is the dispersion diagram for the Rossby waves (see Longuet-Higgins, 1964). A wave incident on a north-south coast will reflect as a Rossby wave if its meridional wave number falls between points A and B in Figure 2.3. To reflect as a Rossby wave from a coast inclined at an angle γ to the meridian, the meridional wave number must fall between points C and D. Hence if the forced wave has a meridional wave number corresponding to point E, it will give rise to coastally trapped waves along the inclined coast but to Rossby waves in the case of a north-south coast (Philander, 1978).

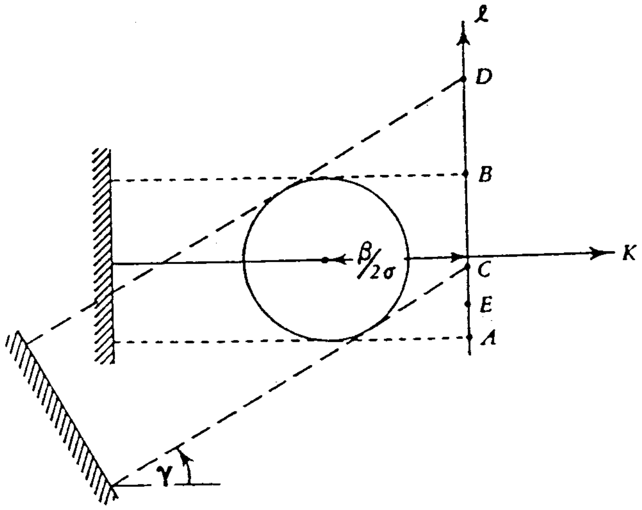

FIGURE 2.3: Dispersion diagram for the Rossby waves (from Philander, 1978).

In summary, mathematical, physical and geometrical arguments indicate that nonmeridional boundaries should be less reflective than meridional ones, and that the poleward coastal Kelvin wave energy flux should be greater the more the boundary inclines from the meridian. The eastern Pacific

Ocean boundary, for example, is less meridional in the Northern Hemisphere and, as consequence, the poleward coastally trapped energy flux should be greater in the Northern Hemisphere than in the Southern Hemisphere.

2.5.2 Energy flux

Energy flux is of primary importance in understanding reflection dynamics. In the context of equatorial waves, the eastward and westward energy fluxes, are due to, respectively, the equatorial Kelvin and the Rossby waves. The poleward energy flux along the boundary is due to coastal Kelvin waves.

The subsequent discussion follows Clarke (1992). According to Clarke, the nondimensional ratio $r_N(\gamma,\sigma)$, in %, of the northward coastal Kelvin wave energy flux to the incoming equatorial Kelvin wave energy flux for a boundary making a constant angle γ with due north is:

$$r_N(\gamma,\sigma) = 100 \cdot \frac{e\,\sigma}{(\beta c)^{1/2}\,\pi^{1/2}\,\cos\gamma} \quad (\%) \qquad (2.5.4)$$

where e=2.71828...

For constant γ, $r_S(\gamma,\sigma)$, the ratio of the southward coastal Kelvin wave energy flux to incoming energy flux is also given as in Equation (2.5.4).

By conservation of energy, the flux $r_W(\gamma,\sigma)$, the ratio of reflected Rossby wave energy flux to incoming equatorial

Kelvin wave energy flux is:

$$r_W(\gamma,\sigma) = 100. - \frac{200.\ e\ \sigma}{(\beta c)^{1/2}\ \pi^{1/2}\ \cos\gamma} \qquad (\%) \qquad (2.5.5)$$

Equation (2.5.5) indicates that Rossby wave reflection is decreased with increased slant of the boundary from meridional. This might be expected because, as γ increases, the critical latitude decreases (see Section 2.5.1).

When only one Hemisphere is considered, the ratio of reflected Rossby wave energy flux to incoming equatorial Kelvin wave energy flux is given by:

$$r_W(\gamma,\sigma) = 50. - \frac{100\ e\ \sigma}{(\beta c)^{1/2}\ \pi^{1/2}\ \cos\gamma} \qquad (\%) \qquad (2.5.6)$$

2.6 Equatorial β-plane approximation

The preceding Sections of this Chapter have used the governing equations on the equatorial β-plane. In this metric the effects of sphericity of the Earth are retained by approximating f, the local vertical (or radial) component of 2Ω, with a linear function of y, a latitudinal coordinate which is measured positive northward from the reference latitude. Therefore, the β-plane approximation consists solely of a set of geometric approximations.

As discussed by LeBlond and Mysak (1978), the β-plane approximation is valid if:

$$\frac{H}{r} << 1 \qquad (2.6.1)$$

$$\left(\frac{L}{r}\right)^2 << 1 \qquad (2.6.2)$$

$$\tan\theta_0 (L/r)^2 << 1 \qquad (2.6.3)$$

where L and H are, respectively, the characteristic horizontal and vertical length scale of the motion, r is the Earth's radius and θ_0 is the reference latitude.

The expression (2.6.1) considers that the motion occurs within a thin layer of fluid where the radial distortion in moving from one depth to another is negligible. Since $r = 6.4\ 10^6$ m and $H = O(5\ 10^3$ m) for the deepest ocean basins, $H/r = O(10^{-3})$, which conforms with (2.6.1).

Approximation (2.6.2) declares that the horizontal scale of the motion must be appreciably less than the Earth's radius. If L O(10^6 m) then $(L/r)^2 = O(10^{-2})$, which agrees with (2.6.2). If L is comparable with (or bigger than) the Earth's radius r, any solution for such large scale derived from β-plane equations is of questionable validity.

For scales $L \leq O(10^6$ m), $L/r = O(10^{-1})$ and hence the approximation (2.6.3) is valid provides that θ_0 corresponds to mid or low latitudes, so that $\tan\theta_0 \leq 1$. For the study of high latitudes a different approach involving spherical coordinates must be used.

When the approximations (2.6.1)-(2.6.3) hold and the motions are near the equator, it can be assumed that:

$$\sin\theta \approx \theta, \qquad \cos\theta \approx 1$$

giving the so called equatorial β-plane approximation. In this case β is a constant given by:

$$\beta = 2\Omega/r = 2.3\ 10^{-11}\ m^{-1}s^{-1}$$

and f is given by $f = \beta y$ where $y = r\theta$ is the northward distance from the equator.

CHAPTER 3

THE MODEL

3.1 Introduction

The reduced-gravity shallow water model has been frequently used in models of tropical and extratropical oceans, on intraseasonal, seasonal and interannual time scales.

In this chapter non linear, 1 ½ layer, shallow water equations are used as the basis of a numerical model. Approximations can be made to these equations in order to derive a linear 1 ½ layer model.

Nonlinear, reduced-gravity, 1 ½ layer models have been used successfully in the equatorial Pacific by Kubota and O'Brien (1988) and Johnson and O'Brien (1990) (hereafter referred to as the FSU model). This very well documented model has been shown to reproduce many of the observed upper layer features in the large-scale ocean.

The non linear numerical model, which has been developed in the present study, is similar to the FSU model. Both the models describe the same physical phenomena. The potential enstrophy-conserving discretization scheme used here is, however, different from that used in the FSU model. The present model, because of its numerical scheme, is more efficient in terms of computing time than the FSU model.

The time step required for linear stability for the numerical scheme used in this model is twice that for the FSU model. Thus, it signifies an important time saving factor for long-term numerical integrations.

Section 3.2 discusses the continuous form of the equations used in this work. The discrete form of the equations is given in the Appendix. The energetics of the shallow water motions are considered in Section 3.3. The boundary conditions applied to the numerical model are examined in Section 3.4. Section 3.5 summarizes the subjects presented in this chapter.

3.2 Dynamic equations: continuous form

3.2.1 Non linear equations

A one-layer, reduced gravity, fully non-linear model is used in this study. The model equations, for the upper layer, are as follows (Gill, 1982):

$$\frac{\partial u}{\partial t} + \frac{1}{r\cos\theta}\frac{\partial}{\partial\lambda}\left(\frac{u^2+v^2}{2}\right) - v(\zeta+f) = -\frac{1}{r\cos\theta}\frac{\partial P}{\partial\lambda} + A_H\nabla^2 u \qquad (3.2.1)$$

$$\frac{\partial v}{\partial t} + \frac{1}{r}\frac{\partial}{\partial\theta}\left(\frac{u^2+v^2}{2}\right) + u(\zeta+f) = -\frac{1}{r}\frac{\partial P}{\partial\theta} + A_H\nabla^2 v \qquad (3.2.2)$$

$$\frac{\partial h}{\partial t} + \frac{1}{r\cos\theta}\left\{\frac{\partial}{\partial\lambda}(uH) + \frac{\partial}{\partial\theta}(vH\cos\theta)\right\} = 0 \qquad (3.2.3)$$

Due to the large latitudinal extent of the model, spherical coordinates with λ (longitude) increasing eastward and θ (latitude) increasing northward are used in the model. As a shallow layer is being considered, r can be taken to be a constant equal to the radius of the earth.

Here $h(\lambda,\theta,t)$ is the interface displacement of the upper layer from the mean depth $H_0(\lambda,\theta)$; $H(\lambda,\theta,t)$ is the total depth ($H=H_0+h$); $u(\lambda,\theta,t)$ and $v(\lambda,\theta,t)$ are the horizontal components of the depth averaged velocity vector $\underline{v}(\lambda,\theta,t)$ in the λ and θ directions, respectively. f is the Coriolis parameter ($f= 2\Omega \sin\theta$). A_H is an eddy viscosity coefficient, used to parameterize processes not resolved in the model, for example, turbulent transfer of energy to scales smaller than the grid size.

ζ is the relative vorticity:

$$\zeta = \frac{1}{r\cos\theta}\left\{\frac{\partial v}{\partial \lambda} - \frac{\partial}{\partial \theta}(u\cos\theta)\right\} \tag{3.2.4}$$

P is the pressure integral:

$$P = g^* h \tag{3.2.5}$$

with the reduced gravity g^*:

$$g^* = \frac{(\rho_2 - \rho_1)}{\rho_2}$$

The Laplacian term is given by:

$$\nabla^2 u = \frac{1}{r^2\cos^2\theta}\frac{\partial^2 u}{\partial \lambda^2} + \frac{1}{r^2\cos\theta}\frac{\partial}{\partial \theta}\left(\cos\theta\frac{\partial u}{\partial \theta}\right) \tag{3.2.6}$$

$$\nabla^2 v = \frac{1}{r^2\cos^2\theta}\frac{\partial^2 v}{\partial \lambda^2} + \frac{1}{r^2\cos\theta}\frac{\partial}{\partial \theta}\left(\cos\theta\frac{\partial v}{\partial \theta}\right) \tag{3.2.7}$$

This system may be referred to as a "1 ½ layer" model. It consists of 1 dynamically active, incompressible, hydrostatic, homogeneous layer overlying an infinitely deep quiescent layer. The upper layer is treated as a shallow fluid of constant density. A property of the bottom layer thus defined is that horizontal pressure gradients and horizontal motions are everywhere vanishingly small. This assumption, known as the "rigid-lid approximation", results in the elimination of the barotropic mode (Charney, 1955; Veronis and Stommel, 1956). The effect of this approximation is to include pressure variations at the upper surface, but to exclude the kinematic effects of the surface variations with which the external inertia-gravity waves are filtered out with no distortion of the steady-state ocean circulation and very little distortion of low frequency motions (Bryan, 1969). Since external gravity waves move rapidly compared to other types of disturbances in the ocean, removing these high speed waves allows an order of magnitude increase in the time step.

3.2.2 Linear equations

The non linear Equations (3.2.1) - (3.2.3) can be linearized by considering motion of infinitesimal amplitude ($h<<H_0$) and $\underline{v}$ small enough that $\partial\underline{v}/\partial t \gg \underline{v}.\nabla\underline{v}$. Thus, terms of the form $\underline{v}\nabla\underline{v}$ and $h\nabla\underline{v}$ can be neglected. The validity of the linearization will depend upon the characteristic length, L, and velocity, U, scales with which the motion is associated.

Therefore, a linear version of Equations (3.2.1) - (3.2.3) is:

$$\frac{\partial u}{\partial t} - vf = -\frac{1}{r\cos\theta}\frac{\partial P}{\partial\lambda} + A_H\nabla^2 u \qquad (3.2.8)$$

$$\frac{\partial v}{\partial t} + uf = -\frac{1}{r}\frac{\partial P}{\partial\theta} + A_H\nabla^2 u \qquad (3.2.9)$$

$$\frac{\partial h}{\partial t} + \frac{H_0}{r\cos\theta}\left\{\frac{\partial}{\partial\lambda}u + \frac{\partial}{\partial\theta}(v\cos\theta)\right\} = 0 \qquad (3.2.10)$$

Equations (3.2.1)-(3.2.3) and (3.2.8)-(3.2.10) were translated into finite-difference form using a Richardson Lattice grid (see Section A.1 in the Appendix).

The time discretization scheme used in this study is described in detail in the Appendix. The scheme is a modification of the traditional forward-backward (FB) scheme: the gravity wave terms were discretized using a FB scheme (see Section A.2). The advective and Coriolis terms of the momentum equations were centred in time using the Adams-Bashforth scheme (see Section A.3). The viscous term was lagged in time, as usual, in order to keep the system stable.

3.3 Energetics of shallow-water motion

3.3.1 Non linear equation

Kinetic Energy - The kinetic energy equation can be obtained by multiplying Equation (3.2.1) by U=Hu and Equation (3.2.2) by V=Hv and adding the results. This gives:

$$\frac{\partial K}{\partial t} + \nabla . q\underline{V} + \frac{g^{*}U}{r\cos\theta}\frac{\partial h}{\partial \lambda} + \frac{g^{*}V}{r}\frac{\partial h}{\partial \theta} + D = 0 \qquad (3.3.1)$$

where, the divergent operator:

$$\nabla . \boldsymbol{F} = \frac{1}{r\cos\theta}\left(\frac{\partial F_{\lambda}}{\partial \lambda} + \frac{\partial}{\partial \theta}(F_{\theta}\cos\theta)\right)$$

the dissipative term (D) : $D = A_H\, H\, (u\nabla^2 u + v\nabla^2 v)$

and $q = (u^2+v^2)/2$; $\underline{V}=uH\underline{i} + vH\underline{j}$; and $K = q\,H$, being the kinetic energy per unit area.

Potential Energy - The potential energy equation is obtained by multiplying Equation (3.2.3) by $g^{*}h$, which results in:

$$\frac{\partial \Pi}{\partial t} + \frac{g^{*}h}{r\cos\theta}\frac{\partial U}{\partial \lambda} + \frac{g^{*}h}{r\cos\theta}\frac{\partial}{\partial \theta}(V\cos\theta) = 0 \qquad (3.3.2)$$

with $\Pi=g^{*}h^2/2$ being the potential energy per unit area.

Total Energy - The equation for non linear total energy (K+Π) is established adding Equations (3.3.1) and (3.3.2):

$$\frac{\partial}{\partial t}(K+\Pi) + \nabla .[(g^*h + q)\ \underline{V}] + D = 0 \qquad (3.3.3)$$

3.3.2 Linear equations

Kinetic Energy - The linear kinetic energy equation can be obtained by multiplying Equation (3.2.8) by H_0u and Equation (3.2.9) by H_0v and adding the results. This provides:

$$\frac{\partial K}{\partial t} + \frac{g^*H_0u}{r\cos\theta}\frac{\partial h}{\partial \lambda} + \frac{g^*H_0v}{r}\frac{\partial h}{\partial \theta} + d = 0 \qquad (3.3.4)$$

where,

$$d = A_H\, H_0\ (u\nabla^2 u + v\nabla^2 v)$$

and $K = H_0(u^2+v^2)/2$, the kinetic energy per unit of area.

Potential Energy - The linear potential energy equation is obtained, again, by multiplying Equation (3.2.10) by g^*h, to give:

$$\frac{\partial \Pi}{\partial t} + \frac{g^*h}{r\cos\theta}\frac{\partial H_0u}{\partial \lambda} + \frac{g^*h}{r\cos\theta}\frac{\partial}{\partial \theta}(H_0 v\cos\theta) = 0 \qquad (3.3.5)$$

Total Energy - The equation for the linear total energy is attained by adding Equations (3.3.4) and (3.3.5):

$$\frac{\partial}{\partial t}(K+\Pi) + \nabla .(g^*hH_0)\underline{v} + d = 0 \qquad (3.3.6)$$

with $\underline{v}=u\underline{i}+v\underline{j}$

3.4 Boundary conditions

One difficult problem when solving the hydrodynamic equations inside a bounded region is the formulation of correct boundary conditions. The open boundaries are generally difficult to place and their positions are often chosen based more upon computational cost than upon physical considerations. It is important to remember that these open boundary conditions will determine, together with the differential equations themselves, the form of the interior solutions, and if not carefully chosen they can lead to unrealistic solutions for the interior points (Castro, 1985).

After many experiments designed to test numerically different formulations for the open boundary conditions a modification of Orlanski's radiative boundary (Miller and Thorpe, 1981) was used in all open boundaries: north, south and west (see Sections 3.4.2 and 3.4.3), excluding corners.

It is assumed that close to the boundaries, excepting corners, the dependent variables satisfy the equation:

$$\frac{\partial A}{\partial t} + c\,\frac{\partial A}{\partial s} = 0 \qquad (3.4.1)$$

where, A is the dependent variable, c is the phase velocity and s is the direction normal to the open boundary.

The above equation may be discretized in a form compatible with the numerical scheme previously described:

$$\frac{A(B)^{(n+1)} - A(B)^{(n)}}{\Delta t} + c_B\frac{A(B)^{(n)} - A(B-1)^{(n)}}{\Delta s} = 0 \qquad (3.4.2)$$

where Δs is equal to either $\Delta\lambda$ or $\Delta\theta$ depending upon which direction (λ or θ) is normal to the open boundary; B indicates a point on the boundary , B-1 is the first point inside that boundary and n, n+1, indicate consecutive time levels.

Since $A(B)^{n+1}$ is the unknown of the problem c_B is actually evaluated at the point B-1:

$$c_{B-1} = -\frac{\Delta s}{\Delta t}\left[\frac{A(B-1)^{n+1} - A(B-1)^{n}}{A(B-1)^{n} - A(B-2)^{n}}\right] \tag{3.4.3}$$

Equation (3.4.3) is used in the model to estimate the phase speed of the waves approaching the boundary. The phase speed is then extrapolated to the boundary in order to find $A(B)^{(n+1)}$ from equation (3.4.2). The values allowed for the estimated phase speed are in the interval $(0,\Delta s/\Delta t)$. If the phase speed is negative, as in the case of a wave penetrating the boundary from outside the domain, the value of the dependent variable is extrapolated from the previous time step. If the estimated phase velocity is larger than $\Delta s/\Delta t$, then it is set equal to $\Delta s/\Delta t$, since numerically this last value corresponds to the fastest wave that the model can resolve.

In the model the open boundaries were located along lines where the velocity normal to that boundary was defined (see Figure A1). Therefore, excluding the corners, there is always one dependent variable located on each open boundary: the v velocity component on the northern and southern boundaries and the u velocity component on the western boundary. The other dependent variable (the interface displacement) was calculated using Equations (3.2.1)-(3.2.3), for the non linear case, or Equations (3.2.8)-(3.2.10), for the linear case, since it is actually located inside the model domain.

At the corners, where there are two dependent variables (u and v), the phase velocity c_{B-1} of Equation (3.4.3) was set zero. This procedure works well in this model because the phenomena generated inside the domain are certainly weak near the model corners. Wave motions are confined mainly to the equator and the coast.

With the present scheme perturbations generated inside the domain are able to cross the boundaries and leave the domain.

3.4.1 Solid wall boundary

On the solid boundaries the free-slip condition was used. It assumes that the tangential velocity outside the boundary is set equal to its adjacent counterpart inside the boundary. Section A.6, in the Appendix, discusses the use of the free-slip condition.

In the nonmeridional boundary experiments the four northernmost and the four southernmost points of the solid boundary are aligned in the meridional direction.

3.4.2 Southern and northern boundaries

The experiments testing the boundary condition (3.4.3) are now presented. Each one of these tests was carried out twice; first using a domain of interest (D) and second using a larger enclosed domain (2D). The ideal solution is one in which the interior flow is essentially identical to the solution within the larger domain.

All experiments reported in this section, have been performed using the model described above, considering only one layer of initial thickness H_0=200 m.

In the linearized form of the reduced gravity equations one can prescribe the linear phase velocity, $c=(g^*H_0)^{1/2}$. In the experiments described in this chapter, the phase velocity was taken to be 2.45 ms^{-1}. In the fully non-linear form, there is no analogous phase speed parameter. Prescribing the initial thickness, however, is analogous to prescribing an initial phase speed, but this can not remain constant as the model fields evolve, as the variations in h can be large compared to H_0.

A regular one-sixth degree resolution is used in both the zonal and meridional directions ($\Delta\lambda = \Delta\theta = 1/6°$). This grid spacing is less than the small baroclinic Rossby radius of the modeled region. Assuming the basin width for the wavelength *l* it results, for the highest latitude of the domain (θ=38°) in $\alpha\approx0.04$ and $\epsilon\approx0.006$ (see Section A6, for the coefficient definitions).

The experiments performed to test the northern and southern boundaries are very similar. In both procedures, a coastal Kelvin wave, generated on the opposite side (south or north) of the boundary to be tested (north or south), is allowed to pass through the latter boundary.

The numerical domains used in these experiments are:

$$\begin{array}{l}\text{northern}\\ \text{boundary}\end{array}\left\{\begin{array}{r}\text{D: } 22^\circ\text{N to } 30^\circ\text{N}\\[1ex] \text{2D: } 22^\circ\text{N to } 38^\circ\text{N}\end{array}\right. \quad \text{of latitude}$$

$$\begin{array}{l}\text{southern}\\ \text{boundary}\end{array}\left\{\begin{array}{r}\text{D: } 22^\circ\text{S to } 30^\circ\text{S}\\[1ex] \text{2D: } 22^\circ\text{S to } 38^\circ\text{S}\end{array}\right. \quad \text{of latitude}$$

and 4° of longitude from the coast.

Figures 3.1 to 3.4 show the time-latitude plots of the upper layer thickness (ULT) anomaly near the coast, resulting from these investigations. Kelvin wave propagation is evident in and all figures. The waves are propagating at a phase speed of approximately $|2.5|$ m/s in all domains.

The results of the northern boundary test are illustrated in Figures 3.1 and 3.2, in the D and 2D domain, respectively. These figures demonstrate that the Kelvin wave is able to pass through the artificial northern boundary without distortion and without affecting the interior solution.

Similar results were obtained for the southern boundary. Figures 3.3 and 3.4 display these test results performed in the D and 2D domains, respectively. Again the agreement between the two domains is remarkably good.

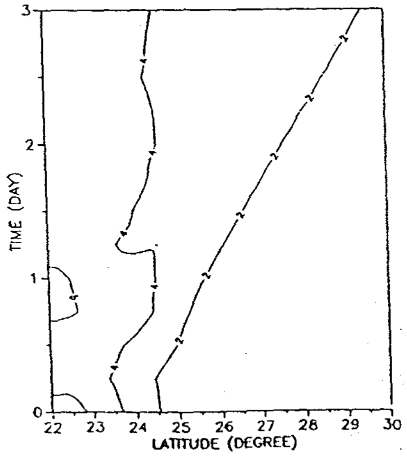

FIGURE 3.1: Time-latitude plot of ULT anomaly near the coast (metre), for the "D" domain. Northern boundary test.

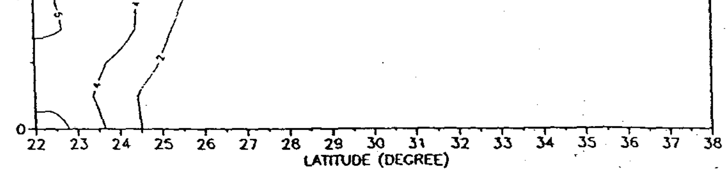

FIGURE 3.2: Time-latitude plot of ULT anomaly near the coast (metre) for the "2D" domain. Northern boundary test.

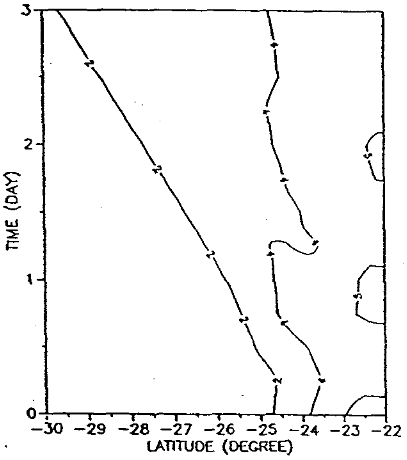

FIGURE 3.3: Time-latitude plot of ULT anomaly near the coast (metre) for the "D" domain. Southern boundary test.

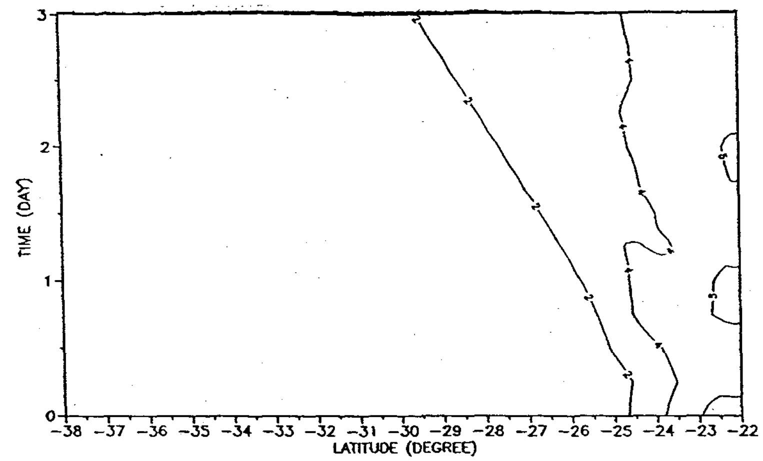

FIGURE 3.4: Time-latitude plot of ULT anomaly near the coast (metre) for the "2D" domain. Southern boundary test.

3.4.3 Western boundary

For the purpose of testing the western boundary of the model, a north-south slope of ULT is generated in the domain. The slope, in geostrophic equilibrium with the velocity, is used in the experiment as an initial condition. This gradient generates westward propagating disturbances, which are allowed to pass through the western boundary.

The domains used in this test are:

$$\begin{array}{l}\text{western}\\ \text{boundary}\end{array}\begin{cases}\text{D: }4^\circ\\ \text{2D: }8^\circ\end{cases}\text{of longitude from the coast}$$

and from 6°N to 6°S of latitude.

The results of this experiment are displayed in Figures 3.5 (D domain) and 3.6 (2D domain) as time-longitude plots along the equator. These plots demonstrate that the wave-like perturbations are transmitted through the western boundary without contamination of the interior solution.

The results obtained using the linear and non linear models were similar.

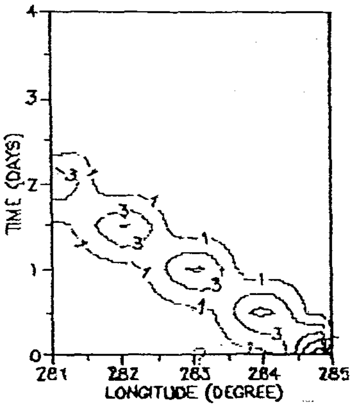

FIGURE 3.5: Time-longitude plot of ULT anomaly along the equator, for the "D" domain. Western boundary test.

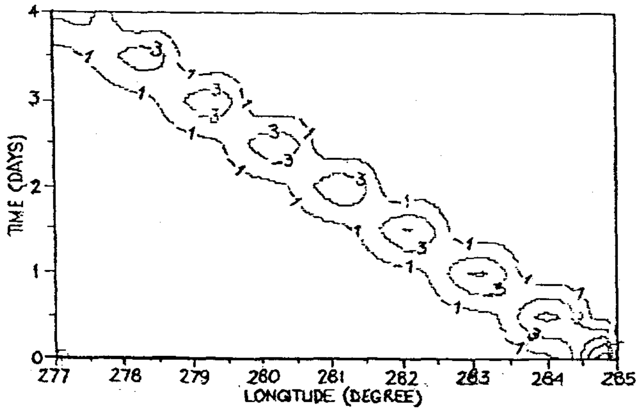

FIGURE 3.6: Time-longitude plot of ULT anomaly along the equator, for the "2D" domain. Western boundary test.

3.5 Summary

The numerical model presented in this chapter is a fast, efficient numerical procedure for modelling both linear and non linear, low frequency motions on the sphere.

The numerical model uses a numerical scheme which permits time steps twice those used in other discretization schemes, like the leapfrog for example. In addition, as a two level scheme, it has no computational mode in time. In the absence of forcing and viscosity the model conserves both potential vorticity and potential enstrophy but not total energy (see Appendix). Nevertheless, the numerical scheme utilized in the model permits long term integrations with negligible loss of energy. The model makes use of open boundary conditions which allow phenomena generated in the interior domain to pass through the artificial boundaries without distortion and without affecting the interior solution.

CHAPTER 4 - RESULTS

LOW FREQUENCY WAVE REFLECTION AT EASTERN BOUNDARIES

4.1 Introduction

Experiments were designed to study, numerically, the *free wave* solutions generated by low frequency wave reflection at meridional and nonmeridional eastern boundaries.

Baroclinic equatorial Kelvin waves generated in the western and central equatorial Pacific propagate eastward along the equator and finally hit the coast. As discussed in Chapter 2, at the coast the incident equatorial Kelvin waves are partially reflected back and partially transmitted north and south along the coast as coastally trapped internal Kelvin waves. Consequently the coastally trapped internal Kelvin waves "communicate", for example, the equatorial El Niño signals to higher latitudes. Hence it is important to know how far from the equator the baroclinic disturbances can propagate.

Previous analytical studies (the more relevant are mentioned in Section 2.5), have always excluded the effect of lateral viscosity, and employed approximations (β-plane, low-frequency wave, for example) to the governing equations in order to solve them analytically. Numerical solutions, however, can be obtained without these approximations. In practice, because of dissipative effects, there is a limit to the distance to which information is carried poleward by waves.

In past works, the numerical investigation of low frequency wave reflection at boundaries has always involved the *forced* solutions of the Equations (3.2.1)-(3.2.3) or (3.2.8)-(3.2.10).

Here, the effect of nonmeridional boundaries on baroclinic equatorial Kelvin wave reflection is investigated using the model outlined in Chapter 3. The mechanism of generation of the incoming equatorial Kelvin wave is not included in this study but the Kelvin wave could, for example, be set up at the western boundary by planetary waves.

All the numerical experiments reported hereafter have been performed using the model described in Chapter 3, considering one layer of initial thickness H_0= 200m. From the hydrostatic balance, a 10 cm surface elevation implies a 28 m depression of the interface (considering ρ_2=1060 and ρ_1=1025 Kg/m^3). The free parameters in the model, the phase velocity c and the dissipation coefficient A_H, are taken to be 2.45 m/s and 10^3 m^{2}s^{-1} (A_H is discussed in Section 4.7), respectively.

A baroclinic equatorial Kelvin wave is used as an initial condition for an ocean which is unbounded at western, southern and northern boundaries. The western side of the basin is considered as an open boundary in order to avoid reflection of the westward propagating long Rossby waves. Therefore, the whole solution of an experiment can be regarded as the result of the incident Kelvin wave reaching the eastern boundary.

To appreciate the reflection dynamics it is worth examining energy fluxes (described in Section 4.2). The numerical experiments, presented in Sections 4.3 to 4.5, were created to study the energy fluxes generated by reflection of an equatorial Kelvin wave of different periods: intraseasonal (60 days), seasonal (180 days) and annual (360 days) at different eastern boundaries.

The validity of the equatorial β-plane approximation for the cases studied is investigated in Section 4.6. Section 4.7 examines the numerical resolution of the model used in the above-mentioned experiments. The main results of this chapter are summarized in Section 4.8.

4.2 Energy flux

To estimate reflection properties, it is convenient to consider energy fluxes.

4.2.1 Linear

The linear shallow water total energy equation is given by Equation (3.3.6). Consider now a region bounded by an eastern ocean boundary and $\lambda=-\lambda_0$ and $\theta=\pm\theta_0$. Integrating Equation (3.3.6) over this region and from time 0 to time T, the following is obtained:

$$\begin{aligned}\int_{\substack{\theta=-\theta_0\\(\lambda=-\lambda_0)}}^{\theta=+\theta_0} \overline{g^* h H_0 u}\; r d\theta &= \int_{\substack{\lambda=-\lambda_0\\(\theta=+\theta_0)}}^{coast} \overline{g^* h H_0 v}\; r\cos\theta d\lambda \\ &- \int_{\substack{\lambda=-\lambda_0\\(\theta=-\theta_0)}}^{coast} \overline{g^* h H_0 v}\; r\cos\theta d\lambda - \int_{\lambda=-\lambda_0}^{coast} \int_{\theta=-\theta_0}^{\theta=+\theta_0} \overline{A_H H_0\ (u\nabla^2 u+ v\nabla^2 v)}\, r^2\cos\theta d\theta d\lambda\end{aligned} \qquad (4.2.1)$$

where the overbar denotes the time average.

If λ_0, $\theta_0 \rightarrow \infty$ in Equation (4.2.1) then physically it is implied that the net energy flux toward the coast is equal to the flux outward along the coast less the dissipation of energy in the domain.

For equatorial waves, the flux outward along the boundary is due to northward (t_N) and southward (t_S) coastal Kelvin waves. The net energy flux (t) toward the boundary is given by the difference between the energy fluxes due to the incoming equatorial Kelvin wave (t_E) and that due to the reflected Rossby waves (t_W).

Including the energy dissipation (t_D) and assuming that the energy flux is positive in the northward and the eastward directions, it can be stated that $t_E - t_W = t_N - t_S - t_D$ (see Figure 4.0).

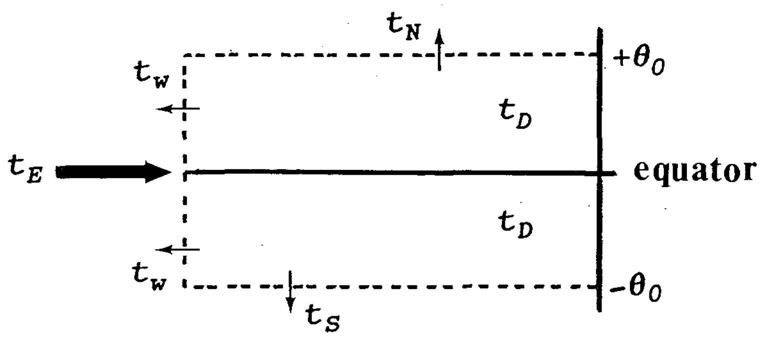

FIGURE 4.0: Energy flux and energy dissipation generated from $\theta=\theta_0$ to $\theta=-\theta_0$.

4.2.2 Non linear

The total energy, in the non linear case, is given by Equation (3.3.3). Again, integrating Equation (3.3.3) over a region bounded by an eastern ocean boundary and $\lambda=-\lambda_0$ and $\theta=\pm\theta_0$ and averaging in time, the following is obtained:

$$\begin{aligned}\int\limits_{\substack{\theta=-\theta_0\\(\lambda=-\lambda_0)}}^{\theta=+\theta_0} \overline{(g^*h + q)\,U}\, r d\theta &= \int\limits_{\substack{\lambda=-\lambda_0\\(\theta=+\theta_0)}}^{coast} \overline{(g^*h + q)\,V}\, r\cos\theta d\lambda \\ &- \int\limits_{\substack{\lambda=-\lambda_0\\(\theta=-\theta_0)}}^{coast} \overline{(g^*h + q)\,V}\, r\cos\theta d\lambda - \int\limits_{\lambda=-\lambda_0}^{coast} \int\limits_{\theta=-\theta}^{\theta=+\theta} \overline{A_H H(u\nabla^2 + v\nabla^2)}\, r^2\cos\theta d\theta d\lambda\end{aligned} \tag{4.2.2}$$

4.2.3 Numerical calculation

The energy fluxes and the energy dissipation were numerically calculated as indicated below. Equations (4.2.3), (4.2.4), (4.2.7) and (4.2.8) consider only one Hemisphere: the Northern Hemisphere. Changing $\theta=+\theta_0$ for $\theta=-\theta_0$ in those equations gives the Southern Hemisphere fluxes. Note that in all the numerical experiments performed in this work, the energy input is always considered for both Hemispheres and the poleward, westward and energy dissipations are always calculated for the Hemisphere under consideration.

The linear northward energy flux, across a given latitude $+\theta_0$ can be obtained by:

$$t_N = \sum_{\substack{\lambda=-\lambda_0 \\ (\theta=+\theta_0)}}^{coast} \overline{g^* h H_0 v}\; r\cos\theta\;\Delta\lambda \qquad (4.2.3)$$

and in the non linear case:

$$t_N = \sum_{\substack{\lambda=-\lambda_0 \\ (\theta=+\theta_0)}}^{coast} \overline{(g^* h + q)\, V}\; r\cos\theta\,\Delta\lambda \qquad (4.2.4)$$

The net linear energy flux toward the boundary, across a given longitude $-\lambda_0$, can be given by:

$$t = \sum_{\substack{\theta=-\theta_0 \\ (\lambda=-\lambda_0)}}^{\theta=+\theta_0} \overline{g^* h H_0 u}\; r\Delta\theta \qquad (4.2.5)$$

and in the non linear case:

$$t = \sum_{\substack{\theta=-\theta_0 \\ (\lambda=-\lambda_0)}}^{\theta=+\theta_0} \overline{(g^*h + q)U}\, r\Delta\theta \qquad (4.2.6)$$

The linear dissipation of energy, up to a given latitude $+\theta_0$, can be calculated as:

$$t_D = - \sum_{\lambda=-\lambda_0}^{coast} \sum_{\theta=0}^{\theta=+\theta_0} \overline{A_H H_0 \ (u\nabla^2 u + v\nabla^2 v)}\, r^2 \cos\theta\, \Delta\theta\, \Delta\lambda \qquad (4.2.7)$$

and in the non linear case:

$$t_D = - \sum_{\lambda=-\lambda_0}^{coast} \sum_{\theta=0}^{\theta=+\theta} \overline{A_H H(u\nabla^2 + v\nabla^2)}\, r^2 \cos\theta\, \Delta\theta\, \Delta\lambda \qquad (4.2.8)$$

4.3 Intraseasonal variability

To investigate the importance of the angle of inclination of the coast to the meridian an equatorial Kelvin wave of intraseasonal period (60 days) was used as an initial condition for the experiments with the numerical model.

Four different eastern boundaries are considered in the numerical domain. First, the whole eastern boundary is conceived to be a meridional one (γ=0°, hereafter Experiment C0). Second, the coastline is considered to be inclined at 40° from the meridian (γ=40°, hereafter Experiment C40), third it is inclined at 50° (hereafter Experiment C50) and finally, an inclination of 60° (hereafter Experiment C60) is used. In each case it is only the eastern boundary in the Northern Hemisphere that is inclined. In all experiments the Southern Hemisphere eastern boundary was considered to be meridional one. The geometry is shown in Figure 4.0.

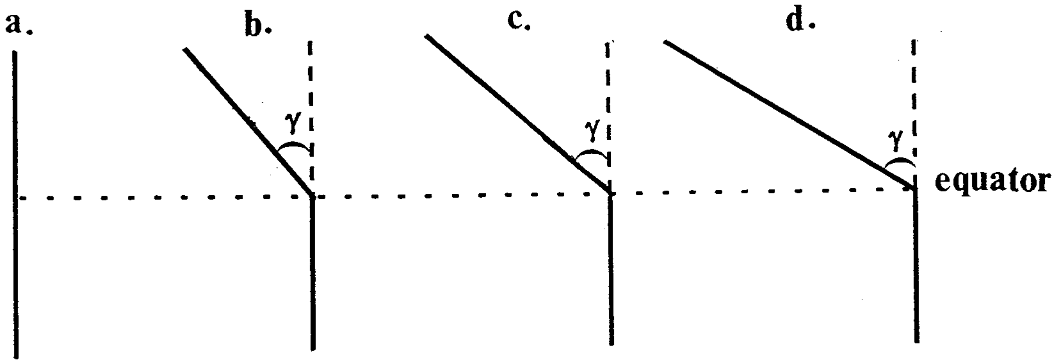

FIGURE 4.1: Model geometry. (a)γ=0°, (b)γ=40°, (c)γ=50° and (d)γ=60°.

The numerical experiment employs a model basin from 20°N to 20°S and maximum longitudinal extent of 70°.

Figure 4.2 displays the longitude-latitude plot of the initial interface anomaly (Z) used as the initial condition of the numerical model. It simulates a baroclinic equatorial Kelvin wave of 60-day period. A 60 day wave period was chosen because fluctuations of 40-60 day periods, related to ENSO phenomenon, have been found in sea level records of the eastern Pacific (see Section 1.4).

The height and velocity fields were initialised to represent a baroclinic equatorial Kelvin wave, and the time integration was performed to follow the evolution of that free wave propagating through the domain. The Kelvin wave energy is equipartitioned between potential and kinetic energy and therefore both height and velocity information are prescribed simultaneously for initialising the wave (see Anderson and Moore, 1985). The wave meridional structure was assumed to be a Gaussian function of latitude centred on the equator. Only a half wavelength of the equatorial Kelvin wave is used in the experiments because of limitations in computer resources.

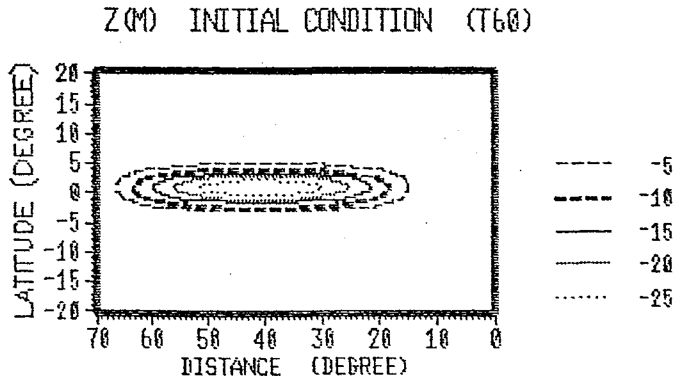

FIGURE 4.2: Initial interface anomaly used as initial condition (baroclinic equatorial Kelvin wave). Note that negative values of Z represent upwelling of the interface. Half wavelength. Wave period: 60 days. The zonal current is proportional to the meridional gradient of sea-level interface.

4.3.1 Linear case

The reflection of a low frequency baroclinic equatorial Kelvin wave at an eastern boundary of an ocean, according to Section 2.5, involves only poleward coastal Kelvin and westward Rossby waves. The Kelvin and Rossby wave responses, created at a meridional eastern boundary ($\gamma=0°$), are shown in Figure 4.3, where the latitude-longitude plot of the linear upper layer anomaly (Z) is displayed at six successive intervals of 15 days. An upward movement of the interface produces a negative height anomaly, indicating upwelling. The upwelling is symmetric in relation to the equator.

When the baroclinic equatorially trapped Kelvin wave reaches the coast, part of the incident energy continues poleward into either Hemisphere as coastally trapped Kelvin waves (deepened thermocline in Figure 4.3a). The remainder of the energy is reflected in the form of westward Rossby waves.

The Rossby waves are evident in Figure 4.3 as a closed contour, moving to the west from the coast (with one third of the incident Kelvin wave speed, at the equator), with a deeper thermocline at their centre. The role of the reflected Rossby waves is to broaden the resulting disturbance in the offshore direction. Equatorward of the critical latitude (given by Table 4.1), Rossby waves continually emanate westward from the coast, but the Rossby response becomes slower and smaller in scale with increasing latitude (see Section 2.3.3). The Rossby wave velocity, at the equator, can be estimated using Figures 4.3-e and 4.3-f, where the Rossby wave fronts are indicated by the dashed meridional line. According to the Figures 4.3-e and -f, the wave front has moved ~9° (from ~47° to ~56°) in 15 days. Resulting in a phase speed, in agreement with the theory, of ~0.8 m/s for the fastest Rossby mode.

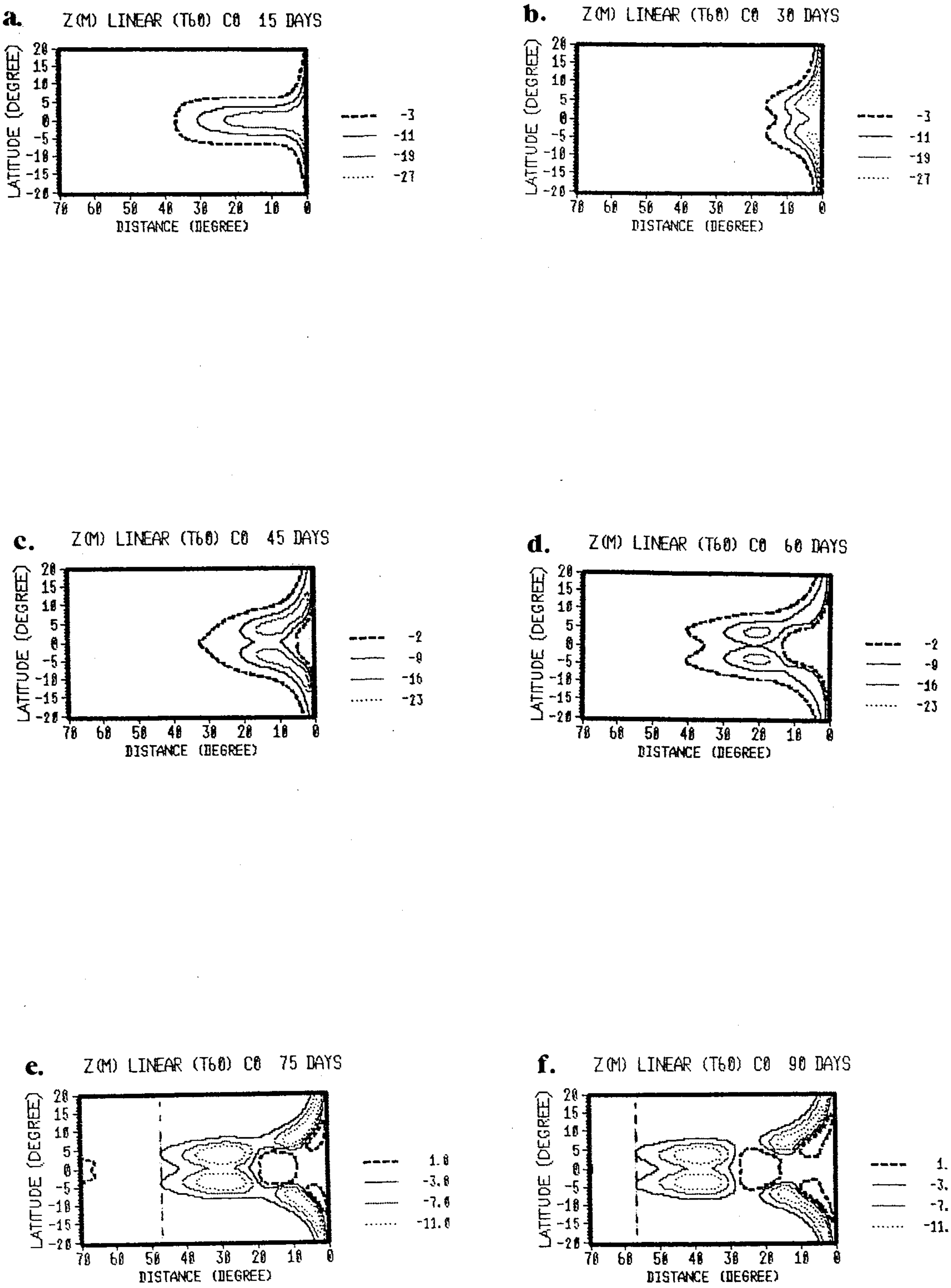

FIGURE 4.3: Sequential patterns of Z (in meters), at (a)15, (b)30, (c)45, (d)60, (e)75 and (f)90 days. Meridional boundary (γ=0°). Wave period: 60 days.

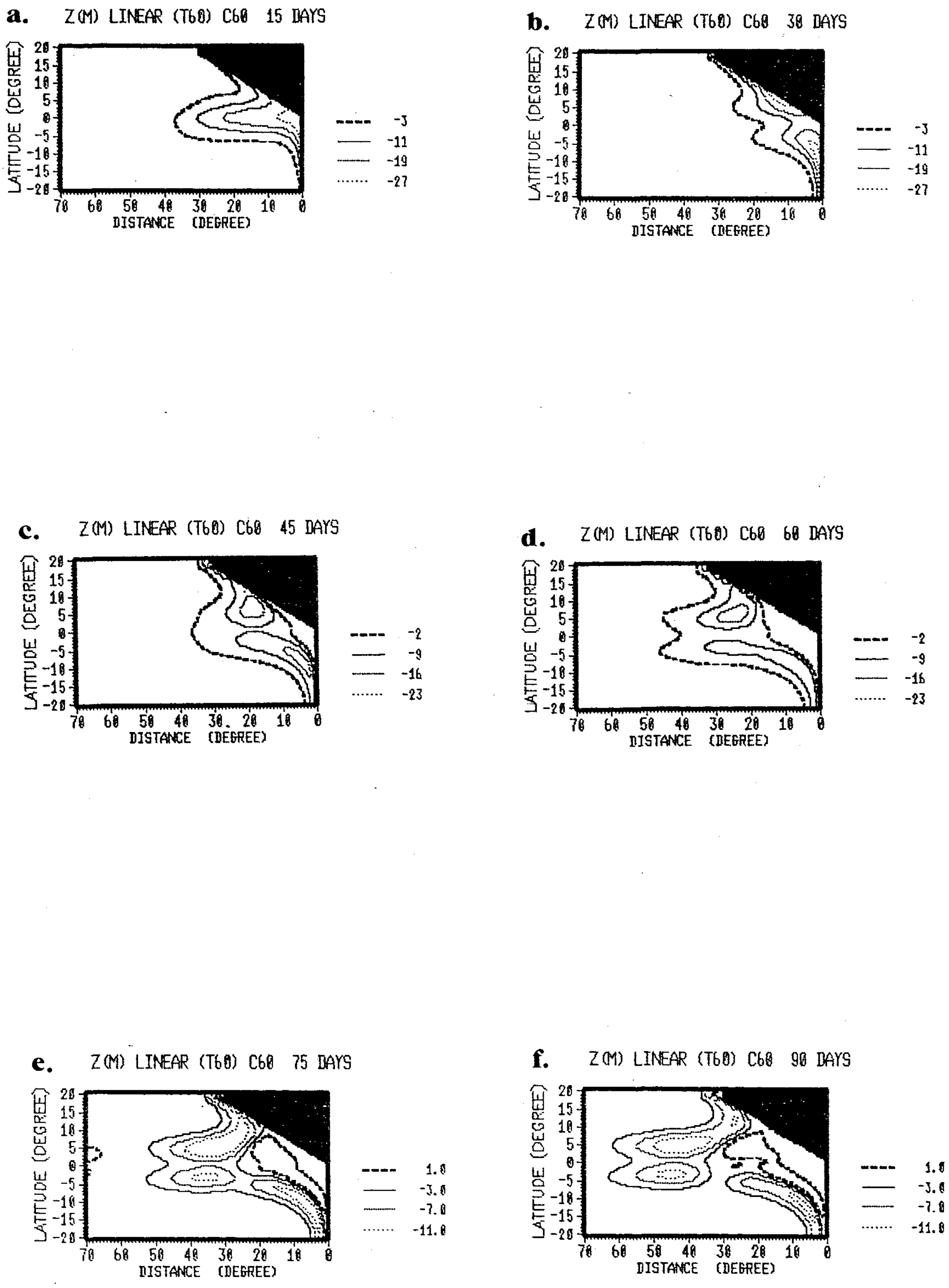

FIGURE 4.4: As Figure 4.3 except for γ=60°. Wave period: 60 days.

Figure 4.4 shows the latitude-longitude plot of the height field generated at a nonmeridional boundary ($\gamma=60°$) at the same six successive intervals of 15 days. The height field asymmetry between the Northern and Southern Hemisphere induced by the geometry of the eastern coast can clearly be seen in Figure 4.4.

The critical latitude values (θ_c) for $\gamma=0°$, $\gamma=40°$, $\gamma=50°$ and $\gamma=60°$, estimated using Equation (2.5.3), are shown in Table 4.1.

	θ_c(°)
$\gamma=0°$	9.0
$\gamma=40°$	7.0
$\gamma=50°$	5.8
$\gamma=60°$	4.5

TABLE 4.1: Critical latitude values (θ_c) for $\gamma=0°$, $\gamma=40°$, $\gamma=50°$ and $\gamma=60°$. Wave period (T): 60 days.

Table 4.1 shows that the more the boundary inclines from the meridian the lower is the associated θ_c value.

In this section only the Northern Hemisphere is considered for the calculation of the energy fluxes. The southward energy fluxes generated in all experiments and the northward energy flux generated at $\gamma=0°$ are symmetric in relation to the equator; i.e., $|t_S(0°,T)| = |t_S(40°,T)| = |t_S(50°,T)| = |t_S(60°,T)| = |t_N(0°,T)|$.

The numerical model is integrated for sufficient time

(90 days) to allow the coastal Kelvin wave, generated by the equatorial wave to leave the domain.

The linear poleward (t_N) coastal Kelvin wave energy flux and the dissipation of energy flux can be calculated, for different latitudes, using Equations (4.2.3) and (4.2.7), respectively.

The Equation (4.2.5) gives the linear net energy flux ($t=t_E-t_W$) towards the boundary. The direct determination of t_E-t_W, however, is computationally expensive because the propagation speed of the westward Rossby waves is a strong function of latitude, varying from ~0.8 m/s at the equator to zero at the poles. It could take years of the numerical integration for all the Rossby waves, generated at the eastern boundary, to reach the western side of the domain. To save computer time, first t_E is calculated and then t_W is inferred by energy conservation considerations.

The energy input in the experiment is solely from the baroclinic equatorial Kelvin wave (shown in Figure 4.2). Consequently before the reflection of this wave occurs at the eastern boundary, the eastward energy flux through a given longitude of the numerical domain corresponds to the value of t_E.

To avoid the equatorial Kelvin wave reaching the eastern boundary before the calculation of t_E, the longitudinal extent of the basin was increased from 70° to 140° with the initial field placed in the left hand side of the domain. This ensures that only the eastward energy flux is determined and not a combination of eastward and westward energy fluxes. In the experiment t_E was calculated 70° from the coast (position of the eastern boundary in the other runs). Figure 4.5 displays the result.

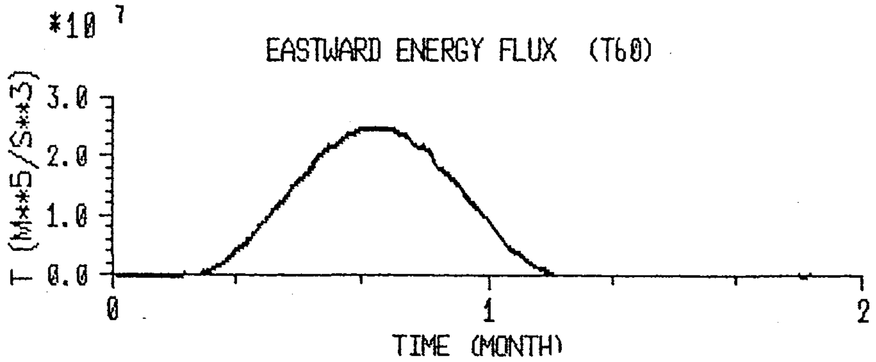

FIGURE 4.5: Eastward energy flux, t_E (4.6 10^9 m^5s^{-3}), as a function of time (month). Wave period: 60 days.

Given that t_E, t_N and t_D are known, the value of t_W, can be inferred by conservation of energy. It can be assumed that the reflected Rossby wave energy (t_W), for the Northern Hemisphere, is given by $t_E/2-t_N+t_D$.

Figure 4.6 shows the nondimensional linear energy flux coefficients (in %) generated at $\gamma=0°$, $\gamma=40°$, $\gamma=50°$ and $\gamma=60°$, respectively. The coefficients, $r_N(\gamma,T)$, $r_W(\gamma,T)$ and $r_D(\gamma,T)$ are, respectively, the ratios of the energy fluxes of the northward coastal Kelvin wave, of the reflected Rossby wave and of the dissipation to the total incoming equatorial Kelvin wave energy flux ($r_N= t_N/t_E$, $r_W= t_W/t_E$ and $r_D= t_D/t_E$). Observe that for each Hemisphere $|r_N|$ (or $|r_S|$) + $|r_W|$ + $|r_D|$ = 50%. The coefficients were numerically calculated at every 2° of latitude and integrated over 90 days. Note that r_N represents the northward energy flux crossing a given latitude and not the northward energy flux generated at that particular latitude (see Figure 4.0). Similarly, r_W and r_D represent, respectively, the reflected and the dissipated energy fluxes up to a given latitude and not the flux reflected or dissipated at that particular latitude.

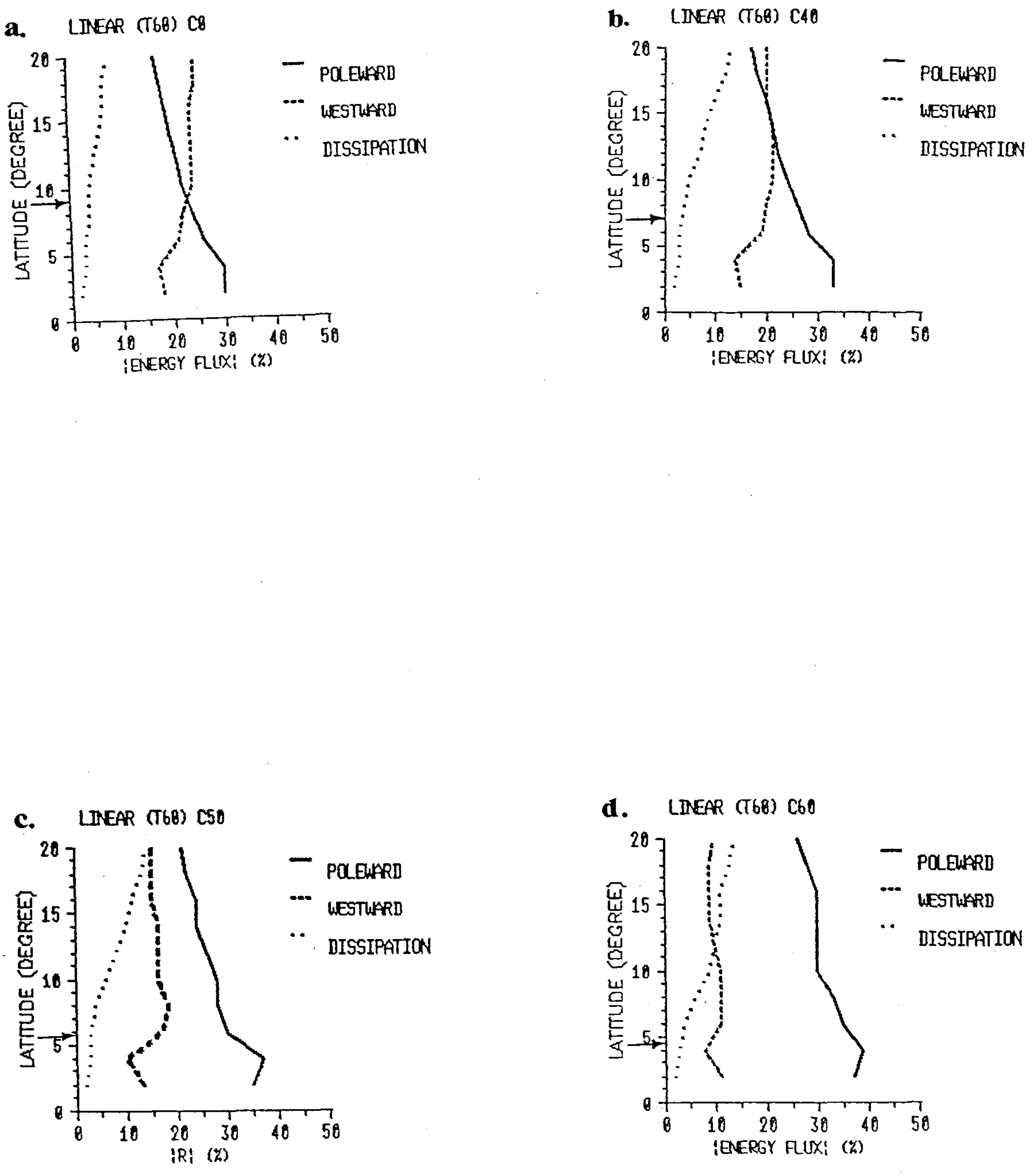

FIGURE 4.6: Linear energy flux coefficients (in %) at different latitudes (°). (a)$\gamma=0°$, (b)$\gamma=40°$ (c)$\gamma=50°$ and (d)$\gamma=60°$. Solid line: r_N. Dashed line: r_W. Dotted line: r_D. The arrows indicate the critical latitudes for the considered boundaries. Wave period: 60 days.

Analytical studies have shown that nonmeridional boundaries are less reflective than meridional ones. This occurs because nonmeridional boundaries favour trapped motion more than meridional ones (see discussion in Section 2.5).

According to Figure 4.6 above the critical latitude (shown in Table 4.1 and indicated in Figure 4.6 by an arrow) the westward energy fluxes do not change significantly with the latitude, but the poleward fluxes show an important latitudinal decrease. Theoretically above θ_c both energy fluxes, r_W and r_N, should be constant with the latitude (see Section 2.5).

The poleward energy flux decline, observed in Figure 4.6, can be explained by dissipative processes. The dissipation of energy increases with both the increase of latitude and with the proximity of the coast (lateral friction). In these experiments the θ_c values are relatively near the equator and therefore the coastal Kelvin waves are important in a large area of the domain. Hence most of the energy lost by dissipation in the domain is taken from the coastal Kelvin waves which results in a reduction of the poleward energy flux. The westward Rossby waves are less affected by dissipation.

In order to better understand the importance of the dissipation of energy in the domain, the former meridional boundary experiment (γ=0°) was repeated for the inviscid case (A_H=0, in the numerical model).

Figure 4.7 shows the numerical energy flux coefficients resulting from this experiment. The energy flux coefficients generated in the dissipative case are also plotted for comparison. Above the critical latitude in the inviscid case, the energy fluxes are, as expected, latitudinally constant.

The numerical values of r_N (solid line in Figure 4.7) and r_W (dashed line in Figure 4.7) are ~24% and ~26%, respectively.

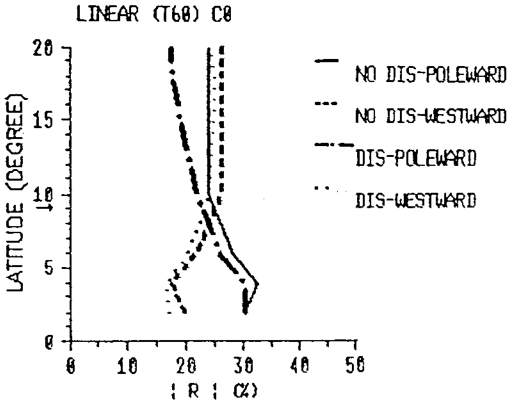

FIGURE 4.7: Linear energy flux coefficient (in %) at different latitudes (°). Solid and dashed lines: r_N and r_W, respectively, for the inviscid case. Centre-dashed and dotted lines: r_N and r_W, respectively, for the dissipative experiment. Meridional boundary. Wave period: 60 days.

The analytical values of r_N and r_W, in the Northern Hemisphere, can be obtained using Equations (2.5.4) and (2.5.6), respectively. For an equatorial Kelvin wave of 60 day period incident at a meridional boundary, the analytical values r_N and r_W are, respectively, ~24% and ~26%. Thus, the coefficient values generated by the inviscid numerical model are in excellent agreement with the analytical coefficient values.

The inviscid experiment was only carried out for the meridional boundary experiment because some dissipation is required in the numerical simulation of the nonmeridional boundaries. Spurious effects, probably due to the steplike form used for approximating the inclined eastern boundary, occur in the domain when the coefficient of dissipation is considered zero.

Table 4.2 displays the analytical values of r_W (obtained from Equation 2.5.6) for the different eastern boundary inclinations; the numerical reflection coefficient r_W is also shown in Table 4.2.

	r_W (model)	r_W (Equation 2.5.6)
$\gamma=0°$	24 (26)	26
$\gamma=40°$	20	18
$\gamma=50°$	15	11
$\gamma=60°$	10	0.5

TABLE 4.2: Linear westward energy flux coefficients (in % of the incident energy flux). The value in brackets is the coefficient obtained by the inviscid model. Wave period: 60 days.

As previously discussed, the difference between the analytical and numerical values of r_W for the meridional boundary experiment can be explained by dissipative effects; for the inviscid model these values are coincident. However, for all the inclined boundaries investigated here the numerical values of r_W are larger than the analytical ones. The deviation between the numerical and theoretical r_W values increases as the inclination of the coast increases (Table 4.2).

According to Hsieh et al.(1983), the wave behaviour in numerical models can be very different from that in the real ocean for the following reasons:(1)the use of unrealistically large viscosity coefficients; (2) poor spatial resolution; and (3) boundary conditions. The boundary conditions used in the open and closed boundaries of the numerical model have been shown, in Chapter 3, to be appropriate for the studied phenomena. To clarify the influence of (1) and (2) on the discrepancy observed between the analytical and the theoretical r_W values, a higher spatial resolution model ($\Delta S=1/8°$ in both directions) with a smaller coefficient of dissipation ($A_H=500\ m^2s^{-1}$) is utilized for an experiment similar to Experiment C60. Henceforth this experiment with the higher spatial resolution is referred to as Experiment C60-H.

Figure 4.8 shows the westward energy flux produced by Experiment C60-H. For comparison, the r_W coefficients previously generated by Experiment C60 are also plotted in Figure 4.8.

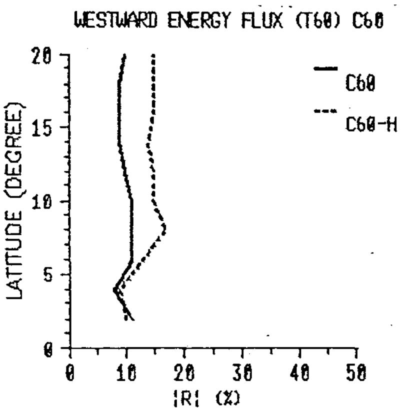

FIGURE 4.8: Linear westward energy flux coefficient (%) at different latitudes (°). Solid line for C60 and dashed line for C60-H. Wave period: 60 days.

Figure 4.8 shows that the C60-H experiment produces r_W values even larger than those generated by the C60 experiment. It indicates, therefore, that the large difference between the numerical and analytical westward energy fluxes of the nonmeridional boundary experiments (Table 4.2) are not due to the use of an unrealistically large viscosity coefficient or to the poor spatial resolution of the numerical model. Note that Experiment C60-H is in a better "resolution regime" than Experiment C60 (see Table 4.7) implying that the wave behaviour in the numerical model is expected to be very similar to that in the continuous viscous model.

Visual inspection of the anomaly height fields generated for Experiments C0 (Figures 4.3, 4.13 and 4.17) and C60 (Figures 4.4, 4.14 and 4.18) suggests that the dramatic change in coastal reflectivity induced by the inclination of the coastline, as presupposed by the analytical values of r_W (Table 4.2), has not been verified in this work. The presence of the westward Rossby waves generated at $\gamma=60°$ can be easily identified in Figures 4.4, 4.14 and 4.18.

γ (°)	$P = \omega\|\tan\gamma\|/f$
0	0.05
40	0.06
50	0.10
60	0.18

TABLE 4.3: Values of P for the different γ considered in the numerical experiments. The Coriolis parameter, f, was calculated at the respective θ_c (as given in Table 4.1). The intraseasonal frequency is ω=1.2 10^{-6} s^{-1}.

Equation (2.5.6) was obtained by Clarke (1992) assuming that $P = \omega|\tan\gamma|/f << 1$. Table 4.3 displays the P values for the frequency and the inclination of the coastlines utilized in the experiments. The Coriolis parameter (f) was calculated at $\theta=\theta_c$ (see Table 4.1 for the θ_c values). According to Table 4.3, as γ increases the value of P also increases and the validity of the analytical expression, Equation (2.5.6), becomes dubious.

The comparatively larger values of P obtained for the C50 and C60 experiments (Table 4.3) could invalidate the use of the analytical Equation (2.5.6) and be partially responsible for the large discrepancies observed between the analytical and the theoretical values of the reflected energy fluxes.

To compare the energy flux changes induced by the coastline inclination the coefficients, r_W, r_N and r_D generated at Experiment C0, C40, C50 and C60, are presented together in Figure 4.9.

According to Figure 4.9-a, for latitudes higher than θ_c the values of r_W are approximately constant with the latitude in all the experiments (see Table 4.2 for the r_W values). In qualitative agreement with the theory, the westward energy flux is smaller as the boundary tilts from the north-south direction. This result is consistent with the values of θ_c given in Table 4.1.

The poleward energy flux generated at $\gamma=0°$ is slightly smaller than that created at $\gamma=40°$, as can be seen in Figure 4.9-b, and significantly smaller than the poleward energy flux generated at both $\gamma=50°$ and $\gamma=60°$. The resemblance between the poleward energy fluxes for Experiments C0 and C40 can be understood by looking at Figure 4.9-c. This shows that the dissipation of energy increases when the coastline departs from the meridional direction. The increase in dissipation, however, is not a linear function of the coastline inclination. For example, the values of r_D at C40, C50 and C60 are comparable for the higher latitudes of the domain.

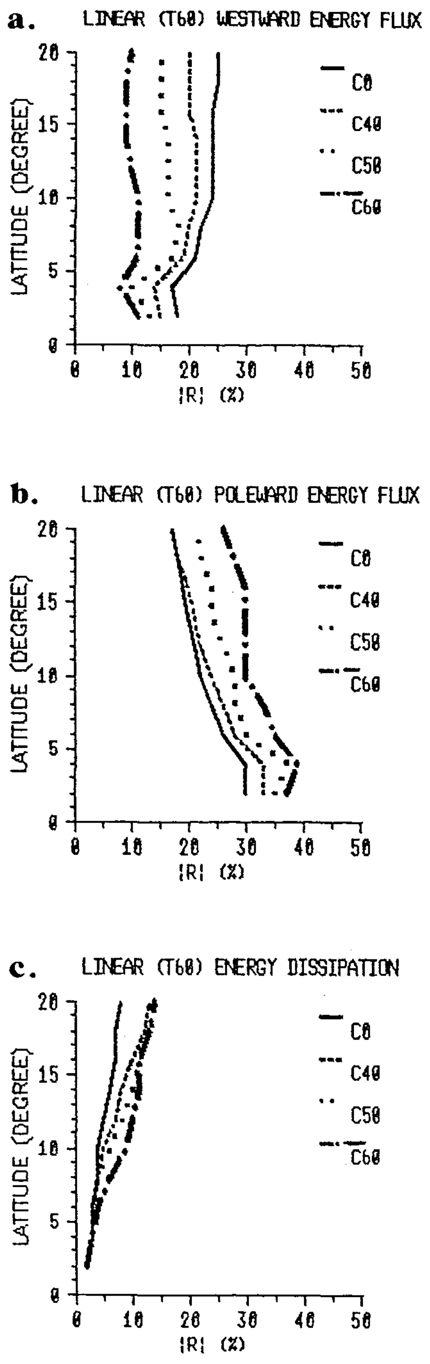

FIGURE 4.9: Linear energy flux coefficient (%) at different latitudes (°). (a)r_W, (b)r_N and (c)r_D. Solid line for γ=0°. Dashed line for γ=40°. Dotted line for γ=50°. Centre-dashed line for γ=60°. Wave period: 60 days.

At γ=40°, the increase in r_N induced by the coastline inclination appears to be counterbalanced by the increase of lateral viscosity, resulting in r_N values similar for Experiment C0 and C40.

Figure 4.9 indicates that despite r_D being larger at both γ=50° and γ=60° than at γ=0°, the dissipation of energy in the nonmeridional experiments (C50 and C60) is not large enough to compensate for the increase of energy induced by the coastline geometry. Therefore, the poleward energy fluxes generated at γ=50° and at γ=60° are significantly larger than that created at γ=0°.

The values of r_D obtained for the nonmeridional boundary experiments are larger for two main reasons. Firstly, the critical latitude for the slanted boundary is lower than that for the meridional one (see Table 4.1). As a result, when the boundary is inclined from the north-south direction comparatively less Rossby waves and comparatively more coastal Kelvin waves are present in the domain. Given that the dissipative effects are larger near the coast than in the interior domain, these Kelvin waves, trapped at the coast, are more affected by the dissipation than the Rossby waves. Secondly, the steplike form used for approximating the tilted eastern boundary generates some numerical noise.

In summary, when an equatorial Kelvin wave of intraseasonal period reaches any eastern ocean boundary, the amount of energy transferred to poleward coastal Kelvin waves will be strongly dependent on the amount of dissipation considered in the problem. The generation of reflected Rossby waves is significantly less dependent on the dissipation utilized.

4.3.2 Nonlinear case

In order to understand the possible effects of the non linearities in the low frequency wave reflection at eastern boundaries, some of the experiments performed in the previous section are repeated using the non linear model described in Chapter 3.

The low frequency motions investigated here are not expected to be profoundly altered by the inclusion of the nonlinearities. The 60-day Rossby waves, for example, are unlikely to form solitary waves (Rossby Solitons) because the dispersion is too small to balance nonlinearity to make a wave of permanent form possible (Boyd, 1980).

Figures 4.10 and 4.11 show the latitude-longitude plot of the non linear height field generated, respectively, at the meridional boundary (Experiment C0) and at the nonmeridional boundary (Experiment C60) at day 75 and 90.

The Rossby wave velocity, at the equator, can be estimated by the Rossby wave front displacement observed in Figures 4.10-a and -b (the wave fronts are indicated in these Figures). The Rossby wave front migrates from ~46° to ~53° in 15 days, resulting in a velocity of ~0.6 m/s. In the linear case the velocity is ~0.8 m/s. This result is theoretically expected. The non linear continuity equation gives a phase speed for the Kelvin wave $c=[g^*(H_0 + Z)]^{1/2}$ compared with $[g^*H_0]^{1/2}$ for the linear case. The linear Rossby wave velocity, at the equator, is approximately one third of the Kelvin wave velocity. In an upwelling region, as shown in the Figures 4.10 and 4.11, the height field is negative. Therefore, in an upwelling region the phase speed for the nonlinear case is less than the phase speed for the linear case.

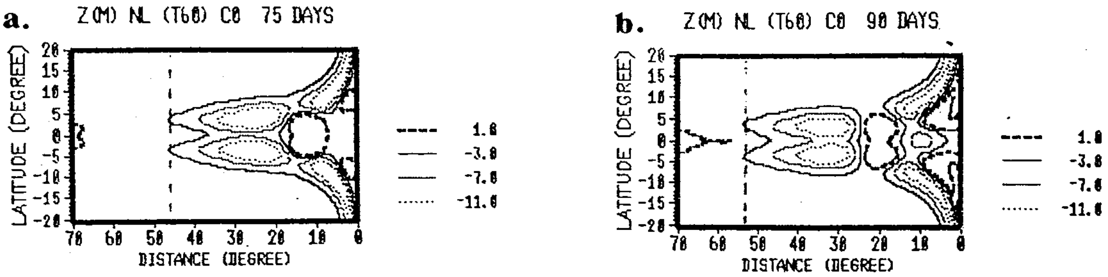

FIGURE 4.10: Non linear height anomaly (in meters), at (a)75 and (b)90 days. Meridional boundary ($\gamma=0°$). Wave period: 60 days.

FIGURE 4.11: As Figure 4.10 but for the nonmeridional boundary ($\gamma=60°$). Wave period: 60 days.

The non linear poleward coastal Kelvin wave energy flux (t_N), eastward energy flux (t_E) and the dissipation of energy (t_D) were estimated, respectively, from Equations (4.2.4), (4.2.6) and (4.2.8) for Experiments C0 and the C60.

The same equatorial Kelvin wave shown in Figure 4.2 was used as the initial condition for the non linear experiment. The eastward energy fluxes for the linear and non linear experiments were found to be similar (t_E= 4.6 10^9 m^5s^{-3}).

In the non linear case, the value of t_W is again assumed to be given by $t_E/2-t_N+t_D$, in the Northern Hemisphere.

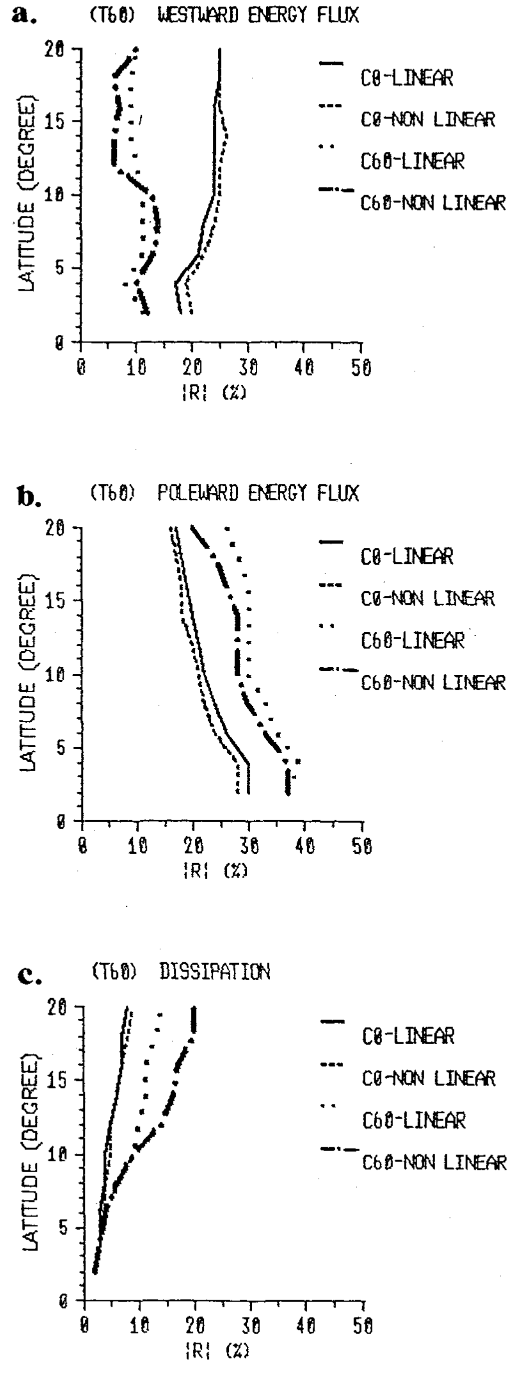

FIGURE 4.12: Energy flux coefficients (%) at different latitudes(°). (a)r_W, (b)r_N and (c)r_D. Solid and dashed lines for the non linear experiment at, respectively, $\gamma=0°$ and $\gamma=60$. Dotted and centre-dashed lines for the linear experiment at, respectively, $\gamma=0°$ and $\gamma=60°$. Wave period: 60 days.

Figure 4.12 shows both coefficients, linear and non linear, plotted together at different latitudes. In accordance with the linear experiment, the non linear northward and westward energy fluxes generated at γ=60° are, respectively, larger and smaller than those generated at γ=0° and the energy dissipated in Experiment C60 is larger than in Experiment C0.

The main differences between the non linear and linear experiments can also be seen in Figure 4.12. For the meridional boundary experiment the non linear and the linear energy flux coefficients can be roughly considered similar. For Experiment C60, the non linear westward energy flux presents a larger latitudinal variation when compared with the linear case (see Figure 4.12-a).

The principal contrast between the linear and non linear experiments (for γ=60°) occurs in the r_D coefficient (Figure 4.12-c). Above 10° of latitude, the dissipation of energy is considerably larger in the non linear case. Consequently, the non linear poleward energy flux is smaller when compared to the linear one (Figure 4.12-b). In contrast to the linear case, the non linear dissipation of energy affects not only the coastal waves but also the reflected westward Rossby waves, as can be seen in Figure 4.12-a.

The differences between the linear and the non linear results, however, are not very significant for the studied problem.

4.4 Seasonal variability

In this section some experiments similar to those of Section 4.3.1 are described here using as an initial condition for the numerical model an equatorial Kelvin wave of seasonal period: 180 days. Again a half equatorial Kelvin wavelength was used. Only the $\gamma=0°$ and $\gamma=60°$ cases are now considered (see Figure 4.1 for the geometry). The modelled region has latitudinal extent of 90° (from 45°S to 45°N) and maximum longitudinal extent of 175°.

The differences obtained between the linear and non linear experiments, shown in the previous section, do not justify the large amount of computing time necessary to run the non linear model. Therefore, hereafter only the linear model is utilized.

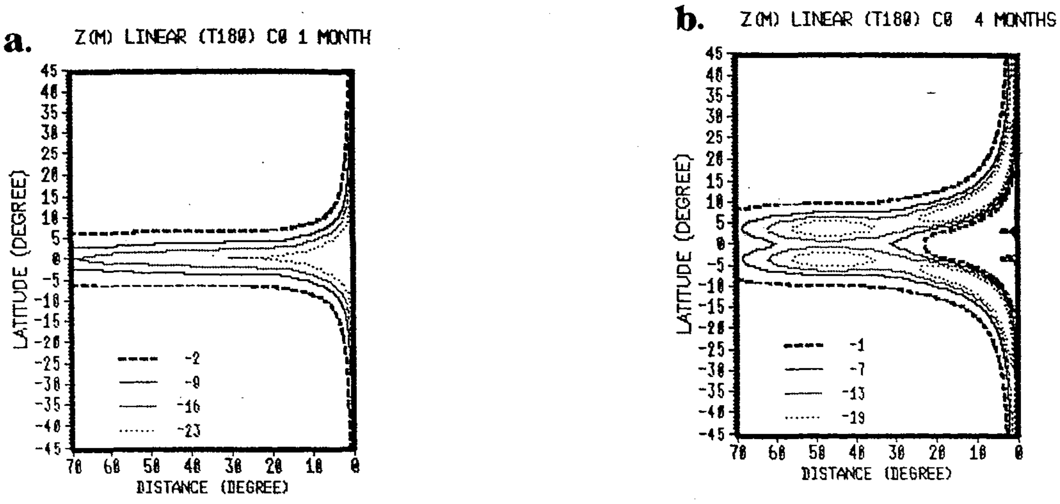

FIGURE 4.13: Z (m) at (a)1 and (b)4 months. Meridional boundary. Wave period: 180 days.

Figures 4.13 and 4.14 show the latitude-longitude plot of the height field anomaly generated, respectively, at meridional and nonmeridional boundaries, after 1 and 4 months of numerical integration. The eastern (70°) of the domain is shown in Figures 4.13 and 4.14.

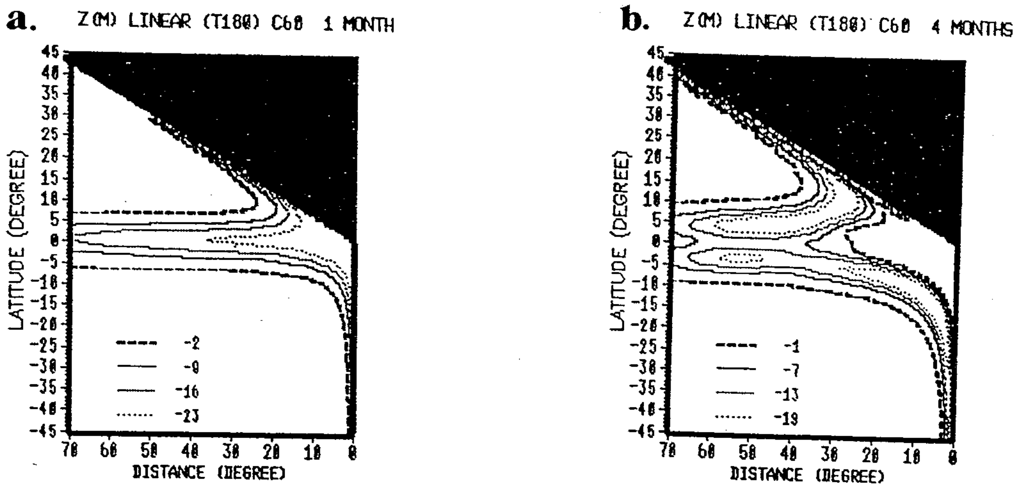

FIGURE 4.14: As Figure 4.13, but for γ=60°.

In order to calculate the energy fluxes, the numerical model was integrated for 6 months. That is the necessary time for the coastal Kelvin waves to leave the domain.

The critical latitude values (θ_c) for $\gamma=0°$ and $\gamma=60°$, are given in Table 4.4.

The linear northward (t_N) coastal Kelvin wave energy flux and the dissipation of energy flux can again be calculated using Equations (4.2.3) and (4.2.7), respectively.

	θ_c(°)
γ=0°	25.5
γ=60°	13.4

TABLE 4.4: Critical latitude values (θ_c) for the meridional (γ=0°) and nonmeridional (γ=60°) boundaries. Wave period (T): 180 days.

In a similar manner to the intraseasonal period experiment, the seasonal eastward energy flux, t_E, is estimated using a longitudinal extended basin (from 175° to 350°). The t_E value (= 1.4 10^{10} m^5s^{-3}) was calculated 175° from the eastern boundary.

Again, the value of t_W is obtained by conservation of energy considerations ($t_W = t_E/2-t_N+t_D$ in the Northern Hemisphere). The energy flux coefficients, r_W, r_N and r_D, generated at Experiments C0 and C60 are displayed in Figure 4.15.

For γ=0°, with the increase of latitude the poleward energy flux decreases and the dissipation of energy increases (see Figure 4.15-a). The westward energy flux increases with latitude until near the critical latitude (θ_c is indicated in Figure 4.15 by an arrow). As expected by the inviscid theory, r_W remains approximately constant with latitude (r_W~20%) above θ_c.

Figure 4.15-b shows that, analogous to Experiment C0, the poleward energy flux decreases and the dissipation of energy increases as the latitude increases. The values of r_N and r_D are coincident near 33° of latitude. Above the critical latitude the westward reflected Rossby wave energy is roughly constant with latitude (r_W~4%).

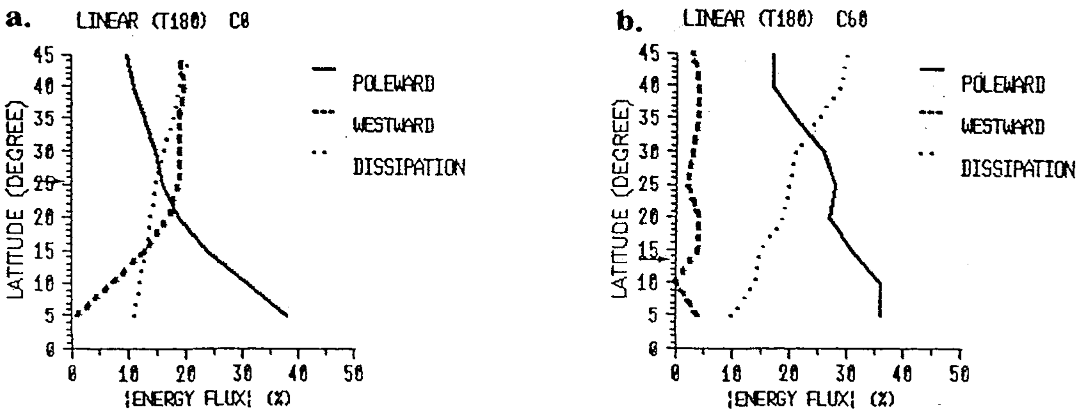

FIGURE 4.15: Linear energy flux coefficients (%) at different latitudes (°). (a)γ=0°and (b)γ=60°. Solid line: r_N. Dashed line: r_W. Dotted line: r_D. Wave period: 180 days.

In order to more easily compare the energy flux changes induced by the coastline geometry, the same coefficients presented separately for each coastline geometry (Figure 4.15) are displayed together in Figure 4.16.

The inclined boundary is less reflective than the meridional boundary (see Figure 4.16-a) and as a result the poleward energy flux generated at γ=60° is bigger than that generated at γ=0° (Figure 4.16-b). Figure 4.16-c shows that more energy is dissipated in the nonmeridional boundary than in the meridional one. These results are qualitatively similar to those generated by the intraseasonal period experiment.

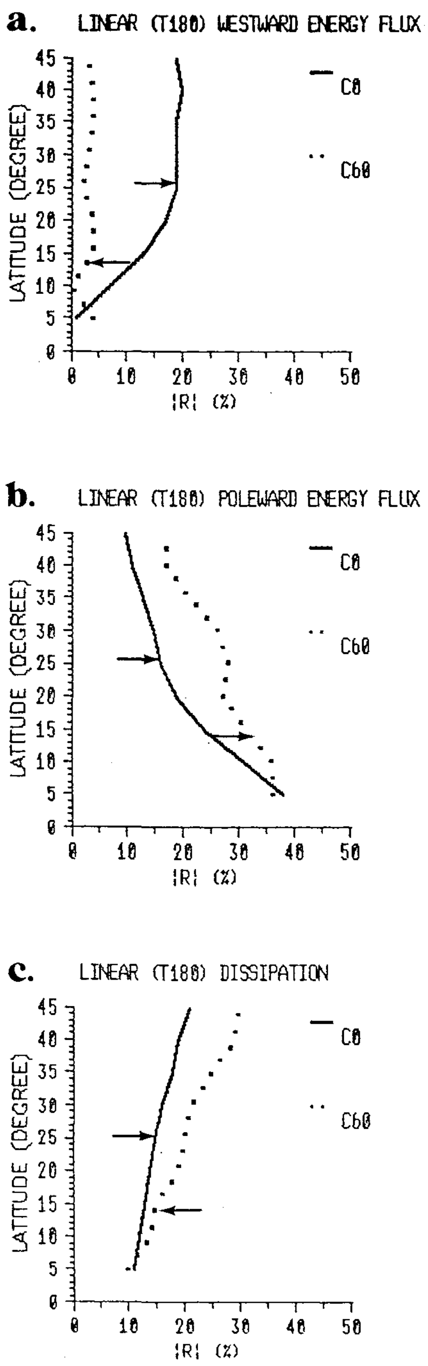

FIGURE 4.16: Linear energy flux coefficient (%) at different latitudes (°). (a)r_W, (b)r_N and (c)r_D. Solid line for γ=0°. Dotted line for γ=60°. Wave period: 180 days.

The analytical value of r_W can be obtained using again Equation (2.5.6). Table 4.5 displays the analytical (inviscid) and numerical (viscous) coefficients generated by an equatorial Kelvin wave, of 180 day period, incident at a meridional and a nonmeridional boundary.

	r_W (model)	r_W (Equation 2.5.6)
$\gamma=0°$	20	42
$\gamma=60°$	4	33

TABLE 4.5: Linear westward energy flux coefficients (in % of the incident energy flux) above the critical latitude. Wave period: 180 days.

Comparing the numerical and analytical solutions of r_W, shown in Table 4.5, it can be seen that there is a large discrepancy between the two values. The numerical results of r_W are now much smaller than the analytical ones. Two main factors contribute to the observed difference. The first and the most important is the inclusion of the viscosity in the numerical model. The energy dissipation increases considerably as the latitude increases (see Figure 4.16-c). Thus, for the long period studied here, the energy lost in the domain certainly restrains the propagation of Rossby waves, decreasing the values of r_W.

The second factor is that the analytical coefficient r_W was obtained by Clarke (1992) using the equatorial β-plane approximation whereas in the present study the numerical coefficient was obtained using spherical coordinates. The validity of the equatorial β-plane approximation to motions of a large latitudinal scale is questionable. Section 4.6

addresses this subject and suggests that at higher latitudes the equatorial β-plane dynamics permit an "anomalous" generation of Rossby waves.

For the inclined boundary experiment, a further point can contribute to the discrepancy that exists between the analytical and numerical solutions: that being the uncertainty of the validity of the analytical Equation (2.5.6) for the larger values of the coastline inclination (see Table 4.3).

4.5 Annual variability

Seeking the free wave solutions generated by the reflection of an equatorial Kelvin wave of annual period the experiments previously described were again performed. A half wavelength of an equatorial Kelvin wave of annual period (360 days) was used as an initial condition for the linear numerical model. The numerical domain utilized in the experiment has 350° of longitudinal extent and 90° (from 45°S to 45°N) of latitudinal extent.

Figures 4.17 and 4.18 show, respectively, the upper layer anomaly after 1 and 6 months of integration, for the meridional and nonmeridional coastlines. Again, only the eastern 70° of the domain is displayed.

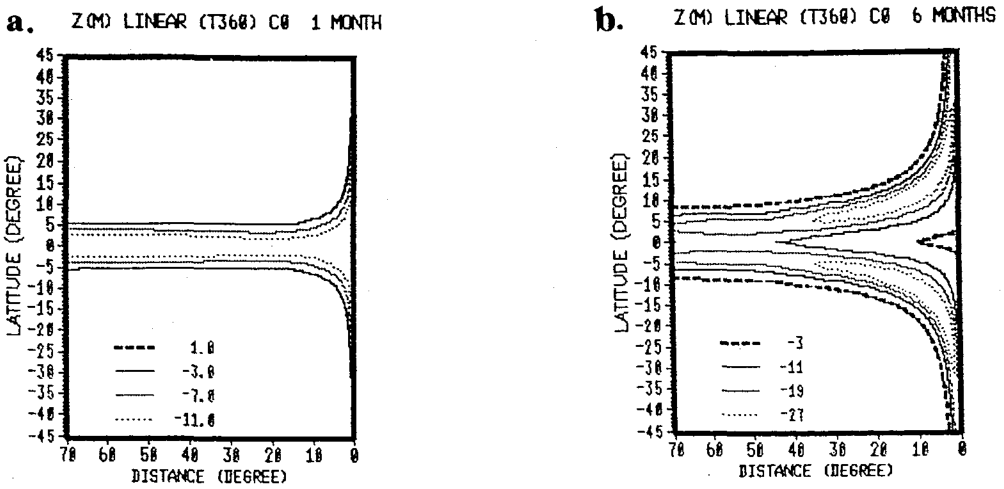

FIGURE 4.17: Z (m) at (a)1 and (b)6 months. Meridional boundary. Wave period: 360 days.

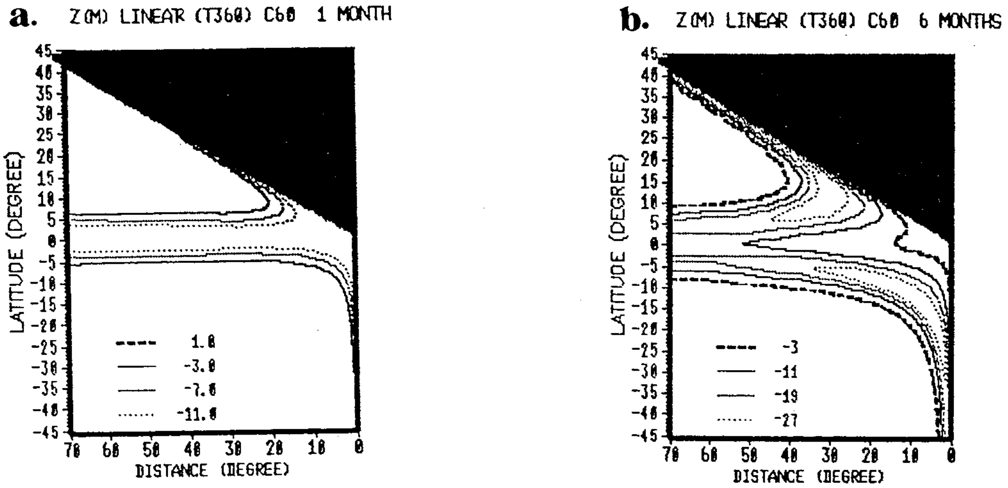

FIGURE 4.18: As Figure 4.17 but for the nonmeridional boundary.

Table 4.6 shows the critical latitude values for the meridional and sloping coastlines. Note that when γ=0° the critical latitude is very close to the northern latitude of the numerical model (45°). Consequently, for the domain considered, most of the energy of the incoming equatorial wave of annual period is expected to be reflected as westward Rossby waves.

Following the previous experiments the poleward energy flux and the dissipation of energy flux were calculated using Equations (4.2.3) and (4.2.7), respectively. The model was integrated for 8 months.

The eastward energy flux, t_E, was estimated using a longitudinally doubled domain (700°). Repeatedly, t_E is calculated at the middle of this larger domain, at 350° from the eastern boundary (t_E = 2.8 10^{10} m^5s^{-3}) and the westward energy flux is obtained using energy conservation considerations.

	θ_c(°)
γ=0°	43.6
γ=60°	25.5

TABLE 4.6: Critical latitude values (θ_c) for the meridional (γ=0°) and nonmeridional (γ=60°) boundaries. Wave period (T): 360 days.

The energy flux coefficients, for Experiments C0 and C60, are shown in Figure 4.19. For the two boundaries considered, as the latitude increases the r_D values increase and the r_N values decrease. This result is in qualitative concordance with the inviscid theory (Clarke, 1992).

Compared with the previous experiments, the westward energy fluxes, however, present an anomalous behaviour in both meridional and nonmeridional cases.

For the meridional boundary experiment the r_W coefficient increases latitudinally up to 30° of latitude (see Figure 4.19-a). Above 30° of latitude r_W becomes nearly constant with latitude. However, according to the theory the r_W coefficient is expected to be latitudinally constant only above the critical latitude (θ_c=43.6°). The analytical value, given by the Equation (4.2.6) is 46%.

Further, in the inclined boundary experiment, the r_W coefficient is not constant with latitude above θ_c. It increases up to 20° of latitude and decreases for latitudes higher than 20°. Note the r_W is expected to increase up to the critical latitude (θ_c=25.5°) and to be constant above that latitude (r_W~42% from the Equation 2.5.6) .

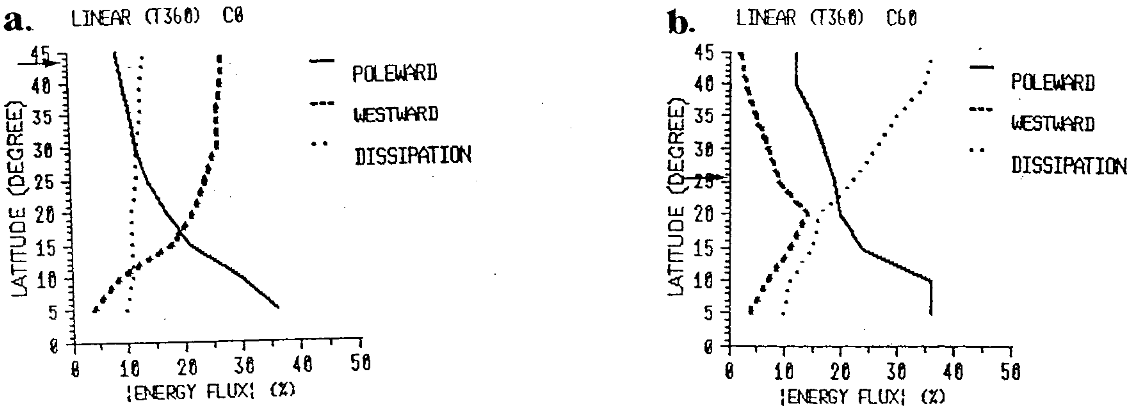

FIGURE 4.19: Linear energy flux coefficients (%) at different latitudes (°). (a)$\gamma=0°$ and (b)$\gamma=60°$. Solid line: r_N. Dashed line: r_W. Dotted line: r_D. Wave period: 360 days.

In summary, the numerical values of r_W for the annual period case, are smaller than the theoretical coefficients. In the meridional boundary experiment, below the critical latitude, the r_W values are constant with the latitude, whereas theoretically they should increase as the latitude increases. For the inclined boundary, above the critical latitude r_W decreases with the latitude and from the theory it is expected to be constant as the latitude increases.

Similarly to the seasonal period experiment, the energy flux lost by dissipation and the use of the equatorial β-plane approximation in the analytical Equation (2.5.6) could be responsible for the smaller values of r_W obtained numerically (Figure 4.19).

Note that the values of r_D obtained for Experiment C60 are much larger than the r_D coefficients generated at C0. For the annual experiment most of the energy of the incoming equatorial wave is expected to be reflected at the meridional boundary as westward Rossby waves and, as already discussed, these waves are less affected by dissipation than the coastal Kelvin waves. For Experiment C60, above 25.5° of latitude the incoming energy is trapped as coastal Kelvin waves. This could explain the large discrepancy between the r_D values created in the meridional and nonmeridional boundaries.

The similarity of r_N values obtained in both the experiments can be justified by the larger dissipative effect in the C60 experiment. The increase in r_N induced by the coastline inclination is compensated by the increase of viscosity, resulting in similar values for r_N in the two experiments.

4.6 Validity of the equatorial β-plane approximation

It is convenient to consider the potential vorticity equation in order to examine the validity of the equatorial β-plane approximation for the phenomenon studied.

4.6.1 Linear equatorial β-plane potential vorticity (βPV)

The equatorial β-plane potential vorticity (βPV) equation can be readily obtained from Equations (2.2.1). Assuming that the motion is geostrophic in the alongshore direction (y), the βPV can be written as:

$$\frac{\partial}{\partial t}\left(\frac{\partial v}{\partial x} - \frac{f}{H} h\right) + \beta v = 0 \qquad (4.6.1)$$

Furthermore, it is supposed that the alongshore particle velocity, v, at a meridional wall can be given by $\partial y/\partial t$. Thus:

$$\frac{\partial v}{\partial x} - \frac{f}{H} h + \beta \, \Delta y = 0 \qquad (4.6.2)$$

As discussed by Clarke (1992), coastal Kelvin wave dynamics apply when $\beta=0$ and the relative vorticity ($\partial v/\partial x$) balances the vortex stretching (- fh/H). As the latitude decreases, f decreases and vortex stretching (and relative vorticity) terms become comparable to the induced planetary vorticity change. When the induced planetary vorticity change (β Δy) is more than twice the relative vorticity, energy leaves the boundary as a Rossby wave (Clarke (1992)).

4.6.2 Linear spherical coordinate potential vorticity (PV)

The PV Equation can be obtained from Equations (3.2.8)-(3.2.10). Assuming, again, that the motion is geostrophic in the alongshore direction (θ) and that the alongshore particle velocity, v, at a meridional wall is given by $r\partial\theta/\partial t$, the PV equation can be written as:

$$\frac{1}{r\cos\theta}\frac{\partial v}{\partial\lambda} - \frac{f}{H}h + \Delta f = 0 \qquad (4.6.3)$$

For the physical mechanism of main interest here, the generation of Rossby waves, the most important term in Equations (4.6.2) and (4.6.3) is the induced planetary vorticity change, given by ($\beta\Delta y$) and by (Δf). The remainder of this section considers the distinction between these two terms.

Figure 4.20 shows the difference between the planetary vorticity changes as given by ($\beta\Delta y$) and (Δf), as a function of latitude. The curve was plotted considering a constant latitudinal interval of 1°. As can be seen in Figure 4.20, near 45° of latitude the planetary vorticity change generated using the equatorial β-plane approximation is about 30% larger than that generated using spherical coordinates.

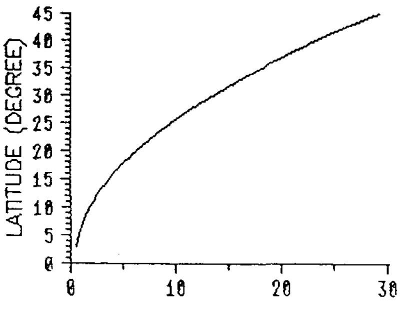

FIGURE 4.20: Difference between the planetary vorticity change in the equatorial β-plane and in the spherical coordinates (in %) as a function of the latitude.

The above discussion suggests that at higher latitudes the equatorial β-plane dynamics allow a spurious generation of Rossby waves.

The use of the equatorial β-plane approximation by Clarke (1992) in the resolution of the analytical problem could help to explain the discrepancy between the numerical and analytical results obtained in the experiments presented here. Actually the spherical coordinate system must be used, rather than the equatorial β-plane approximation, because the north-south scale of motion studied is large enough for variations in the value of β to be important.

4.7 Numerical considerations

4.7.1 Spatial resolution

In all the experiments described in Chapters 4 and 5, except Experiment C60-H, a regular 1/4 degree resolution is used in both zonal and meridional directions ($\Delta\lambda=\Delta\theta=1/4°$). The C60-H experiment utilized a regular 1/8 degree of resolution.

This grid spacing is less than the smallest baroclinic Rossby radius (R) of the modeled region. For the highest latitude of the numerical domain (45°), R~24 km and $\Delta\lambda$~17 km.

4.7.2 Temporal resolution

The time steps (Δt) used in all the experiments satisfy the CFL stability criterium given by (A.5.1). For the linear experiments a Δt of 4 hours was utilized. However, for the non linear model, the condition (A.5.1) was used only as a guide for choosing the time interval. The Δt actually employed in the non linear model, (Δt= 2 hours), was arrived at by a trial-and-error process.

4.7.3 Viscous effects

A Laplacian coefficient of 10^3 m^2s^{-1} is employed in most of the numerical experiments described in this study. Only the C60-H experiment uses a coefficient of 500 m^2s^{-1}.

The coefficient value, 10^3 m^2s^{-1}, has been commonly used in baroclinic shallow water numerical models. Numerically, the coefficient helps to smooth the numerical noise associated with very high wave numbers. Physically, A_H helps to form the viscous boundary layer required to fit the theory with the observations.

The effects of viscosity on linear free baroclinic Kelvin waves in numerical shallow-water models are discussed in the Appendix (Section A.6). Table 4.7 shows the parameter regime values (as defined by Davey et al.,1983 and Hsieh et al., 1983), calculated for the highest latitude of the numerical domain used in the experiments described in Chapters 4 and 5. For the intraseasonal experiment θ_{max}=20° and for the seasonal and annual experiments θ_{max}=45°.

	α (given by A.6.2)	ϵ (given by A.6.1)	Δ (given by A.6.3)	ϵ/Δ^2
T60; ΔS=1/8°; A_H=500 m^2s^{-1}	1.0 10^{-4}	0.17	0.27	2.33
T60; ΔS=1/4°; A_H=10^3 m^2s^{-1}	2.0 10^{-4}	0.34	0.53	1.21
T180; ΔS=1/4°; A_H=10^3 m^2s^{-1}	7.0 10^{-5}	4.5	0.8	6.6
T360; ΔS=1/4°; A_H=10^3 m^2s^{-1}	3.0 10^{-5}	9.0	0.8	13.2

TABLE 4.7: Non dimensional parameters associated with the viscosity and the finite-differencing scheme.

Table 4.7 shows that the Rossby radius is reasonably well resolved by the model grid (see Δ) and that the numerical model is in a "good resolution" regime (see ϵ/Δ^2). Therefore, the wave behaviour is expected to be similar to that in the continuous case.

Note that the offshore viscous effect (ϵ) increases considerably as both the wavelength and the latitude increase. The increase in ϵ causes a large increase in decay rate and a decrease in velocity as a wave travels poleward. The use of a free-slip boundary, however, prevents the reduction in velocity from being very severe (Davey et al., 1983). The alongshore coefficient (α) is very small in all the experiments.

4.8 Summary

The free waves solutions generated by low frequency wave reflection at meridional and nonmeridional eastern boundaries, are shown not to be significantly affected by nonlinearities. The viscous effects, however, are of major importance for the problem. If no viscosity is incorporated in the model (A_H=0) the agreement between the numerical simulations and the analytical results is very good.

The real ocean, however, is viscous. In this study, a viscosity coefficient of 10^3 m^2s^{-1} is utilized in the numerical model. This is a standard value, widely used in models similar to this one. Some authors have indicated that 10^3 m^2s^{-1} is a reasonable value to be used for this coefficient. Davey et al.(1983), for example, suggested a value of the order of 10^3-10^4 m^2s^{-1}. They have used the fact that the onshore velocity is nonzero when $A_H > 0$ to estimate the amount of viscosity required in their continuous wave model to achieve a realistic onshore flow; i.e, a flow comparable to the onshore flow observed in the free baroclinic coastally-trapped waves off Peru.

The difference between the analytical (inviscid) and the numerical energy fluxes, for γ smaller than 40°, are primarily due to the inclusion of dissipative effects in the numerical model and, to a lesser extent the utilization of the equatorial β-plane approximation in the previous analytical expressions. For coastline inclinations greater than 40°, the analytical energy flux expression, as given by Clarke (1992) may be doubtful.

Analytical works which exclude dissipative effects and make use of the equatorial β-plane approximation (Schopf and al.,1981; Grimshaw and Allen, 1988; Clarke and Shi, 1991 and Clarke ,1983,1992; among others) have shown that:

(1) nonmeridional boundaries are less reflective than meridional ones;
(2) the poleward coastal Kelvin wave energy flux is greater the more the boundary inclines from the meridian; and
(3) the westward energy flux increases and the poleward energy flux decreases as the incident Kelvin wave period is increased.

Analysing the Figures 4.13-a, 4.16-a and 4.19, it can be seen that for any period, T, studied, statement (1) is always true: the nonmeridional boundary is less reflective than the meridional one [$r_w(0°,T) > r_w(60°,T)$].

Statement (2) is true for all the experiments except for the intraseasonal period with γ=40°. The increase in poleward flux, for γ=40° and intraseasonal period wave, is counterbalanced by the large increase of lateral viscosity (see Figure 4.9).

To verify statement (3), the energy flux coefficients have been plotted together for different wave periods. Figure 4.21 shows those coefficients generated at the meridional boundary. To relate experiments of different periods it is necessary to examine the coefficient values above their particular critical latitude. The critical latitude for each period studied are indicated in Figure 4.21 with arrows.

Figure 4.21 shows that, for the experiments investigated here, statement (3) is not always verified. This is due to the inclusion of the energy dissipation in the model. For the studied problem, the dissipation of energy depends on the kind of waves present in the domain, being larger for the coastal Kelvin waves than for the Rossby waves. Hence, the higher the critical latitude, the less Kelvin waves are present in the domain and the lower is the energy dissipated (see Section 2.5). For the coastal Kelvin waves present in the domain the dissipation of energy, however, increases as the period of the wave increases (see the values of ϵ given in Table 4.7). Davey et al.(1983) have analytically shown this result using a continuous viscous model. The final amount of energy taken from the domain by dissipation, therefore, depends not only on the presence of the coastal Kelvin waves (for longer period wave, less coastal waves and less dissipation) but also on the frequency of these waves (for longer period waves, more dissipation).

In the annual experiment, for example, because of its higher critical latitude value (Table 4.5, for $\gamma=0°$) there are mainly Rossby waves in the studied domain. As a result, the r_D values for the annual experiment are smaller than those for the seasonal case (Figure 4.21-c). In the intraseasonal period, however, despite its comparatively lower critical latitude (Table 4.1 for $\gamma=0°$) the r_D values are the smallest amongst those obtained in the experiments. This occurs due to the comparatively smaller value of ϵ (Table 4.6) obtained in the intraseasonal case. The intraseasonal westward energy flux is practically unaffected by dissipation (see Figure 4.7), which results in comparatively larger values of r_W (Figure 4.21-a).

In summary, the veracity of statements (2) and (3) depends strongly on the viscosity included in the problem.

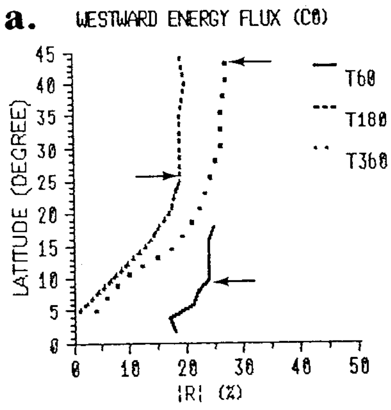

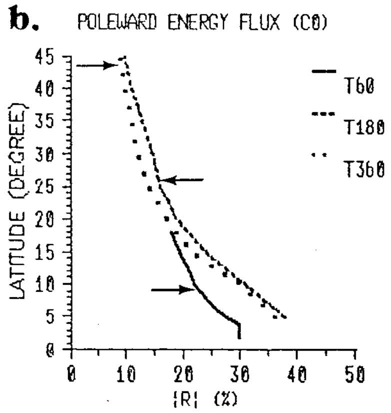

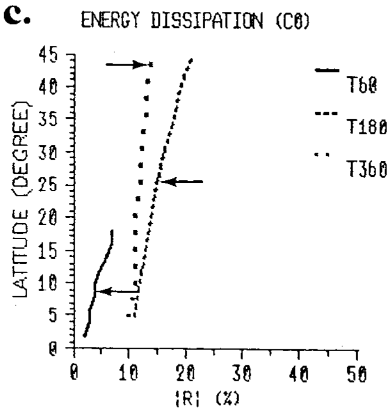

FIGURE 4.21: Linear energy flux coefficient (%) at different latitudes, for different incident wave periods. (a)r_W, (b)r_P and (c)r_D. The arrows indicate the critical latitude for the investigated period wave. Meridional boundary.

CHAPTER 5 - RESULTS

PACIFIC AND ATLANTIC EASTERN BOUNDARIES

5.1 Introduction

The experiments described in the Chapter 4 are now applied to more realistic ocean boundaries representing the Pacific and Atlantic eastern coastlines.

Both the Pacific and Atlantic experiments are performed using the numerical model, described in Chapter 3, with one layer of initial thickness 200 m. The linear phase speed is assumed to be 2.45 m/s and the viscosity coefficient 10^3 m^2s^{-1}.

In the model the eastern Pacific and Atlantic coastlines are defined by the position of the 200 m isobath instead of the actual coastline, as it is a better approximation of the vertical coast assumed in theory (the initial layer thickness is considered to be 200 m).

The free waves solutions generated by the reflection of baroclinic equatorial Kelvin waves of different periods (intraseasonal, seasonal and annual) at the Pacific eastern coast is examined in Section 5.2. The variability in the eastern Atlantic is investigated in Section 5.3.

5.2 Pacific Ocean

5.2.1 Intraseasonal variability

The linear and non linear experiments described in this section employ a numerical model basin of latitudinal extent of 40° (from -20° to 20°) and maximum longitudinal extent of 70°. The eastern Pacific boundary approximation used in the intraseasonal experiments is shown in Figure 5.1. The geometry ignores the Gulf of California. Nevertheless, Clarke (1992) has shown that the energy flux entering the Gulf is the same as that leaving it.

A baroclinic equatorial Kelvin wave of 60-day period, similar to that displayed in Figure 4.2 is used as an initial condition for the numerical model for the intraseasonal linear and non linear cases. The numerical model was integrated for 90 days. The eastward energy flux (input energy) is the same as that in Figure 4.3 of Section 4.3.1 ($t_E = 4.6\ 10^9\ m^5 s^{-3}$).

5.2.1.1 Linear case

The longitude-latitude plot of the linear upper layer anomaly at six successive intervals of 15 days is given in Figure 5.1. The coastally trapped Kelvin waves are visible as a deepened thermocline along the coast, and the Rossby wave as a closed contour, moving westward from the coast. Compare the Pacific intraseasonal fields, with those generated in Experiments C0 (Figure 4.3) and C60 (Figure 4.4).

The linear northward energy flux (t_N) and the dissipation of energy (t_D) were numerically calculated using Equations (4.2.3) and (4.2.7) respectively; the southward energy flux (t_S) was obtained using Equation (4.2.3) with the signal changed: $\theta=+\theta_0$ for $\theta=-\theta_0$.

The energy input (t_E) in the experiment, as in the previous chapter, is only due to the baroclinic equatorial Kelvin wave. The westward energy flux (t_W), was again inferred by conservation of energy. It is assumed that the reflected Rossby wave energy (t_W) is given by $t_E/2-t_N+t_D$ for the Northern Hemisphere and by $t_E/2-t_S+t_D$ for the Southern Hemisphere.

Figure 5.2 shows the nondimensional linear energy flux coefficients, $r_P(\gamma,T)$, $r_W(\gamma,T)$ and $r_D(\gamma,T)$, as defined in Section 4.3.1, generated at the eastern Pacific coast. The coefficients were calculated at latitudinal intervals of 2° and integrated in time for 90 days.

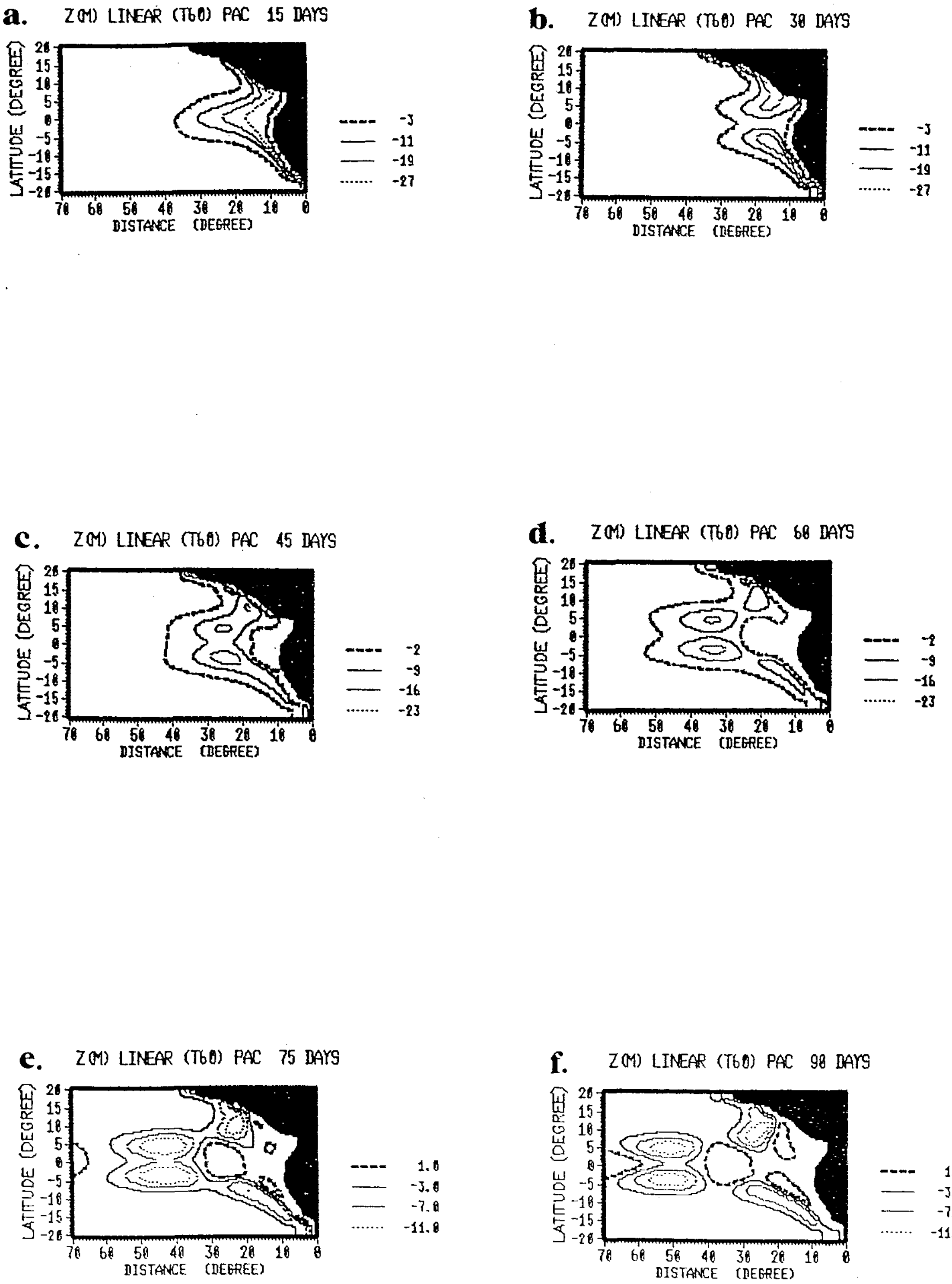

Figure 5.1: Sequential patterns of Z (in metre), at (a)15, (b)30, (c)45, (d)60, (e)75 and (f)90 days. Wave period: 60 days. Pacific coastline.

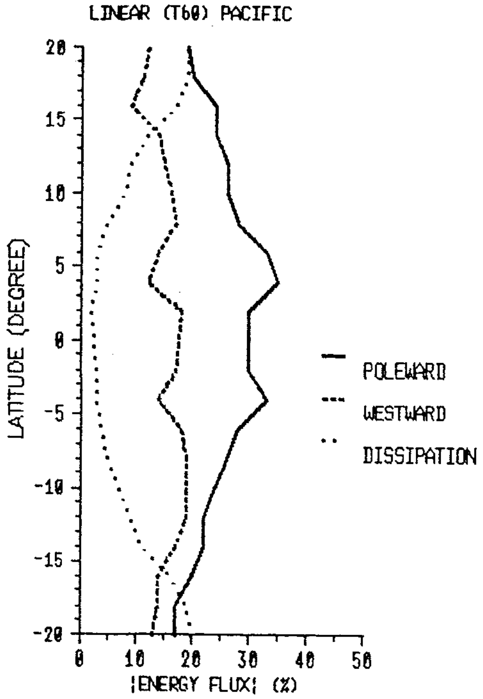

FIGURE 5.2: Linear energy flux coefficients (%) at different latitudes (°). Solid line: r_P. Dashed line: r_W. Dotted line: r_D. Wave period: 60 days. Pacific Ocean.

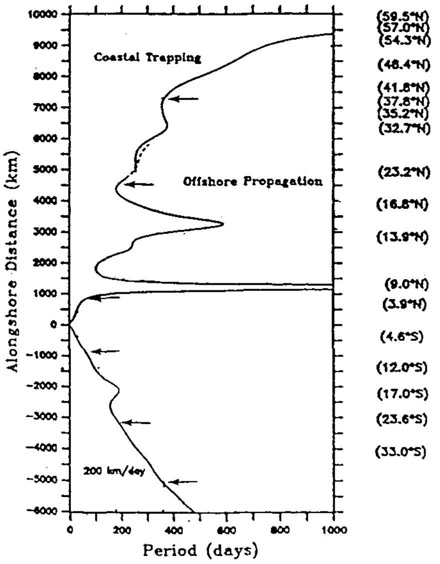

FIGURE 5.3: The critical latitude for the eastern Pacific ocean as a function of distance from the equator. For periods and alongshore distances corresponding to points on the right of the curves, the waves propagate offshore, whereas for points to the left of the curves, the waves are coastally-trapped, as evidenced. [Adapted from Grimshaw and Allen, 1988]. The arrows indicate the approximate northernmost value of θ_c for the periods investigated here.

According to Figure 5.2, the northward energy flux is somewhat larger than the southward energy flux whereas the westward energy flux is smaller in the Northern Hemisphere than in the Southern Hemisphere. This is consistent with the Northern Pacific boundary being more inclined to the meridian. The energy dissipation is roughly similar in both Hemispheres. The westward energy flux, in disagreement with the results of Section 4.3, presents a considerable latitudinal variation. It is due to the changing coastline angle of inclination, γ, which allows more than one critical latitude for the eastern Pacific coastline (Grimshaw and Allen, 1988; Clarke and Shi, 1991 and Clarke, 1992).

Figure 5.3, from Grimshaw and Allen (1988), shows the critical latitude values calculated along a smoothed eastern Pacific boundary as a function of distance from the equator, considered positive to the north. The critical latitude was obtained using the coastal internal Kelvin wave speed of 200 km/day (~2.3 m/s). Note that for a range of oscillation periods the variations of γ for the Northern Hemisphere coastal geometry results in more than one critical latitude. This also occurs, but to a lesser extent, in the Southern Hemisphere. For periods and alongshore distances corresponding to points on the right of the curves, the waves propagate offshore, whereas for points to the left of the curves, the waves are coastally-trapped. The oscillation periods investigated in this chapter together with their approximate value of the northernmost θ_c are also indicated in Figure 5.3.

5.2.1.2 Non linear case

To appreciate the effects of nonlinearity on low frequency wave reflection at the Pacific boundary, the non linear model was run using the same parameter and the same initial condition (equatorial Kelvin wave; Figure 4.2) as used for the linear experiment.

The non linear poleward coastal Kelvin wave energy flux (t_P) and the dissipation of energy (t_D) are estimated, for both Hemispheres, using Equations (4.2.4) and (4.2.8). The values of t_W are again derived from energy conservation considerations.

To compare the relative importance between the change in energy flux caused by the nonlinearities and by the coastline geometry, Figure 5.4-a shows the westward energy fluxes calculated using the (1) Pacific coastline and the linear model (solid line); (2) meridional coastline and the linear model (dashed line); (3) Pacific coastline and the non linear model (dotted line) and (4) meridional boundary and the non linear model (centre-dashed line). Figures 5.4-b and 5.4-c, show, respectively, the poleward and the energy dissipation coefficients for the four cases.

According to Figure 5.4, the changes in energy fluxes and in energy dissipation induced by the coastline geometry are notably more important than those induced by the nonlinearities.

The Pacific coastline is less reflective than the meridional boundary (see Figure 5.4-a). This is expected because nonmeridional boundaries favour trapped motion more than meridional ones (see Section 2.5.1).

For the cases presented in Figure 5.4, the poleward energy fluxes are similar; the smallest values are given by case (4) and the largest by case (1) (Figure 5.4-b). Because the Pacific coastline is a nonmeridional boundary, the Pacific r_P values (particularly r_N) would be expected to be significantly larger than the r_P values generated in Experiment C0. However, as discussed in Chapter 4, the dissipation induced by the nonmeridional boundary is larger than that induced by the meridional one (see Figure 5.4-c). Hence, for the Pacific coastline the increase in dissipation prevents the rise in poleward energy flux induced by the geometry of the coast.

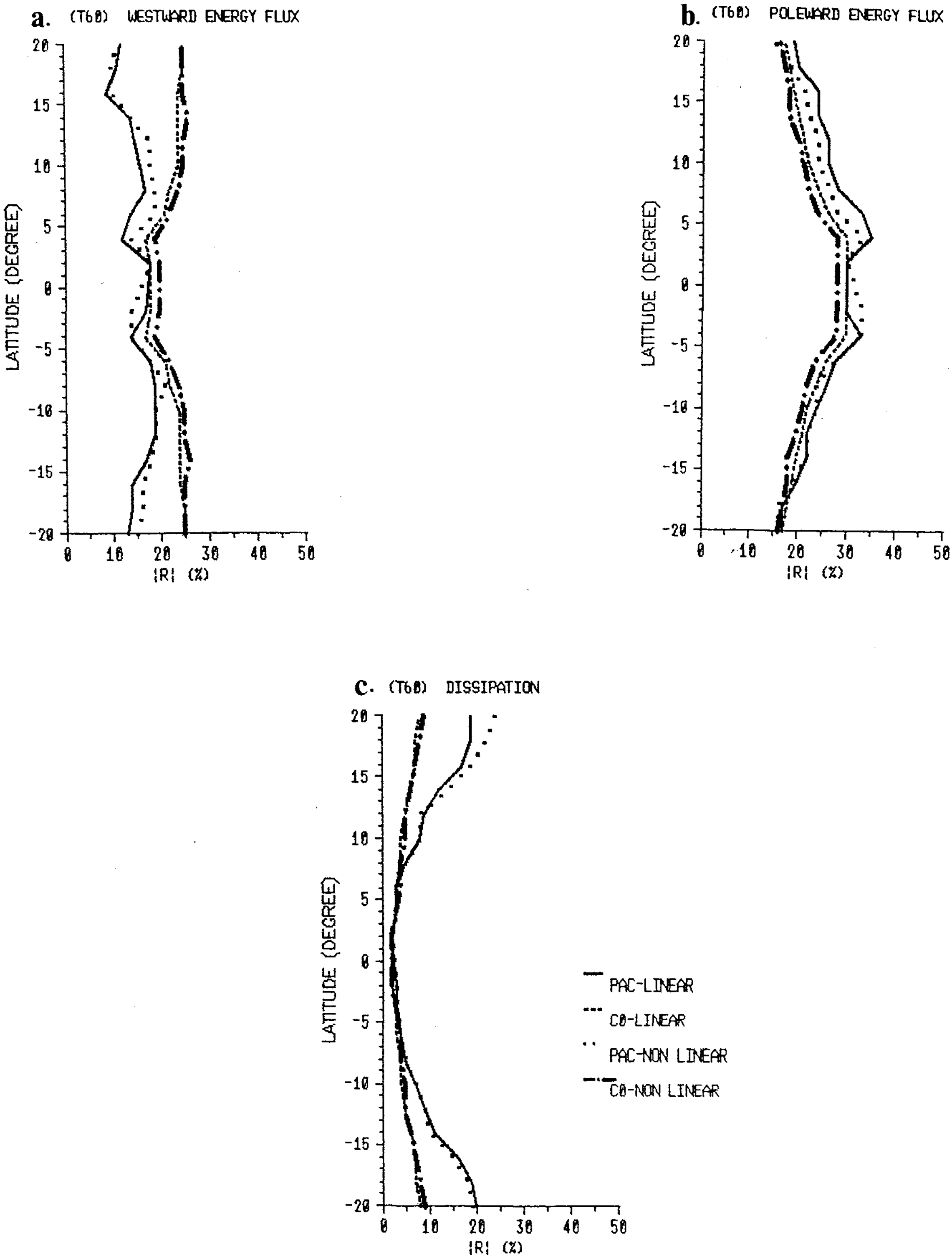

FIGURE 5.4: Energy flux coefficients (%) at different latitudes (°). (a)r_W, (b)r_P and (c)r_D. Solid line: linear and Pacific coastline. Dashed line: linear and meridional coastline. Dotted line: non linear and Pacific coastline. Centre-dashed line: non linear and meridional coastline. Wave period: 60 days.

5.2.2 Seasonal variability

To simulate the seasonal variability in the eastern Pacific ocean an equatorial Kelvin wave of 180 days period was used as an initial condition for the numerical model.

The intraseasonal energy fluxes, as shown in the previous section, are significantly more affected by the coastline geometry than by the nonlinearities. Thus hereafter only the linear model is used for the investigations.

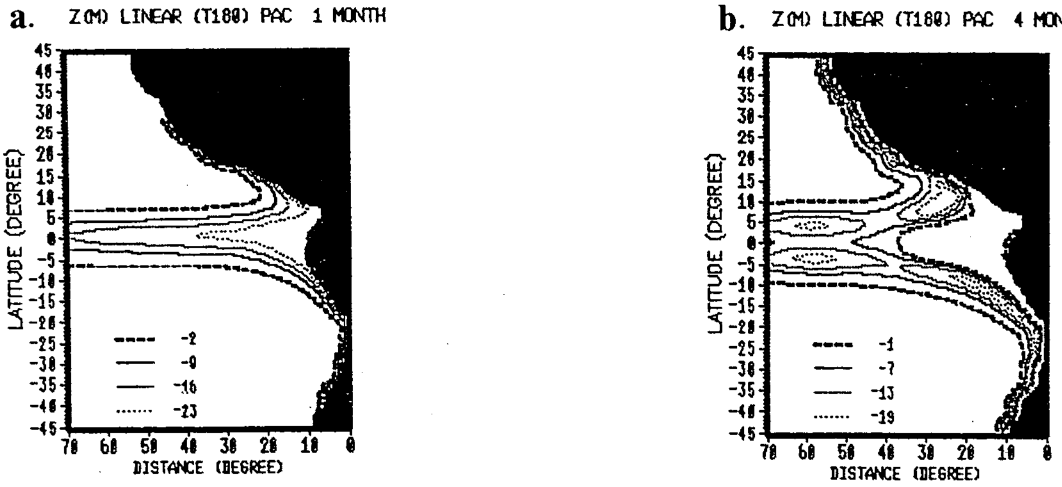

FIGURE 5.5: Z (m) at (a)1 and (b)4 months. Pacific coastline. Wave period: 180 days.

The modeled region has, now, a latitudinal extent of 90° (from 45°S to 45°N) and a maximum longitudinal extent of 175° (see Figure 5.5 for the boundary geometry). The numerical model was integrated for 6 months.

Figure 5.5 shows the latitude-longitude plot of the height anomaly (in metre), generated at the Pacific coast, after 1 and 4 months. Only the eastern domain (70°) is shown. The Pacific upper layer fields (Figure 5.5), near the coast, resemble the fields generated by the C60 experiment (Figure 4.14).

The non dimensional energy flux and the energy dissipation coefficients, for this experiment, are shown in Figure 5.6 for different latitudes. The coefficients were calculated at every 5° of latitude and integrated over 6 months. Figure 5.6 shows that the asymmetry between the Northern and Southern Hemispheres is small. Poleward of ~20° of latitude, the dissipation of energy is larger than either of the energy fluxes.

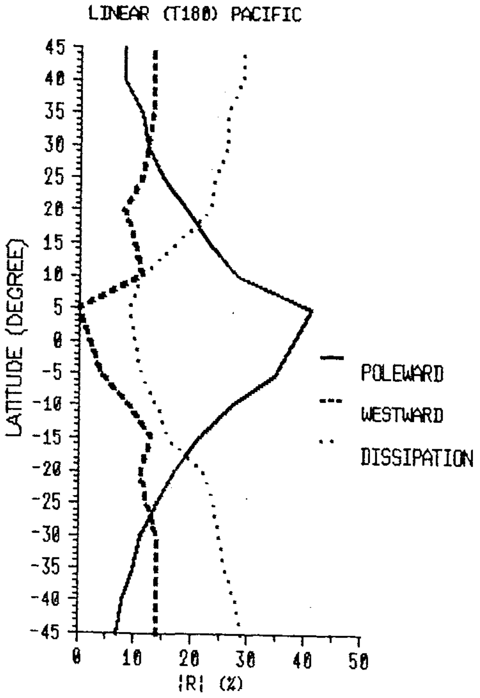

FIGURE 5.6: Linear energy flux coefficients (%) at different latitudes (°). Solid line: r_N. Dashed line: r_W. Dotted line: r_D. Wave period: 180 days. Pacific coastline.

In order to compare the energy flux change induced by the coastline geometry, the coefficients presented in Figure 5.6 have been plotted together and are presented in Figure 5.7 with the analogous coefficients generated in Experiment C0.

In agreement with the intraseasonal period experiment, the Pacific boundary is less reflective than the meridional boundary (see Figure 5.7-a). The Pacific poleward energy flux (Figure 5.7-b) is slightly smaller than that generated at $\gamma=0°$ because of the larger dissipation of energy occurring in the Pacific (Figure 5.7-c) which prevents an increase of poleward energy flux induced by the coastline geometry.

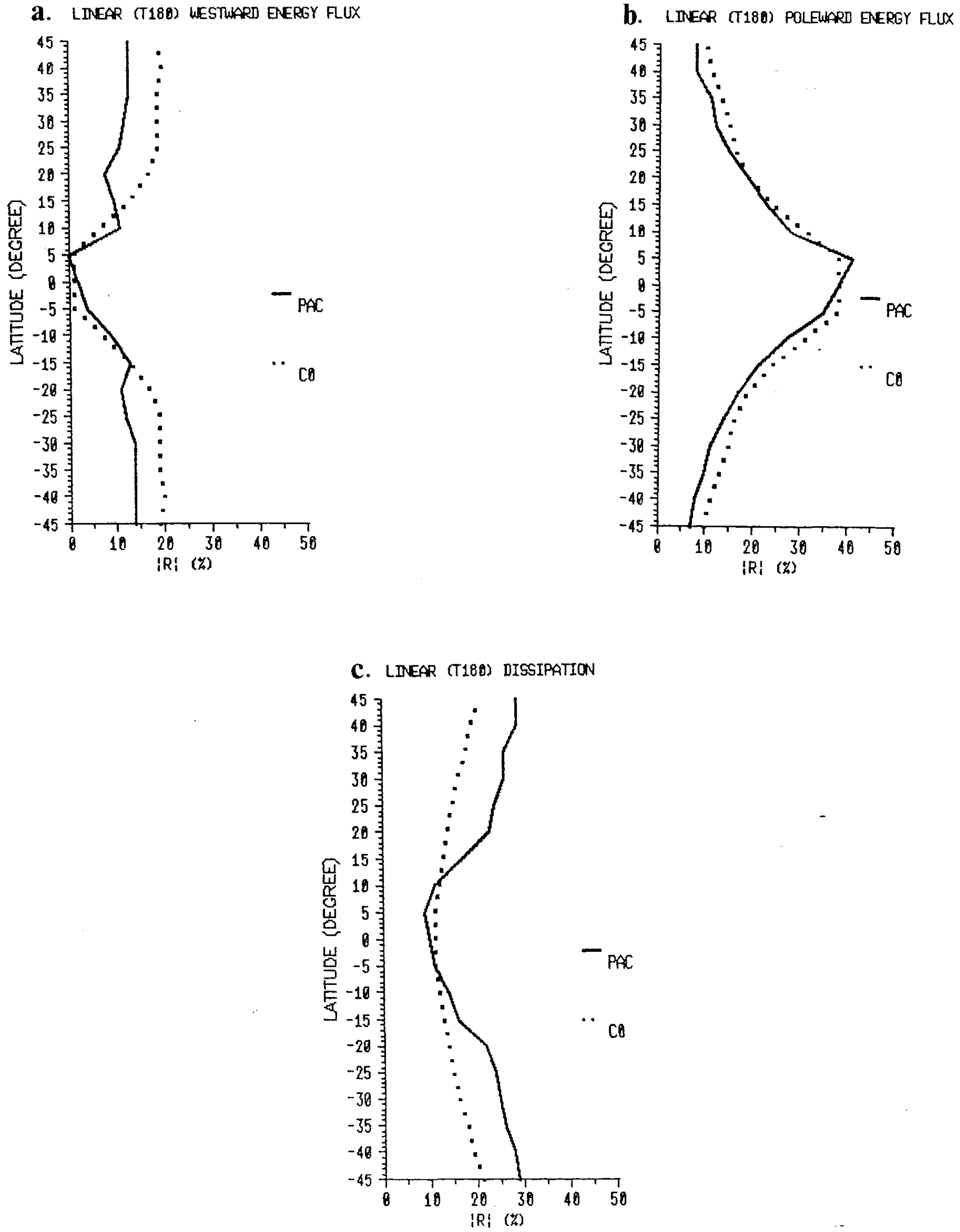

FIGURE 5.7: Linear energy flux coefficients (%) at different latitudes (°). (a)r_W, (b)r_P and (c)r_D. Solid line: Pacific coastline. Dotted line: meridional boundary. Wave period: 180 days.

5.2.3 Annual variability

Similarly to Section 4.5, a half wavelength of an equatorial Kelvin wave of annual period (360 days) is used as an initial condition for the linear numerical model. The numerical domain utilized in the experiment has a maximum longitudinal extent of 350° and a latitudinal extent of 90° (from 45°S to 45°N). Figure 5.8 shows the upper layer anomaly after 1 and 6 months of integration. Only the eastern 70° is displayed in the figure. As has been shown previously, near the coast, the Pacific height field anomalies resemble more the fields generated in Experiment C60 (Figure 4.18) than those generated in Experiment C0 (Figure 4.17).

Following the methodology of the previous experiment the poleward energy flux and the dissipation of energy were numerically calculated for every 5° of latitude and integrated over 8 months.

The eastward energy flux, t_E, was estimated using a longitudinally doubled domain (700°). Repeatedly, t_E was calculated at the middle of this larger domain, at 350° from the coast ($t_E = 2.8\ 10^{10}\ m^5s^{-3}$). The westward energy flux was then obtained using energy conservation considerations.

The energy flux and the energy dissipation coefficients are shown in Figure 5.9. According to Figure 5.9, the annual northward and southward energy fluxes are symmetric about the equator. Poleward of 20°N the dissipation of energy is dominant over the energy fluxes in the Northern Hemisphere; in the Southern Hemisphere, however, the coastline geometry facilitates the boundary reflection and the westward energy flux is larger than the dissipation of energy.

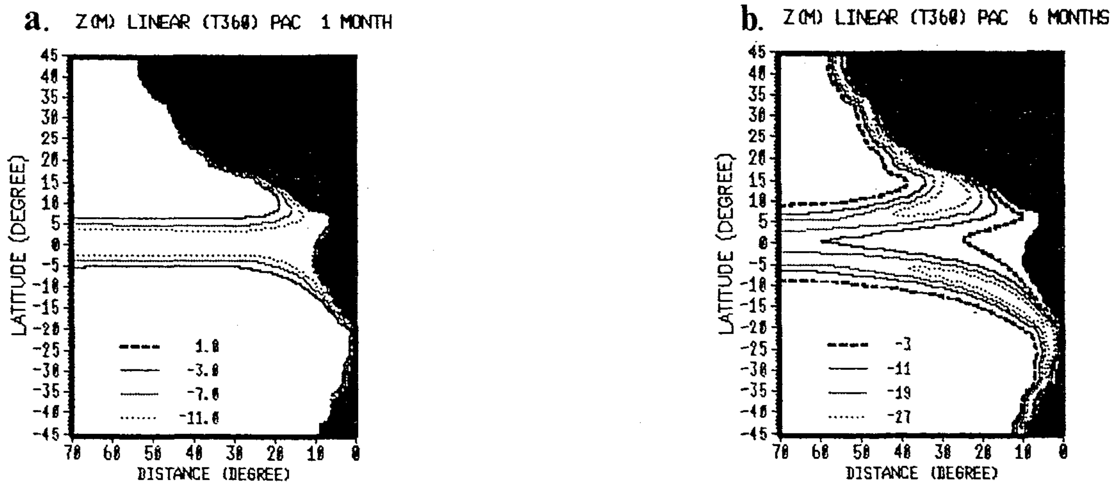

FIGURE 5.8: Z (m) at (a)1 and (b)6 months. Pacific coastline. Wave period: 360 days.

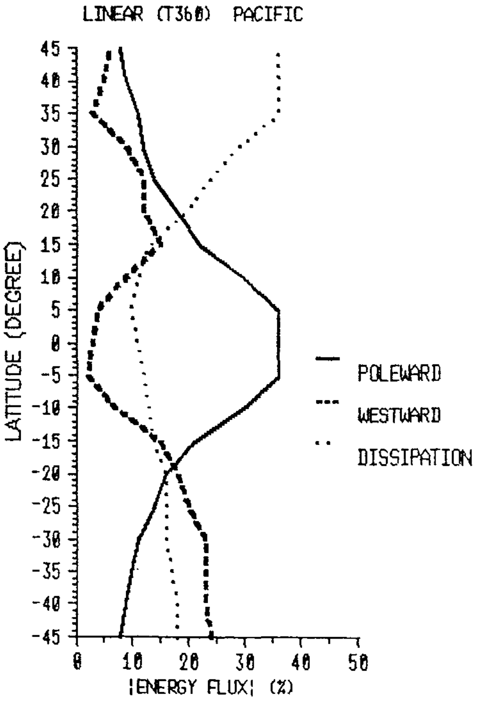

FIGURE 5.9: Linear energy flux coefficients (%) at different latitudes (°). Solid line: r_P. Dashed line: r_W. Dotted line: r_D. Pacific coastline. Wave period: 360 days.

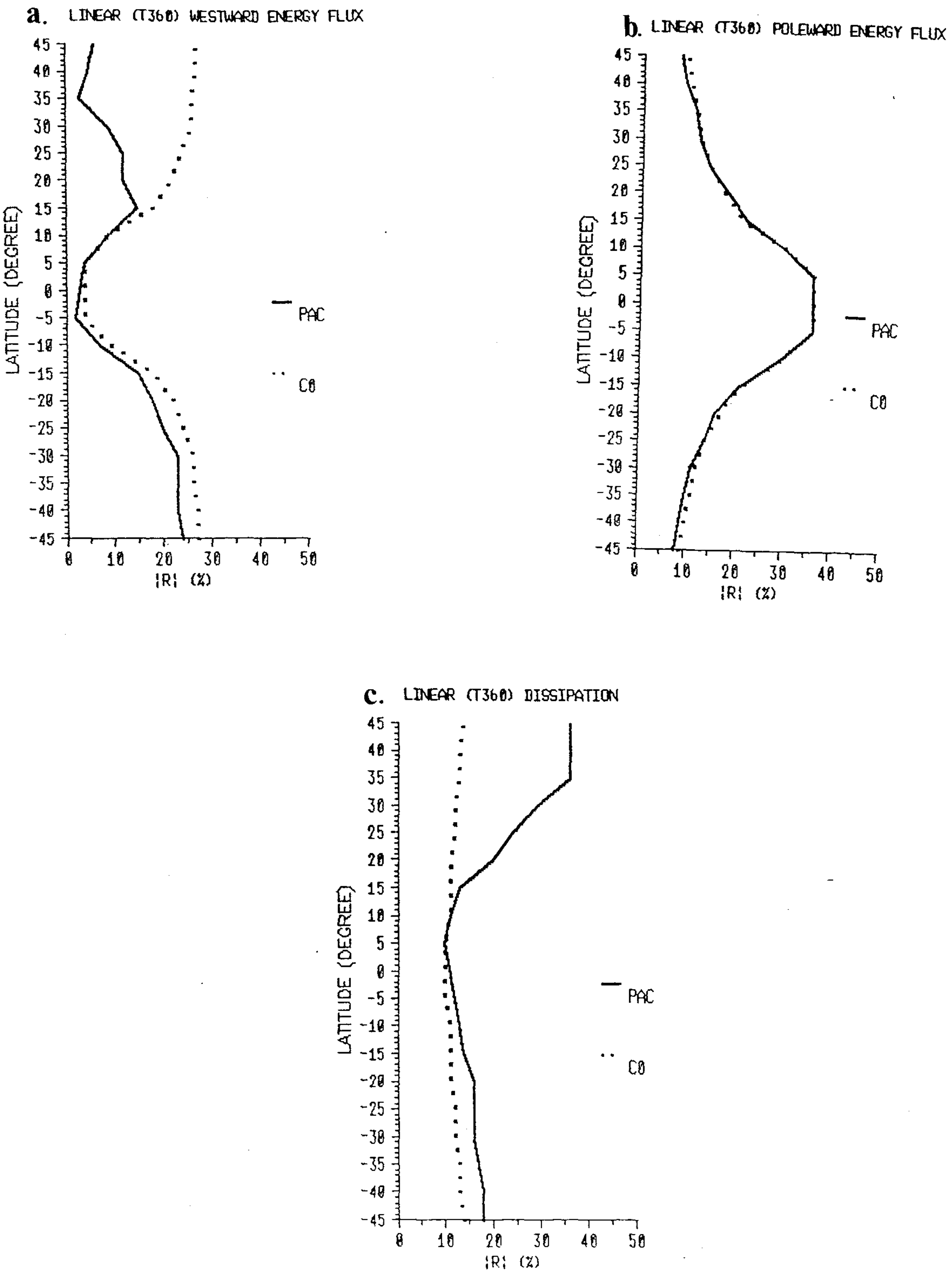

FIGURE 5.10: Linear energy flux coefficient (%) at different latitudes (°). (a)r_W, (b)r_P and (c)r_D. Solid line: Pacific coastline. Dotted line: meridional boundary. Wave period: 360 days.

The influence of the coastline on the energy fluxes and on the energy dissipation is very clear in Figure 5.10, where the nondimensional coefficients generated using the Pacific boundary and the meridional boundary are displayed together.

In the Southern Pacific, the energy fluxes and the energy dissipation are not substantially different from those generated in the meridional boundary experiment. This is expected given that the Southern Pacific coastline does not depart significantly from a meridional orientation.

In the Northern Pacific, the westward energy flux differs substantially from that generated in Experiment C0 (Figure 5.10-a). The poleward energy fluxes generated in the eastern Pacific and in Experiment C0 (Figure 5.10-b) are similar. The dissipation of energy (Figure 5.10-c), which increases as the boundary departs from the meridional direction, restrains the increase in the northward energy flux induced by the coastline geometry.

5.2.4 Summary

Figure 5.11 summarizes the energy fluxes and the energy dissipation coefficients obtained for the Pacific Ocean at intraseasonal, seasonal and annual periods. The intraseasonal coefficients were calculated only up to 20° of latitude and therefore a direct comparison between the intraseasonal coefficients and the lower frequency coefficients should be made with prudence.

As already stated in Chapter 4, the energy fluxes are strongly dependent on the energy dissipated in the domain. In the Southern Hemisphere, the dissipation of energy is smaller in the annual experiment than in the seasonal one (Figure 5.11-c). This can be explained by the critical latitude values being higher for the annual experiment. Therefore, in this case the increase in dissipation due to the increase of period is shown to be less important than the energy dissipated by the presence of coastal Kelvin waves. In the Northern Hemisphere, however, the energy dissipated in the annual case is larger than that for the seasonal case. This is, probably, due to the combination of both the presence of the coastal Kelvin waves in the domain and the increase in the wave period.

In agreement with the results presented in Chapter 4, the intraseasonal values of r_W (Figure 5.11-a) and r_D (Figure 5.11-c) are, respectively, larger and smaller than those obtained by the lower frequency experiments.

The westward energy flux, in the Southern Hemisphere, is larger for the annual period experiment than for the seasonal period case. In the Northern Hemisphere (where the boundary is more nonmeridional) the comparatively larger presence of coastal Kelvin waves, in the annual period experiment, induces stronger dissipative effects (see Figure 5.11-c) inhibiting the reflection processes. As a result, less energy of annual period is propagated offshore (see Figure 5.11-a).

Calculations for the intraseasonal, seasonal and annual frequencies all indicated that the coastally trapped energy flux, poleward of 15°, does not depend significantly on the period of the incident wave (see Figure 5.11-b). The northward and southward energy flux asymmetry is also negligible for all the investigated frequencies. The symmetry of r_p is explained by the larger dissipative effects in the Northern Hemisphere which compensate for the increase of the northward energy flux generated by the coastline geometry.

The Hemispherical asymmetry of both, westward energy flux and energy dissipation, are larger for the annual experiment. This result is in agreement with Clarke (1992), who has found that the energy flux asymmetry in the eastern Pacific increases as the period increases.

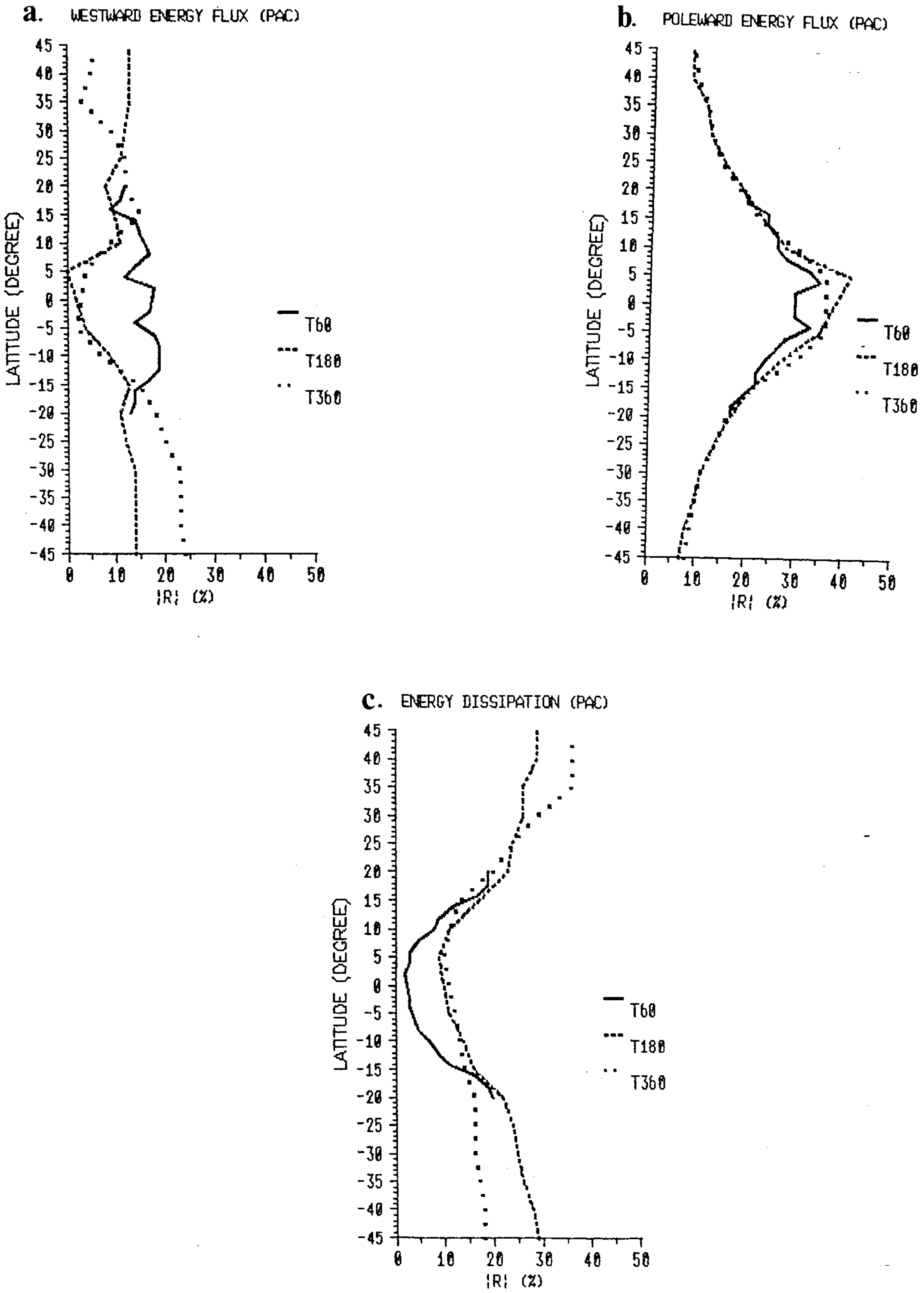

FIGURE 5.11: Linear energy flux coefficients (%) at different latitudes, for different incident wave periods. (a)r_W, (b)r_P and (c)r_D. Pacific boundary.

5.3 Atlantic Ocean

The experiments carried out for the Pacific Ocean (Section 5.2), have been repeated for the Atlantic Ocean. The methodology employed is similar to that utilized in the previous section.

The Atlantic coastline geometry, used in the experiments, is shown in Figures 5.12 (for the intraseasonal period) and 5.16 (for the seasonal and annual periods).

5.3.1 Intraseasonal variability

5.3.1.1 Linear case

The Atlantic linear height field anomaly generated by an incident equatorial Kelvin wave of 60-day period is shown in Figure 5.12 at six successive intervals of 15 days. Except very near the Gulf of Guinea, the Atlantic field (Figure 5.12) resembles the field generated at $\gamma=60°$ (Figure 4.4).

The principal effect of the approximately east-west coastline at 5°N is to add a narrow boundary current which widens westward, as evident in Figure 5.13-b.

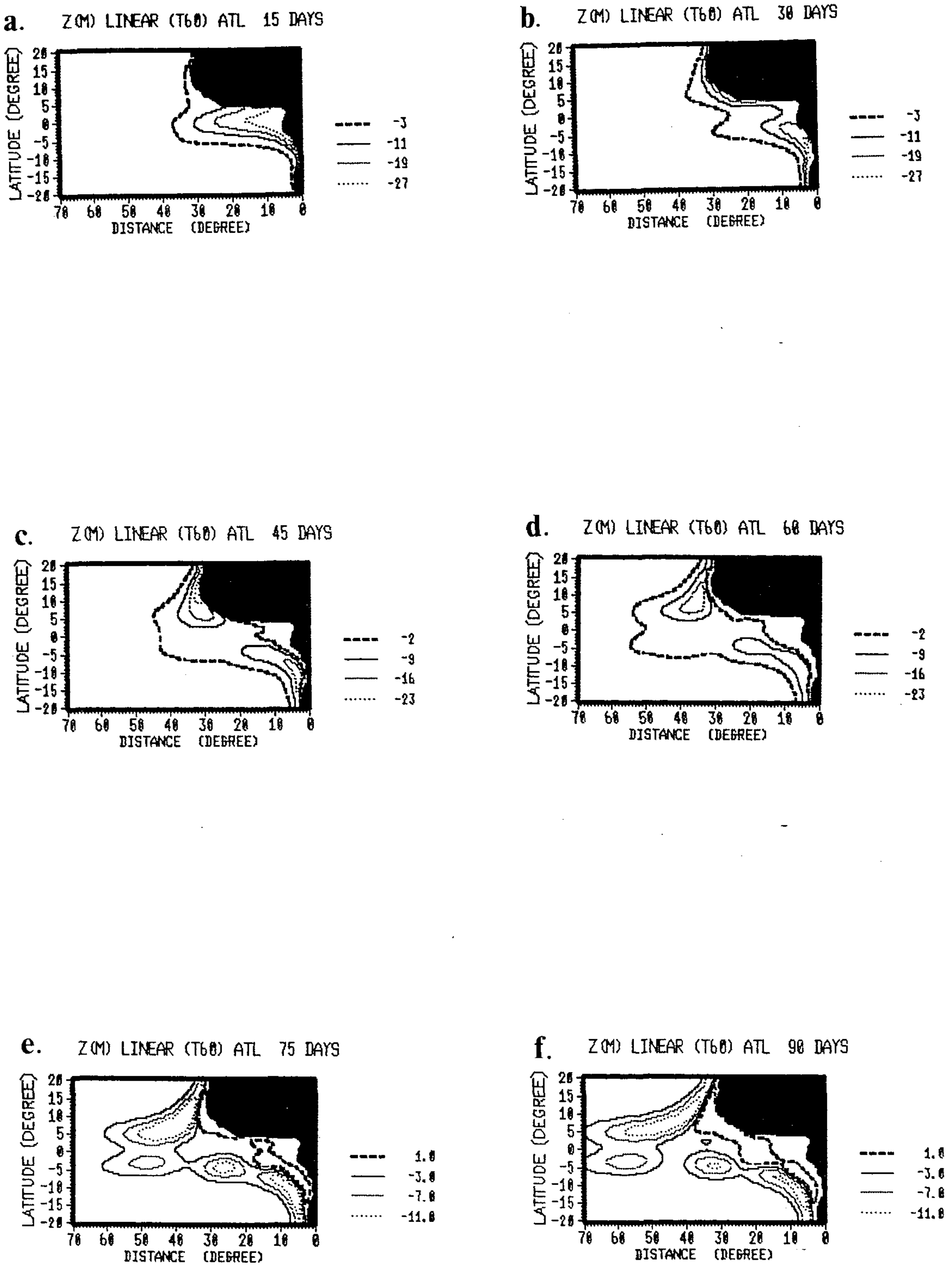

Figure 5.12: Sequential patterns of Z (in metre), at (a)15, (b)30, (c)45, (d)60, (e)75 and (f)90 days. Wave period: 60 days. Atlantic coastline.

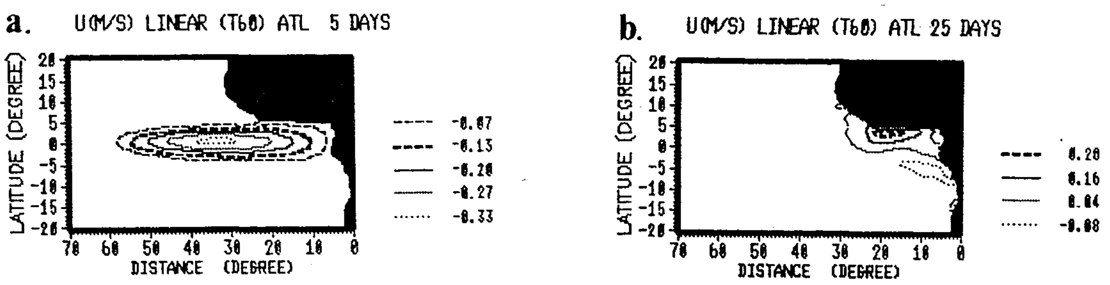

FIGURE 5.13: Zonal velocity (m/s), at (a)5 and (b)25 days. Wave period: 60 days. Atlantic coastline.

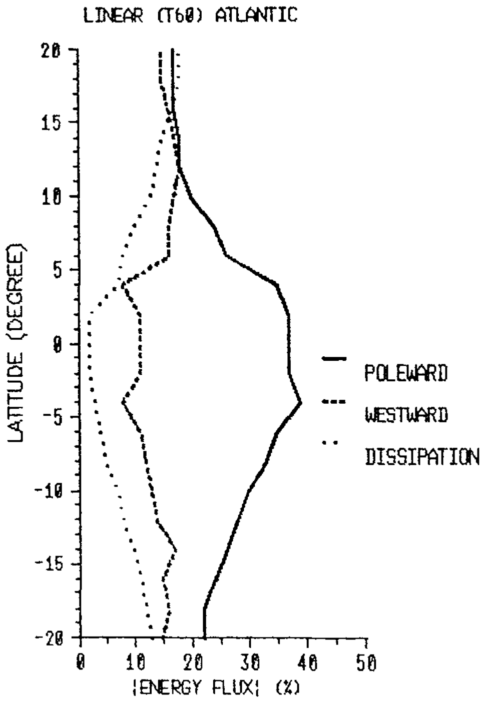

FIGURE 5.14: Linear energy flux coefficients (%) at different latitudes (°). Solid line: r_P. Dashed line: r_W. Dotted line: r_D. Wave period: 60 days. Atlantic Ocean.

This boundary layer is too narrow to be a single coastally trapped meridional mode (Cane and Patton, 1984); instead, it is a sum and difference of the (anti-symmetric) Rossby-Kelvin wave and the (symmetric) anti-Kelvin wave (see Figure 2.2), which are taken to produce isolated coastal Kelvin waves (Cane and Sarachik, 1979).

The flow produced by the coastal Kelvin wave along the zonal boundary is opposite in direction to the phase propagation. The eastward propagating wave produces a flow to the west. The westward wave propagating along the east-west boundary produces a flow to the east. Both these results can be clearly seen in the zonal velocity fields at days 5 and 25, shown in Figure 5.13.

The nondimensional linear energy flux coefficients, $r_P(\gamma,T)$, $r_W(\gamma,T)$ and $r_D(\gamma,T)$ generated at the eastern Atlantic coast are shown in Figure 5.14 at different latitudes. The coefficients were calculated at latitudinal intervals of 2° and integrated over 90 days.

According to Figure 5.14, near the Gulf of Guinea, both the reflected energy flux and the dissipated energy exhibit a rapid increase whereas the poleward energy flux presents a rapid decrease. The increase in the r_D value is due to the energy dissipated along the zonal boundary (see Figure 5.13-b). The larger amount of dissipation, consequently, reduces the northward energy flux (see Chapter 4).

5.3.1.2 Non linear case

The intraseasonal non linear results are presented. Following the methodology of Section 5.2.1.2, the energy coefficients are calculated using the: (1) Atlantic coastline and the linear model (solid line); (2) meridional coastline and the linear model (dashed line); (3) Atlantic coastline and the non linear model (dotted line) and (4) meridional boundary and the non linear model (centre-dashed line). The results are presented in Figure 5.15.

In agreement with the earlier experiments, the energy flux changes induced by the coastline geometry are significantly more important than those induced by the nonlinearities (Figure 5.15).

The Atlantic coastline is shown by Figure 5.15-a to be less reflective than the meridional one. This result is expected theoretically given that the critical latitudes for the nonmeridional boundaries are lower than those generated at the meridional coastlines (see Section 2.4.1).

For the four cases presented in Figure 5.15-b, poleward of 5°N, the northward energy fluxes present similar values. This means that north of 5°N the Northern Atlantic coastline acts, in terms of intraseasonal poleward energy flux, as a meridional boundary. In the Southern Hemisphere, the poleward energy generated in the Atlantic coastline is larger than that generated in Experiment C0. In concordance with the previous experiments the energy dissipation induced by the nonmeridional boundary (Atlantic coastline) is larger than that induced by the meridional one (Figure 5.15-c). The increase in dissipation prevents the expected rise in the poleward energy flux induced by the geometry of the coastline.

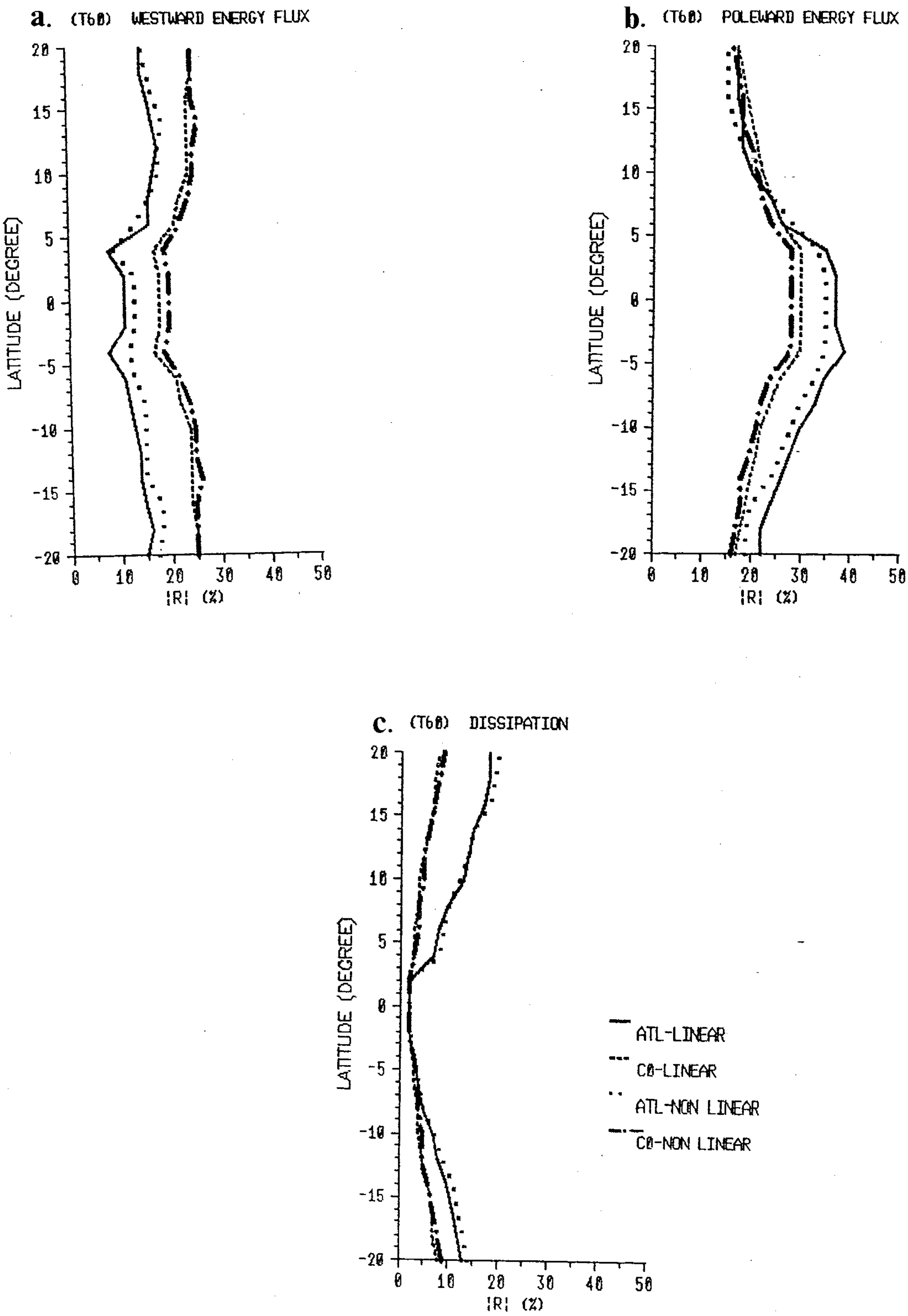

FIGURE 5.15: Energy flux coefficient (%) at different latitudes (°). (a)r_W, (b)r_P and (c)r_D. Solid line: linear model and Atlantic coastline. Dashed line: linear model and meridional coastline. Dotted line: non linear model and Atlantic coastline. Centre-dashed line: non linear model and meridional coastline. Wave period: 60 days.

5.3.2 Seasonal variability

Only the Atlantic eastern domain (70°) is shown in the Figure 5.16, where the plot of the height field anomaly is displayed after 1 and 4 months of the integration. Note that for the seasonal period case, the resemblance between the Atlantic field (Figure 5.16) and Experiment C60 field (Figure 4.14) is smaller than it was for the intraseasonal period experiment.

Figure 5.17 shows the energy flux coefficients calculated at every 5° of latitude and integrated over 6 months. The asymmetry between the Northern and Southern Hemispheres is found to be negligible for all the seasonal energy fluxes investigated here. This indicates that the geometrical effects of the Gulf of Guinea are not very important for seasonal period motions.

In order to compare the energy flux change induced by the coastline geometry, the coefficients presented in Figure 5.17 have been plotted together and are shown in Figure 5.18 with their analogous fluxes generated in Experiment C0. As for the intraseasonal period experiment, the Atlantic boundary is less reflective than the meridional boundary (see Figure 5.18-a).

According to Figure 5.18-b, concerning the seasonal poleward energy flux the whole eastern Atlantic boundary can be regarded to approximate a meridional boundary. Again, the comparatively larger energy dissipated at the eastern Atlantic boundary (Figure 5.18-c) offsets the expected increase of poleward energy flux induced by the coastline geometry.

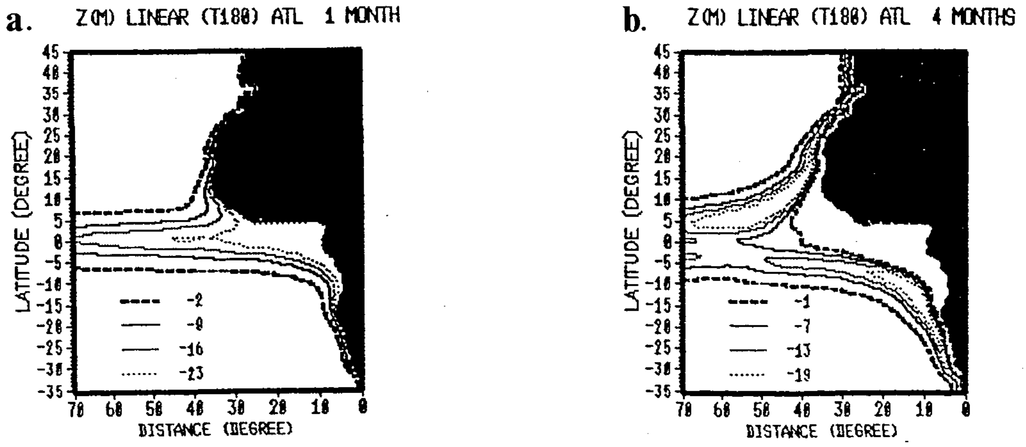

FIGURE 5.16: Z (m) at (a)1 and (b)4 months. Atlantic coastline. Wave period: 180 days.

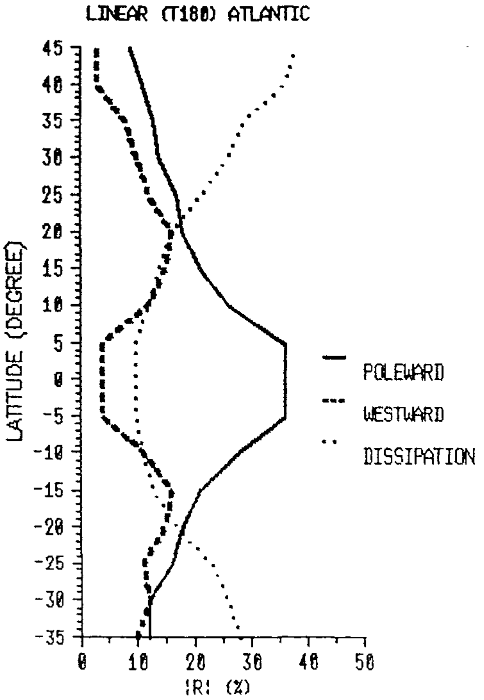

FIGURE 5.17: Linear energy flux coefficients (%) at different latitudes (°). Solid line: r_N. Dashed line: r_W. Dotted line: r_D. Wave period: 180 days. Atlantic coastline.

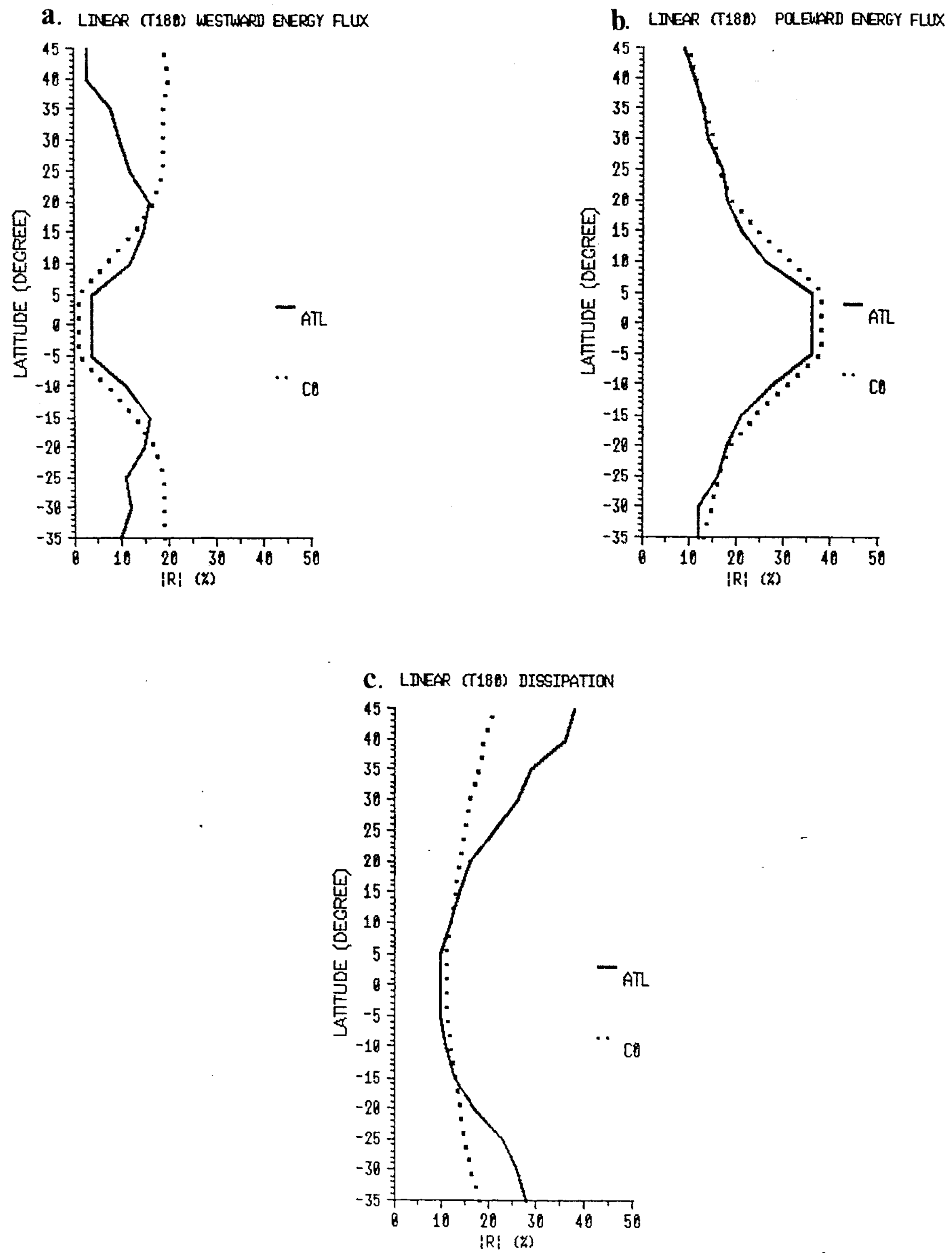

FIGURE 5.18: Linear energy flux coefficient (%) at different latitudes (°). (a)r_W, (b)r_P and (c)r_D. Solid line: Atlantic coastline. Dotted line: meridional boundary. Wave period: 180 days.

5.3.3 Annual variability

Figure 5.19 shows the upper layer anomaly after 1 and 6 months of integration. Only the eastern 70° from the Atlantic coast is displayed in Figure 5.19. For the annual period motion, the Atlantic field resembles more the height field generated in Experiment C0 (Figure 4.17) than that generated in Experiment C60 (Figure 4.18).

The annual energy flux coefficients calculated at every 5° of latitude and integrated over 8 months, are displayed in Figure 5.20. In common with the seasonal experiment, all the annual energy coefficients are approximately symmetric about the equator (Figure 5.20).

To compare the coastline influences on the energy fluxes and on the energy dissipation, the nondimensional coefficients generated by the Atlantic coastline and by the meridional boundary are displayed together in Figure 5.21.

Figure 5.21-b shows that the annual poleward energy fluxes induced by both meridional and Atlantic boundaries are similar. As expected, the energy dissipated (Figure 5.21-c) and the reflected flux (Figure 5.20-a) are, respectively, larger and smaller in the Atlantic than in Experiment C0.

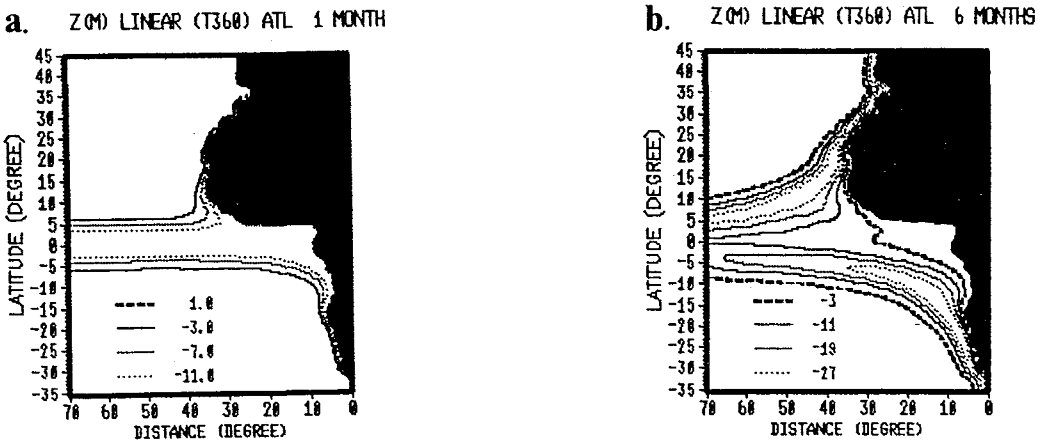

FIGURE 5.19: Z (m) at (a)1 and (b)6 months. Atlantic coastline. Wave period: 360 days.

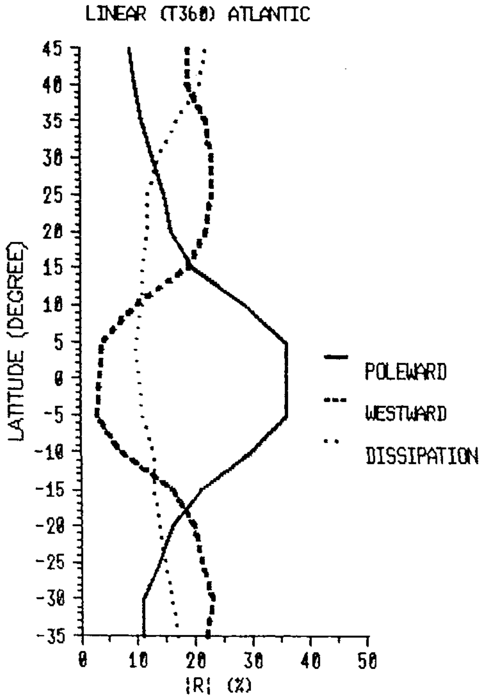

FIGURE 5.20: Linear energy flux coefficients (%) at different latitudes (°). Solid line: r_P. Dashed line: r_W. Dotted line: r_D. Atlantic coastline. Wave period: 360 days.

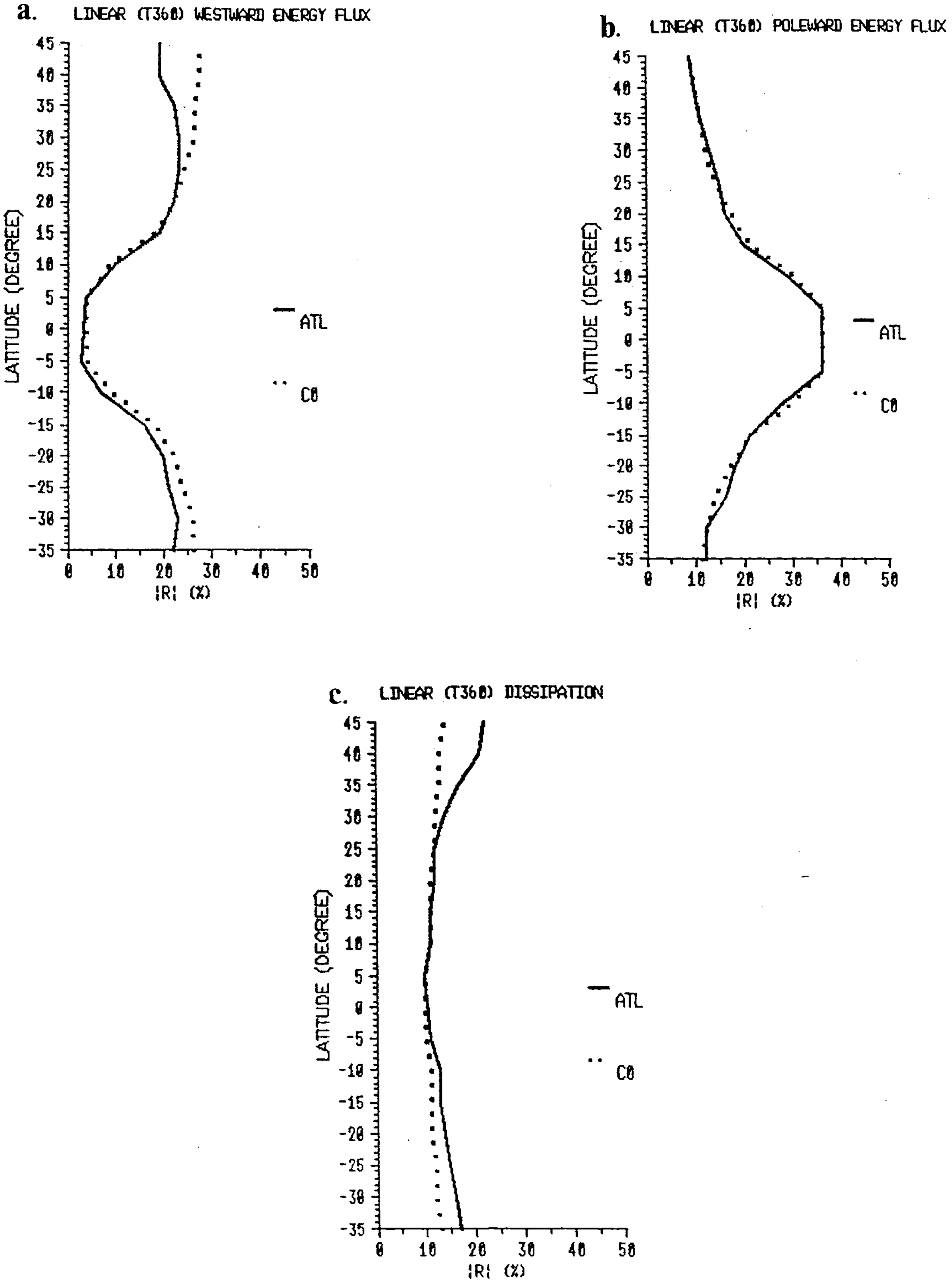

FIGURE 5.21: Linear energy flux coefficient (%) at different latitudes (°). (a)r_W, (b)r_P and (c)r_D. Solid line: Atlantic coastline. Dotted line: meridional boundary. Wave period: 360 days.

5.3.4 Summary

The intraseasonal, seasonal and annual energy fluxes and energy dissipation coefficients are shown in Figure 5.22.

In agreement with both the previous section (Figure 5.11-a) and Chapter 4 (Figure 4.21), the westward energy flux is larger for the intraseasonal period than for the longer periods (Figure 5.22-a). This is explained by the smaller values of energy dissipated in the domain, in the intraseasonal experiment (Figure 5.22-c). These smaller values are due to the shorter period wave used in this experiment when compared to the seasonal and annual period waves (see ϵ in Section 4.7).

For the seasonal and the annual period experiments, as the period increases, the reflected energy increases (Figure 5.22-a) and the dissipation of energy decreases (Figure 5.22-c). These results can be explained by the higher values of the critical latitude obtained for larger periods (see Section 2.5.1). The higher the critical latitude the larger is the latitude band over which Rossby waves radiated from the boundary and, consequently, the smaller the amount of energy dissipated in the domain.

It is found that the seasonal and the annual poleward energy fluxes are very similar (see Figure 5.22-b). Both fluxes are also comparable to the poleward energy flux generated at the meridional boundary. Despite the reflected energy being smaller for the seasonal case than that generated by the annual experiment, the seasonal energy dissipated in the domain is larger, resulting in similar values of the poleward energy fluxes for both periods.

The influence of the Atlantic coastline geometry, therefore, on the seasonal and annual coastally trapped energy flux can be considered irrelevant. This result is striking because of the particular geometry of the eastern Atlantic, which has an approximately zonal coast near 5°N (Gulf of Guinea). However, Du Penhoat et al.(1983) have shown that the effect of the coast of the Gulf of Guinea is very small on low frequency waves (seasonal and annual periods).

The effect of the Gulf of Guinea coastline on the comparatively higher frequency (intraseasonal period), however, is not negligible. The largest asymmetry between the Northern and Southern Hemisphere energy fluxes was found in the intraseasonal experiment (Figure 5.22).

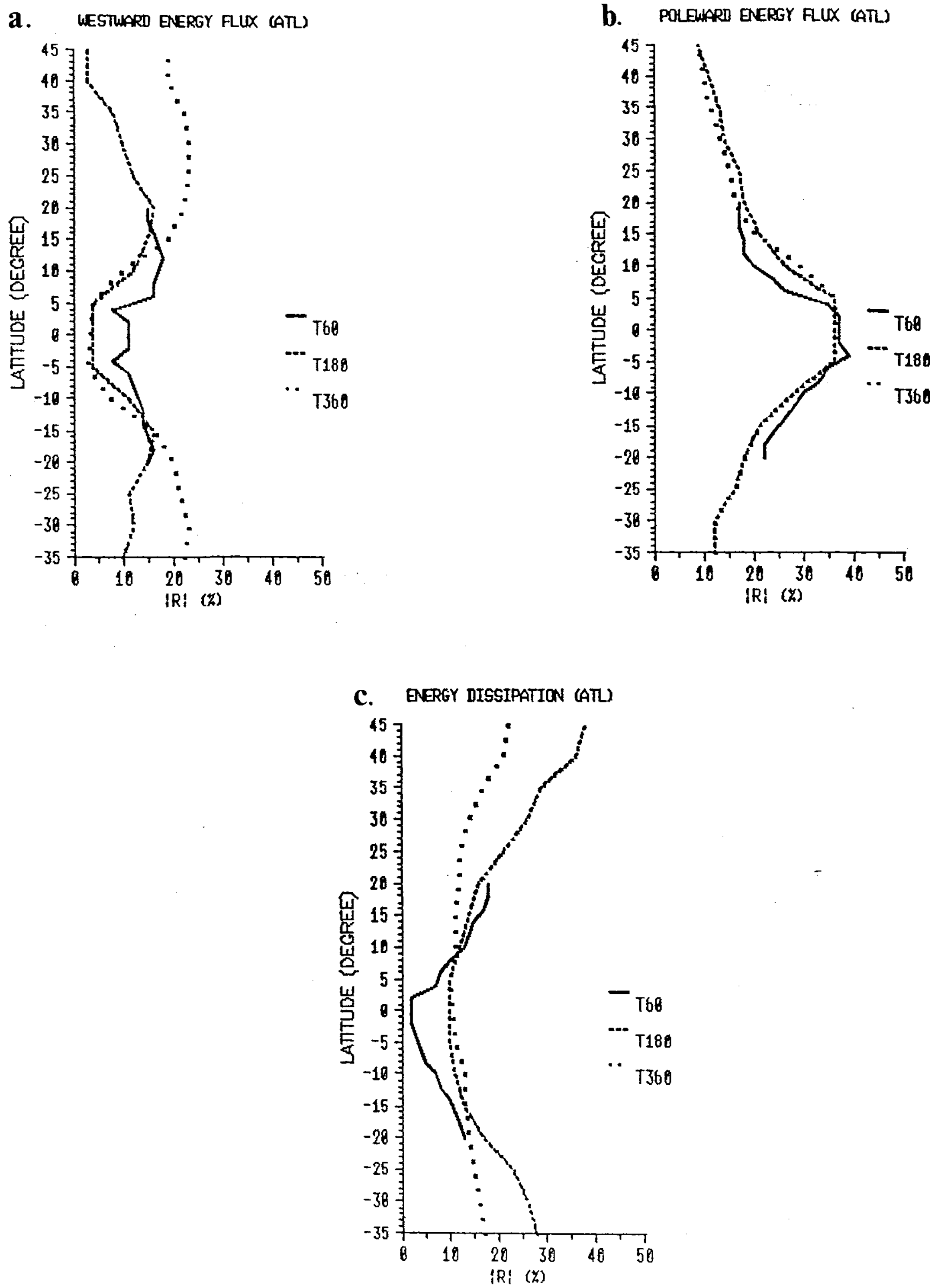

FIGURE 5.22: Linear energy flux coefficient (%) at different latitudes, for different incident wave periods. (a) r_W, (b)r_P and (c) r_D.

CHAPTER 6 - DISCUSSION

6.1 Discussion of results and conclusion

The work described in this thesis has two main aspects. The first is the development of the numerical model, and the second is the use of the model to study the low frequency reflection of the equatorial waves at different eastern ocean boundaries.

The numerical model developed in this study, is a fast, efficient, reduced gravity, 1 ½ layer model, able to simulate the linear and non linear low frequency motions on the sphere. It uses a potential vorticity and potential enstrophy numerical conserving scheme which permits time steps twice those used in other discretization schemes, like the leapfrog for example. In addition, as a two level scheme, it has no computational mode in time.

The open boundary conditions, used in the model, allow phenomena generated in the interior domain to pass through the model boundaries without distortion and without affecting the interior solution. The model was extensively tested and verified by comparing numerical results with analytical solutions to the linearised equations of motion. It was found that the model is able to correctly represent the Kelvin and Rossby wave motions that dominate the dynamics of the equatorial oceans.

A simple Laplacian representation of viscous effects with a horizontal coefficient of 10^3 m^2s^{-1}, is used in the model. The viscous model is shown to be in a "good resolution regime", which according to Hsieh et al.(1983), indicates that the wave behaviour, in the numerical model, can be considered identical to that in the continuous viscous model;

i.e, the finite-difference effects are negligible.

A standard value for the viscosity coefficient has been utilized in this study (10^3 m^2s^{-1}). Davey et al.(1983) have shown that a coefficient of the order of 10^3-10^4 m^2s^{-1} was required in their continuous Kelvin wave model in order to make the numerical onshore component of velocity comparable with that observed in the free baroclinic coastally-trapped waves off Peru.

Despite the limitations of this model, which are addressed in Section 6.2, some important conclusions can be drawn from its results.

To investigate how much of the low frequency variability at the eastern ocean boundaries (such as, for example, the El Niño related anomalies) is due to equatorial waves, the poleward energy fluxes have been numerically calculated at several latitudes. The large latitudinal extent of the numerical domain permits consideration of both equatorial and mid-latitude responses. The influence of the strength of viscosity, the incident wave period and the eastern coastline geometry, on the energy fluxes is discussed below.

According to the energy flux results nonlinear effects can be regarded as negligible for the problem considered here whereas the viscous effects are important.

The energy fluxes are found to be strongly dependent on the viscosity included in the model. If no viscosity is incorporated in the model (A_H=0), there is very good agreement between the numerical simulations and the analytical results, generated at meridional boundaries. The inclusion of dissipation, however, is imperative in the model in order to form a viscous boundary layer required to fit theory with observations (Davey et al., 1983).

It is concluded that the differences between the analytical and the numerical energy fluxes are primarily due to the inclusion of dissipative effects in the numerical model. To a lesser degree other factors are also suggested to contribute to the discrepancy obtained between these results. The utilization of the equatorial β-plane approximation in the analytical expressions (as given by Clarke, 1992) can allow an artificial generation of Rossby waves at higher latitudes. The validity of the analytical expressions, for coastline angles greater than 40°, is also questionable.

The experiments described in Chapter 4 have shown that the poleward coastal Kelvin wave energy flux has a tendency to increase with a decrease of the critical latitude. The critical latitude, in its turn, decreases with the increase of the angle of coastline inclination and with the decrease of the incident wave period. Opposing the rise of the poleward energy flux there are, however, the frictional effects.

For a given eastern boundary, the amount of energy dissipated in the domain is shown to be dependent on the wave period in two conflicting ways:

(1) for the specific problem investigated here, longer wave periods in the domain result in higher critical latitudes and a reduction in the presence of coastal Kelvin waves. Thus the dissipation of energy decreases as the wave period increases;
(2) the amount of energy dissipated by the coastal Kelvin waves increases as the period of the wave increases (this result is in agreement with Davey et al., 1983).

Therefore, the final amount of energy taken from the domain by dissipation, therefore, depends not only on the presence of the coastal Kelvin waves in the domain, but also on the period of these coastal waves.

The influence of the coastline geometry and the incident wave period, was found to be more important for the westward energy flux than for the poleward flux. It is suggested that to accurately simulate the reflected Rossby waves on the Pacific and Atlantic boundaries, the eastern ocean coastline geometry should be included in the numerical models.

In agreement with the inviscid theory, in the viscous case the nonmeridional boundaries were found to be less reflective than the meridional ones. The westward energy flux, according to the inviscid theory, should increase with the increase of the incident equatorial wave frequency. For the viscous case, however, this result is not always verified. In all the experiments performed (Chapter 4 and 5) the intraseasonal reflected energy, for example, is found to be larger than for those of lower periods. This is explained by the comparatively smaller values of energy dissipated, in the domain, in the intraseasonal experiments.

The effects of the boundary inclination on the poleward energy flux, for the Pacific and Atlantic Oceans, were found to decrease as the period of the incident wave increased. For motions of seasonal and annual periods, the influence of the coastline inclination, on both oceans, can be considered negligible.

For incident waves of intraseasonal period, however, there is a poleward energy flux asymmetry between the Northern and Southern Hemispheres. For the Northern Atlantic, poleward of 5°N, the eastern boundary can be considered as a meridional one whereas for the Southern Atlantic the eastern coastline geometry should be incorporated to obtain accurate poleward propagation of intraseasonal period. In the Pacific Ocean, the northward energy flux was found to be somewhat larger than the northward flux generated at a meridional boundary. In the Southern Hemisphere, however, the difference between the poleward fluxes, of intraseasonal period, generated at the meridional and the Pacific coastlines can be considered negligible.

In summary, results from the eastern Atlantic and Pacific Oceans suggest that the poleward energy fluxes from meridional boundary models should give plausible results for motions of seasonal and annual periods. For comparatively shorter periods, the coastline geometry should be included to obtain more accurate results. It is also recommended that any numerical model involving the reflected baroclinic Rossby waves (of intraseasonal, seasonal or annual periods) on the eastern Pacific or Atlantic Oceans, should consider the effect of the coastline geometry in order to improve the accuracy of the results.

6.2 Critique of the model and future directions

The numerical model used in this work omits some potentially important factors which may influence wave propagation. The more important of these are briefly considered in this section.

6.2.1 Poleward variation of the thermocline

To investigate the importance of the poleward variation of the thermocline depth on coastal wave propagation, some experiments have been performed. The analytical solution of this problem is complicated by the dependence of solutions on latitude.

The experiments use a numerical domain of 40° (from 10°S to 50°S) of latitudinal extent and 3° of longitudinal extent. The results were obtained using the inviscid model; the inclusion of the viscosity only increases the decay of coastal waves as they propagate poleward (not shown here).

An analytical solution to the coastally trapped Kelvin wave, of 10 day period, was specified as an oscillatory northern boundary condition. The numerical experiments were performed using different slopes of the thermocline depth. The first experiment (E1) uses a flat thermocline of 200 m depth. The second experiment (E2) considers the thermocline depth linearly tilted in latitude, varying from 200 m at 10°S to 100 m at 50°S. The third experiment (E3) considers a steep thermocline front; the profile of the thermocline is chosen so that it changes linearly from 200 m to 100 m, from 20° to

30°S. The fourth experiment (E4) assumes a main thermocline varying linearly in latitude from 200 m at 10°S to 300 m at 50°S (see Figure 6.1).

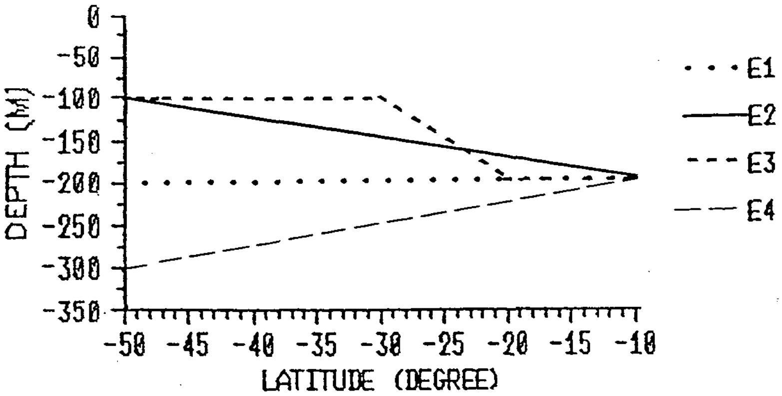

FIGURE 6.1: Meridional cross section of the thermocline depth.

The results of those experiments are displayed in Figure 6.2 as time-latitude plots of the thermocline anomaly near the coast.

According to Figure 6.2-a, the meridional wavelength is conserved when the coastal Kelvin wave propagates on a flat thermocline. The zonal wave trapping scale (Rossby radius of deformation), however, reduces when the wave propagates poleward, which results in an increase of the wave amplitude to preserve the wave total energy. The wave propagates with a phase speed of ~2.5 m/s.

Figures 6.2-b and -c show that the meridional wavelength becomes shortened when the Kelvin wave propagates into the shallower thermocline. The effect of a sloping thermocline is to reduce the poleward wave propagation. The wave velocity of experiment E2 is ~2.3 m/s and of E3 is ~1.9 m/s.

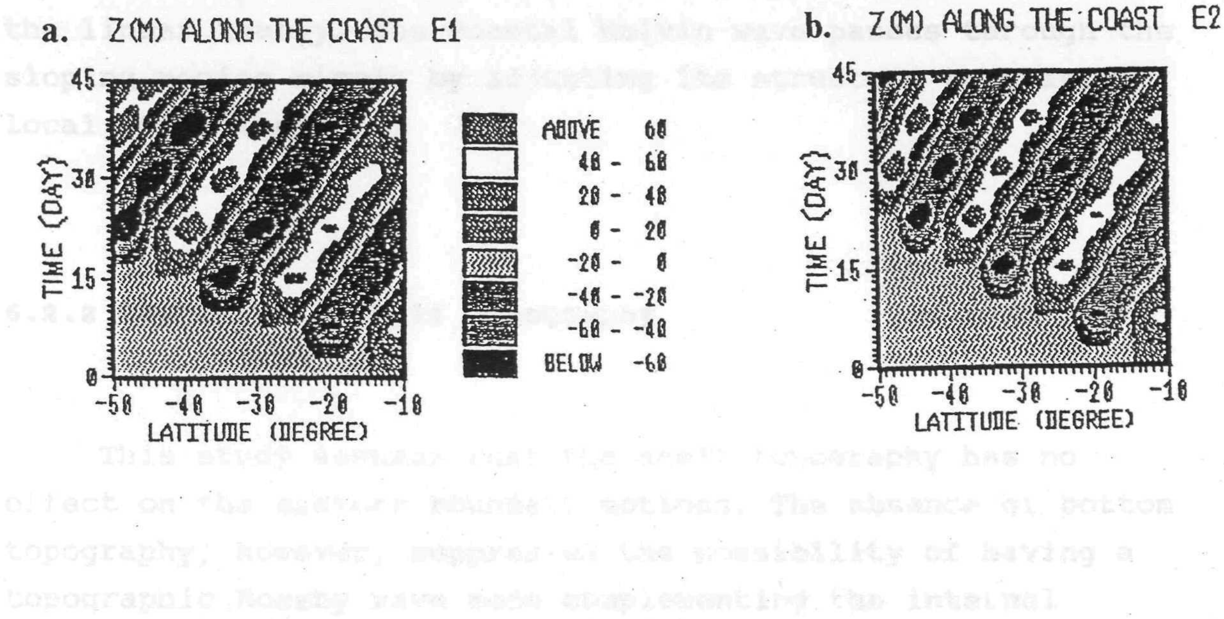

FIGURE 6.2: Time-latitude plots of the thermocline anomaly near the coast.

Both, the meridional wavelength and the wave velocity (~2.7 m/s) increase when the Kelvin wave propagates into an area of increased thermocline depth (see Figure 6.2-d).

In summary, according to Figure 6.2, the shallower the thermocline the shorter the wavelength and the smaller the increase in poleward wave amplitude. Thus, in agreement with the linear theory, the coastal Kelvin wave passes through the sloping region simply by adjusting its structure to suit local conditions.

6.2.2 Continental shelf topography

This study assumes that the shelf topography has no effect on the eastern boundary motions. The absence of bottom topography, however, suppresses the possibility of having a topographic Rossby wave mode complementing the internal Kelvin waves along the eastern boundary. Suginohara (1981) has found that the continental shelf slope has no significant effect on the transmission of energy from an incident equatorial Kelvin wave to coastally trapped baroclinic disturbances. However, at higher latitudes, the baroclinic Kelvin waves can transform to barotropic shelf waves (Suginohara, 1981; Allen and Romea; 1980). Hence, the importance of the shelf slope should be emphasized for understanding the dynamics of the eastern boundary, and the reflection problem (including the effects of continental shelf slope) needs to be studied.

6.2.3 Higher baroclinic modes

Observational studies from the Pacific Ocean (Lukas at al, 1984; Harrison and Craig, 1993, Picaut, 1993) and from the Atlantic Ocean (McCreary, 1984; McCreary et al., 1984; Verstraete, 1992) have indicated the presence of higher modes than the first baroclinic in these oceans. Hence, a higher vertical resolution model would simulate more realistically the Pacific and Atlantic oceans.

The exclusion in the present model of both continental shelf topography (barotropic mode) and higher vertical modes (others than the first baroclinic mode), was based more upon computational cost than upon physical reasons.

The presence of the barotropic mode, because of its high speed, would impose a drastic limitation on the time step of numerical integration. The CFL condition requires that $c\Delta t/\Delta s < 1$, where c is the maximum phase speed present in the system.

The inclusion of higher baroclinic modes in the model has been frustrated by the lack of computer facilities. A $n+\frac{1}{2}$ layer model was successfully developed during the course of this study but its use was constrained by the shortage of the virtual memory of the IBM 3090 available for this research.

Despite the model limitations, it is considered that its numerical results will be useful for interpreting the response of more sophisticated models as well as an aid in understanding observations. The behaviour of the low frequency motion propagation from lower to higher latitudes, along the eastern ocean boundaries, however, will only be completely understood through an interplay between modelling and observation. Models must be constrained by comprehensive data sets, making coincident equatorial and coastal data sets imperative for the studied problem. Of the utmost importance are measurements of: (i) the strength of the equatorial wave emitted from the western boundary; (ii) coastal Kelvin waves at several latitudes; and (iii) westward-propagating Rossby waves at different longitudes.

APPENDIX

THE NUMERICAL MODEL

A number of numerical experiments have been carried out to test the ability of this ocean model in simulating some important characteristics of low frequency wave dynamics.

A test simulated the spin-up in a closed ocean basin, focusing on the internal Kelvin and Rossby waves generated by numerical solutions. Another test involved total energy conservation (preserved in the model, at least, within 0.02%) and kinetic energy balance in the system (the residual error representing less than 0.001%). An experiment investigating the behaviour of a Kelvin wave interacting with a mean flow - a problem essentially non linear (Anderson and Rowlands, 1976) - was also performed. This experiment showed the competence of the present model to reproduce a phenomenon, in a context where the non linear terms are important. The tests, not shown here, can be found in Soares (1992).

Section A.1 presents the numerical form of the equations described in Chapter 3. Sections A.2 and A.3 examine in greater depth the time discretization schemes used in the numerical model.

Section A.4 addresses the problem of the conservation of properties of the numerical scheme used in the study. The stability criteria applied to the model are defined in Section A.5. The effect of inclusion of lateral viscosity in the numerical model is discussed in Section A.6.

A.1 Dynamic equations: discrete form

In order to translate Equations (3.2.1)-(3.2.3) and (3.2.8)-(3.2.10) into finite-difference form a Richardson Lattice (also known as Arakawa "C" grid; Figure A1) was chosen. The choice of the C grid is based on the fact that it best simulates the geostrophic adjustment mechanism (Mesinger and Arakawa, 1976). The zonal and meridional velocities (u and v) are defined on the boundary of each grid cell whilst the interface displacement (h) is defined at the centre of each grid cell.

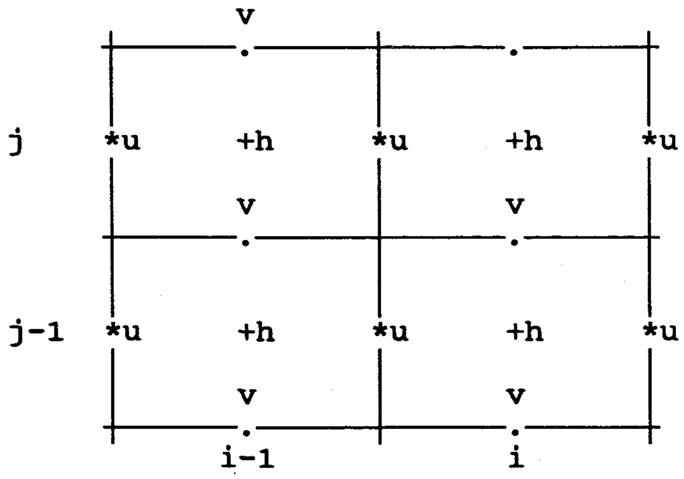

FIGURE A1 - Location of variables *h*, *u*, and *v* on a Richardson Lattice.

The discretization scheme used in this model is a modification of the traditional forward-backward (FB) scheme (Castro, 1985): the gravity wave terms, which are the layer interface displacement gradient in the momentum equations and divergent term in the continuity equation, of Equations (3.2.1)-(3.2.3) and of Equations (3.2.8)-(3.2.10) were discretized using a FB scheme (see Section A.2). The advection and Coriolis terms of the momentum equations were centred in time using the Adams-Bashforth scheme (see Section A.3).

The viscous term was lagged in time, as usual, in order to keep the system stable. A constant value for the horizontal eddy viscosity, $A_H=10^3$ m^2/s, was used in order to damp grid scale waves. A coefficient of viscosity of O(10^3 m^2/s) is similar to that used in most other models of a similar type (see Section A.6).

A.1.1 Non linear equations

The discretized form of Equations (3.2.1)-(3.2.3), used in this work is:

$$\begin{aligned} u(t+\Delta t) = u(t) - \Delta t\{&[1.5B_i(t) - 0.5B_i(t-\Delta t)] \\ &+ \delta_i P(t+\Delta t) - A_H\delta^2 u(t)\} \end{aligned} \qquad \text{(A.1.1)}$$

$$\begin{aligned} v(t+\Delta t) = v(t) - \Delta t\{&[1.5B_j(t) - 0.5B_j(t-\Delta t)] \\ &+ \delta_j P(t+\Delta t) - A_H\,\delta^2 v(t)\} \end{aligned} \qquad \text{(A.1.2)}$$

$$h(t+\Delta t) = h(t) - \Delta t\left[\delta_i U(t) + \frac{1}{\cos\theta_j}\,\delta_j[V(t)\cos\theta_j]\right] \qquad \text{(A.1.3)}$$

where B is the combination of advective and Coriolis terms, given by:

$$B_i(t) = \frac{\delta_i}{2}\left[\overline{u^2(t)}^{i} + \overline{v^2(t)}^{j}\right] - \overline{V(t)}^{ij}\,\overline{Q(t)}^{j} \qquad \text{(A.1.4)}$$

$$B_j(t) = \frac{\delta_j}{2}\left[\overline{u^2(t)}^{i} + \overline{v^2(t)}^{j}\right] + \overline{U(t)}^{ij}\,\overline{Q(t)}^{i} \qquad \text{(A.1.5)}$$

Q, the discretized potential vorticity, given by:

$$Q(t) = \left\{ \delta_i v(t) - \frac{1}{\cos\theta_j}\delta_j\left[u(t)\,\cos\theta_j\right] + f \right\} / \overline{H}^{ij} \qquad \text{(A.1.6)}$$

U and V are the components of the flux vector, given by:

$$U(t) = u(t)\,\overline{H(t)}^{i}$$

$$V(t) = v(t)\,\overline{H(t)}^{j}$$

and

$$\Delta x = r\cos\theta\,\Delta\lambda$$

$$\Delta y = r\,\Delta\theta$$

The averaging, differentiating and Laplacian operators are respectively given by (Lilly, 1965):

Averaging operators:

$$\overline{a^{i}} = \frac{1}{2}\,[a(i+1/2) + a(i-1/2)]$$

$$\overline{a^{j}} = \frac{1}{2}\,[a(j+1/2) + a(j-1/2)]$$

Differentiating operators:

$$\delta_i a = \frac{1}{\Delta x}\,[a(i+1/2) - a(i-1/2)]$$

$$\delta_j a = \frac{1}{\Delta y}\,[a(j+1/2) - a(j-1/2)]$$

Laplacian operator:

$$\delta^2 a = \frac{1}{(\Delta x)^2}\,[a(i+1) + a(i-1) - 2\,a(i)]$$

$$+ \frac{1}{(\Delta y)^2}\left\{[a(j+1) - a(j)] + \frac{\cos\theta_{j-1}}{\cos\theta_j}\,[a(j-1) - a(j)]\right\}$$

The system of Equations (A.1.1)-(A.1.3) is in fact implicit, but, if integrated in the order (A.1.3)-(A.1.1)-(A.1.2), or (A.1.3)-(A.1.2)-(A.1.1) it is explicit. To minimize the asymmetry of the system the equations are integrated in the order (A.1.3)-(A.1.1)-(A.1.2) in the odd time steps, and in the order (A.1.3)-(A.1.2)-(A.1.1) in the even time steps.

A.1.2 Linear equations

The discretized form of the linear Equations (3.2.8)-(3.2.10) can also be given by Equations (A.1.1)-(A.1.3) but with B, Q, U and V, given by:

$$B_i(t) = -\overline{V(t)^{ij}}\,\overline{Q(t)^{j}} \tag{A.1.7}$$

$$B_j(t) = \overline{U(t)^{ij}}\,\overline{Q(t)^{i}} \tag{A.1.8}$$

$$Q(t) = \frac{f}{\overline{H_0}^{ij}}$$

$$U(t) = u(t)\,\overline{H_0}^{i}$$

$$V(t) = v(t)\,\overline{H_0}^{j}$$

A.2 Forward-backward (FB) scheme

The FB scheme is obtained by first integrating the gravity terms of either the equation of motion or of the continuity equation forward, and then those of the other equation. Mesinger and Arakawa (1976) have studied the stability and convergence of this scheme in the context of the linearized shallow-water equations. They found the scheme to be stable and neutral for time steps satisfying:

$$\Delta t < \frac{2\ \Delta S}{\sqrt{gH}} \qquad (A.2.1)$$

where, Δs is the grid size.

This stability limit for the time step is twice the Courant-Friedrichs-Lewy (CFL) condition valid for other discretization schemes, like the leapfrog for example, which makes this scheme very attractive in terms of computing efficiency. In addition, as a two level scheme, it has no computational mode in time.

Henry (1981) and Foreman (1984) showed, using linearized shallow water equations, that the application of the FB scheme for both the gravity wave terms and the Coriolis terms introduces phase velocity errors for the long waves present in the model. In order to avoid these phase velocity errors, generated by asymmetric treatment of Coriolis terms, the Coriolis terms were centred in time using the Adams-Bashforth scheme. Since it is desirable to have the advective terms also centred in time, both the advection and Coriolis terms are collected together and the Adams-Bashforth scheme was used to centre the combined terms in time.

A.3 Adams-Bashforth (AB) scheme

The scheme used here is a simplified version of the original AB scheme, which is of fourth order of accuracy.

To define the AB scheme, consider the equation :

$$\frac{dU}{dt} = f(U,t); \qquad U=U(t)$$

where, t is the time (t=nΔt) and $U^{(n)}$ is the approximate value of U at time nΔt.

As a two level scheme, the AB scheme relates values of the dependent variable at two time levels (n-1 and n), in order to approximate the exact formula:

$$U^{(n+1)} = U^{(n)} + \int_{(n)\Delta t}^{(n+1)\Delta t} f(U,t)\ dt \qquad \text{(A.3.1)}$$

The scheme, second order accurate, is obtained when f in Equation (A.3.1) is approximated by a value obtained at the centre of the interval Δt by a linear extrapolation using values $f^{(n-1)}$ and $f^{(n)}$ (Mesinger and Arakawa, 1976):

$$U^{(n+1)} = U^{(n)} + \Delta t\left(\frac{3}{2}f^{(n)} - \frac{1}{2}f^{(n-1)}\right) \qquad \text{(A.3.2)}$$

A.4 Energy and vorticity

When discretizing the advective terms in the non linear momentum equations the discretization scheme best suited for the model usage has to be carefuly chosen. Different properties of the flow may or may not be conserved depending on slight changes in the discrete form of the advective terms (Castro, 1985).

In this study, due to the importance of Kelvin and Rossby waves for the dynamics of the processes studied, a scheme able to conserve both potential vorticity and potential enstrophy (average of the square of the potential vorticity) was chosen.

The scheme, given by Equations (A.1.4) and (A.1.5), conserves both potential vorticity and potential enstrophy as shown by Sadourny (1975).

The scheme, however, only conserves energy if Q=0 (pure rotational motion). Nevertheless, according to Sadourny (1975), the potential enstrophy-conserving model allows very long term integrations with negligible loss of energy in the explicit scales. Further, enstrophy conservation prevents any build up of energy in the smaller scales: most of the energy remains in the larger scales, where good accuracy makes the necessity of formal energy conservation less stringent. This, together with the much higher degree of complexity of an enstrophy-energy conserving scheme (Arakawa and Lamb, 1981), justifies the adoption of Sadourny's potential enstrophy conserving formulation.

A.5 Stability criteria

The time step (Δt) used in the study satisfies the criteria of stability, CFL and momentum diffusion. However, these conditions can only be used as guide in choosing the Δt actually used in the study because of simplifying assumptions made in their derivations. The most severe criterion is the CFL condition given, in Cartesian plane, by Equation (A.2.1). Applying it to the actual difference scheme on the spherical Earth, the stability criterion can be formulated as follows:

$$\Delta t < 2\,\frac{\min(r\cos\theta\,\Delta\lambda)}{c} \qquad \text{(A.5.1)}$$

A.6 Viscous effects

The inclusion of lateral viscosity in models can significantly affect the prediction of baroclinic waves. In linear models, both the wave decay scale (the distance that waves carry information) and the wave velocity can be modified by viscous effects.

Continuous case

The subsequent discussion follows Davey et al.(1983), who investigated the free Kelvin wave solutions of the continuous linear f-plane shallow water equations, with lateral viscosity (A_H) included. Two important parameters associated with the viscosity, characterising the offshore and alongshore viscous effects, were examined.

Offshore viscous effect:

$$\epsilon = \frac{A_H}{fR^3 l} \qquad \text{(A.6.1)}$$

Alongshore viscous effect:

$$\alpha = \frac{A_H l}{fR} \qquad \text{(A.6.2)}$$

where R is the Rossby radius (c/f) and l is the alongshore wavenumber.

It was demonstrated that long waves are slowed down by offshore viscous effects (see A.6.1) and short waves by longshore viscous effects (see A.6.2). Note that the offshore viscous effects increase as wavelength increases. This seems surprising at first sight because one expects longer waves to be less affected by viscosity. The shorter waves were shown to decay faster. The longer waves decay more slowly and the longshore decay scale is largest for long waves. The wave properties, particularly the longshore wave velocity, were shown to be much less dependent on A_H when free-slip rather than no-slip conditions were used.

Variations with latitude

The parameters described above depend on the Coriolis parameter (f), which varies with latitude. From low to higher latitudes, the parameter α changes only slightly but, ϵ increases considerably. The increases in ϵ causes a large increase in decay rate and a decrease in velocity, as a wave travels poleward. Therefore, for a fixed frequency, a decrease in wavelength accompanies decreased speed.

Discrete case

The effects of viscosity on linear free baroclinic Kelvin waves in numerical shallow-water models were explored by Hsieh et al.(1983). A model resolution parameter was defined in their study as:

$$\Delta = \frac{\Delta s}{R} \tag{A.6.3}$$

with Δs being the offshore grid spacing.

They also defined two distinct parameter regime. A "good-resolution" regime, $\epsilon/\Delta^2 >> 1$ [with ϵ given by (A.6.1) and Δ by

(A.6.3)] and a "poor-resolution" regime, $\epsilon/\Delta^2<<1$. Transition from one regime to another regime occurs when $\epsilon/\Delta^2=1$.

It was shown that in a "good-resolution" regime, the wave behaviour in a numerical model is essentially identical to that in the continuous case studied by Davey et al.(1983), i.e., finite-difference effects are negligible. Within a "poor-resolution" regime, Δ (A.6.3) becomes dominant while ϵ (A.6.1) becomes unimportant.

LIST OF REFERENCES

Adamec, D. and J.J.O'Brien, 1978: The seasonal upwelling in the Gulf of Guinea due to remote forcing. *J. Phys. Oceanogr.*, 8, 1050-1060.

Anderson, D.L.T. and P.W.Rowlands, 1976: The role of inertia-gravity and planetary waves in the response of a tropical ocean to the incidence of an equatorial Kelvin wave on a meridional boundary. *J. Mar. Res.*, 34, 295-312.

Anderson, D.L.T. and A.M.Moore, 1985: Data Assimilation, 437-463. In *Proceedings of the NATO Advanced Study on Advanced Physical Oceanographic Numerical Modeling.*

Arakawa, A. and V.R.Lamb, 1981: A potential enstrophy and energy conserving scheme for the shallow water equations, *J. Phys. Oceanogr.*, 109, 18-36.

Barber,R.T. and F.P.Chavez, 1983: Biological consequences of El Nino. *Science*, 222, 1203-1210.

Bigg, G.R. and A.E.Gill, 1986: The annual cycle of sea level in the eastern tropical Pacific. *J. Phys. Oceanogr.*, 16, 1055-1061.

Bigg, G.R. and M.Inoue, 1992: Rossby waves and El Nino during 1935-46. *Q. J. R. Meteorol. Soc.*, 118, 125-152.

Boyd, J.P, 1980: Equatorial solitary waves. Part I: Rossby Solitons. *J. Phys. Oceanogr.*, 10, 1699-1717.

Bryan, K., 1969: A numerical method for the study of the world ocean. *J. Comp. Phys.*, 4, 347-376.

Busalacchi, A.J. and J.Picaut, 1983: Seasonal variability from a model of the tropical Atlantic ocean. *J. Phys. Oceanogr.*, 13, 1564-1588.

Cane, M.A., 1979: The response of an equatorial ocean to simple wind stress pattern: I. Model formulation and analytic results. *J. Mar. Res.*, 37, 233-252.

Cane, M.A., 1983: Oceanographic events during El Niño. *Science*, 222, 1189-1195.

Cane, M.A. and R.J.Patton, 1984: A numerical model for low-frequency equatorial dynamics. *J. Phys. Oceanogr.*, 14, 1853-1863.

Cane, M.A. and E.S.Sarachik, 1976: Forced baroclinic ocean motions,I, The linear equatorial unbounded case. *J. Mar. Res.*, 34, 629-666.

Cane, M.A. and E.S.Sarachik, 1979: Forced baroclinic ocean motions,III, The linear equatorial basin case. *J. Mar. Res.*, 37, 355-398.

Cane, M.A. and E.S.Sarachik, 1983: Equatorial Oceanography. *Rev. Geophys. and Space Phys.*, 21, 1137-1148.

Castro, B.M., 1985: Subtidal response to wind forcing in the South Brazil Bight during winter. *Ph.D dissertation*, Rosenstiel School of Marine and Atmospheric Science, University of Miami, USA.

Charney, J.G., 1955: The generation of oceanic currents by winds. *J. Mar. Res.*, 14, 477-498.

Chelton, D.B. and R.E.Davis, 1982: Monthly mean sea level variability along the west coast of North America. *J. Phys. Oceanogr.*, 12, 757-784.

Clarke, A.J., 1983: The reflection of equatorial waves from oceanic boundaries. *J. Phys. Oceanogr.*,13, 1193-1207.

Clarke, A.J., 1992: Low-frequency reflection from a nonmeridional eastern ocean boundary and the use of coastal sea level to monitor eastern Pacific equatorial Kelvin waves. *J. Phys. Oceanogr.*,22, 163-183.

Clarke, A.J. and C.Shi, 1991: Critical frequencies at ocean boundaries. *J. Geophys. Res.*, 96, 10731-10738.

Davey, M.K., W.W.Hsieh and R.C.Wajsowicz, 1983: The free Kelvin wave with lateral and vertical viscosity. *J. Phys. Oceanogr.*, 13, 2182-2190.

Delcroix, T., J.Picaut and G. Eldin, 1991: Equatorial Kelvin and Rossby waves evidenced in the Pacific ocean through Geosat sea level and surface current anomalies. *J. Geophys. Res.*, 96, 3249-3262.

Du Penhoat, Y., M.A.Cane and R.J.Patton, 1983: Reflections of low frequency equatorial waves on partial boundaries, 237-258. In *Hydrodynamics of the equatorial ocean*, Elsevier Oceanography series.

Enfield, D.B., 1989: El Niño, past and present. *Rev. Geophys.*, 27, 159-187.

Enfield, D.B. and J.S.Allen, 1980: On the structure and dynamics of monthly mean sea level anomalies along the Pacific coast of North and South America. *J. Phys. Oceanogr.,* 10, 557-588.

Foreman, M.G.G., 1984: A two dimensional dispersion analysis of selected methods for solving the linearized shallow water equations. *J. Comp. Phys.*, 56, 287-323.

Glantz, M.H., R.W.Katz and N.Nicholls, 1990: *Teleconnections linking worldwise climate anomalies*, Cambridge University Press.

Gill, A.E., 1982: *Atmosphere-Ocean Dynamics*, Academic, San Diego, Calif.

Grimshaw, R. and J.S.Allen, 1988: Low-frequency baroclinic waves off coastal boundaries. *J. Phys. Oceanogr.*, 18, 1124-1143.

Hsieh, W.W., M.K.Davey and R.C.Wajsowicz, 1983: The free Kelvin wave in finite-difference numerical models, *J. Phys. Oceanogr.*, 13, 1383-1397.

Henry, R.F., 1981: Richardson-Sielecki schemes for shallow-water equations, with applications to Kelvin waves. *J. Comp. Phys.*, 41, 389-406.

Houghton, R.W., 1976: Circulations and hydrographic structure of the Ghana continental shelf during the 1974 upwelling. *J. Phys. Oceanogr.*, 6, 909-924.

Hurlburt, H.J., J.Kindle and J.J.O'Brien, 1976: A numerical simulation of the onset of El Niño. *J. Phys. Oceanogr.*, 6, 621-631.

Johnson, M.I. and J.J.O'Brien, 1990: The northeast Pacific Ocean response to the 1982-1983 El Niño. *J. Geophys. Res.*, 95, 7155-7166.

Katz, E.J., 1987: Equatorial Kelvin waves in the Atlantic. *J. Geophys. Res.*, 92, 1894-1898.

Knox, R.A and Halpern, 1982: Long range Kelvin wave propagation of transport variations in Pacific ocean equatorial currents. *J. Mar. Res.*, 40, Suppl, 329-339.

Kubota, M. and J.J.O'Brien, 1988: Variability of the upper tropical Pacific Ocean model. *J. Geophys. Res.*, 95, 13930-13940.

LeBlond, P.H. and L.A.Mysak, 1978: *Waves in the ocean*, Elsevier Oceanographic Series, 20, Amsterdam, The Netherlands.

Lilly, D.K., 1965: On the computational stability of numerical solutions of time-dependent non-linear geophysical fluid dynamics problems. *Mon. Wea. Rev.*, 93, 11-26.

Longuet-Higgins, M., 1964: Planetary waves on a rotating sphere. *Proc. Roy. Soc., Ser. A*, 279, 446-473.

Madden, R.A. and P.R. Julian, 1971: Detection of a 40-50 day oscillation in the zonal wind in the tropical Pacific. *J. Atmos. Sci.*, 28, 702-708.

Madden, R.A. and P.R. Julian, 1972: Description of global scale circulation cells in the tropics with a 40-50 day period. *J. Atmos. Sci.*, 29, 1109-1123.

McCreary, J.P., 1976: Eastern tropical ocean response to changing wind systems. *J. Phys. Oceanogr.*,6, 632-645.

McCreary, J.P., 1977: A model of tropical ocean-atmosphere interaction. *Mon. Wea. Rev.*, 111, 370-389.

McCreary, J.P, 1984: Equatorial beams. *J. Mar. Res.*, 42, 395-430.

McCreary, J.P, J.Picaut and D.W.Moore, 1984: Effects of remote annual forcing in the eastern tropical Atlantic ocean. *J. Mar. Res.*, 42, 45-81.

McCreary, J.P. and Anderson, D.L.T., 1991: An overview of coupled ocean-atmosphere models of El Nino and the Southern Oscillation. *J. Geophys. Res.*, 96, 3125-3150.

McPhaden, M.J. and B.Taft, 1988: Dynamics of seasonal and intraseasonal variability in the eastern equatorial Pacific. *J. Phys. Oceanogr.*, 18, 1713-1732.

Mesinger, F. and A.Arakawa, 1976: Numerical methods used in atmospheric models, volume 1. *GARP Publication Series*, 17, World Meteorological Organization.

Meyers, G., 1979: Annual variation of the slope of the 14°C isotherm along the equator in the Pacific ocean. *J. Phys. Oceanogr.*, 9, 885-891.

Miller, M.J. and A.J.Thorpe, 1981: Radiation conditions for the lateral boundaries of limited-area numerical models. *Quart. J. R. Met. Soc.*, 107, 615-628.

Miller, L., R.Cheney and B.Douglas, 1988: GEOSAT altimeter observations of Kelvin waves and the 1986-87 El Niño. *Science*, 239, 52-54.

Moore, D., 1968: Planetary-gravity waves in an equatorial ocean. *Ph.D. Dissertation*, Harvard University, Cambridge, Massachusetts.

Moore, D. and S.G.H.Philander, 1977: Modelling of the tropical ocean circulation. *In "The Sea"*, vol.6, 319-361, Wiley, New York.

Moore, D., P.Hisard, J.McCreary, J.Merle, J.O'Brien, J.Picaut, J-M Verstraete and C.Wunsch, 1978: Equatorial adjustment in the eastern Atlantic. *Geophys. Res. Lett.*, 5, 637-640.

Pares-Sierra, A. and J.J.O'Brien, 1989: The seasonal and interannual variability of the California current system: A numerical model. *J. Geophys. Res.*, 94, 3159-3180.

Philander, S.G.H., 1978: Forced oceanic waves. *Rev. Geophys. Space Phys.*, 16, 15-46.

Philander, S.G.H., 1979: Equatorial waves in the presence of the Equatorial Undercurrent. *J. Phys. Oceanogr.*, 9, 254-262.

Philander, S.G.H., 1990: *El Niño, La Nina and the southern oscillation*, Academic Press Inc.

Picaut, J., 1983: Propagation of the upwelling in the eastern equatorial Atlantic. *J. Phys. Oceanogr.*, 13, 18-37.

Picaut, J., 1993: Influence of density stratification and bottom depth on vertical mode structure functions in the tropical Pacific. *J. Geophys. Res.*, 98, 14727-14737.

Quinn, W.H., V.T.Neal and S.A. de Mayolo, 1987: El Niño occurrences over the past four and a half centuries. *J. Geophys. Res.*, 92, 14449-14461.

Rasmusson, E.,M. and T.C.Carpenter, 1982: Variations in tropical sea surface temperature and surface wind fields associated with the Southern Oscillation/El Nino. *Mon. Wea. Rev.*, 110, 354-384.

Rasmusson, E.M. and J.M.Wallace, 1983: Meteorological aspects of the El Niño/Southern Oscillation. *Science*, 222, 1195-1202.

Ripa, P. and S.Hayes, 1981: Evidence for equatorially trapped waves at the Galapagos Islands. *J. Geophys. Res.*, 86, 6509-6516.

Sadourny, R., 1975: The dynamics of finite-difference models of the shallow-water equations. *J. Atmos. Sci.*, 32, 680-689.

SCOR, 1983: Scientific Committee on Oceanic Research, Working Group 55, Prediction of "El-Niño", in *SCOR Proceedings*, vol.19, pp47-51, Paris, 1983.

Schopf, P.S., D.L.T.Anderson and R.Smith, 1981: Beta-dispersion of low frequency Rossby waves. *Dyn. Atmos. Ocean*, 5, 187-214.

Servain, J., J.Picaut, and J.Merle, 1982: Evidence of remote forcing in the equatorial Atlantic ocean. *J. Phys. Oceanogr.*, 12, 457-463.

Soares, J.R., 1991: Extra tropical response of the ocean to El Niño-Southern oscillation events. *M.Phil/Ph.D. Upgrading Report*, Oceanography Department, University of Southampton.

Spillane, M.C., D.B.Enfield and J.S. Allen, 1986: Intraseasonal oscillations in sea level along the west coast of the Americas. *J. Phys. Oceanogr.*, 17, 313-325.

Veronis, G. and H.Stommel, 1956: The action of variable wind-stresses on a stratified ocean. *J. Mar. Res.*, 15, 43-69.

Verstraete, J.M, 1992: The seasonal upwellings in the Gulf of Guinea. *Progress in Oceanography*. 29, 1-60.

Weickmann, K.M., 1991: El Nino/Southern Oscillation and Madden-Julian (30-60 days) oscillations during 1981-1982. *J. Geophys. Res.*, 96, 3187-3195.

Weisberg, R.H., A.Horigan and C.Colin, 1979: Equatorially trapped Rossby-gravity wave propagation in the Gulf of Guinea. *J. Mar. Res.*, 37, 67-86.

White, W.B. and J.F.T.Saur, 1983: A source of interannual baroclinic waves in the eastern tropical Pacific. *J. Phys. Oceanogr.*, 13, 531-544.

Wyrtki, K., 1975: El Niño-The dynamic response of the equatorial Pacific Ocean to atmospheric forcing. *J. Phys. Oceanogr.*, 5, 572-584.